NEW TECHNOLOGIES FOR LIVE CELL FLUORESCENCE IMAGING OF POST-TRANSLATIONAL MODIFICATIONS

by
Brian L. Ross

A dissertation submitted to Johns Hopkins University in conformity with the requirements
for the degree of Doctor of Philosophy

Baltimore, MD
October 2018

Abstract

Post translational modifications (PTMs) of proteins serve critical roles in both signal transduction as well as gene regulation. Phosphorylation is an important means by which signals are transmitted, processed, and amplified within a cell, while methylation is a critical regulator of chromatin organization mediated by histone proteins. The spatial distribution and temporal dynamics of these PTMs must be tightly controlled to allow for proper functioning. In signaling pathways, distinct spatiotemporal patterning of signaling activities is a critical means by which cells use the same molecular components to regulate diverse functionalities. In gene regulation, precise spatial organization of histone methylation allows for the proper distributions of heterochromatin and euchromatin, controlling which parts of the genome are transcriptionally active or repressed.

In this dissertation, we discuss three new genetically encodable fluorescence technologies to expand the information we can obtain about the spatiotemporal dynamics of PTMs in real time in live cells. First, we discuss a new suite of genetically encodable fluorescent biosensors that are both single-color and ratiometric. These FLuorescent Anisotropy Reporters (FLARE) are based on homo-FRET, and they allow for multiparameter imaging of cell signaling activities, such as kinase activity and second-messengers. We then present a panel of biosensors called Fluorescent fLuctuation INcrease by Contact (FLINC) sensors that allow for the creation of sub-diffraction limit resolution maps of kinase activity. They were then used to map highly localized signaling microdomains of the Protein Kinase A (PKA) pathway in the plasma membrane. Finally, we describe a new fluorescent probe for superresolution mapping of tri-methylated histone 3 lysine 9 (H3K9me3), a critical histone modification for regulating the formation of heterochromatin in the nucleus. By engineering a mutant of the chromobox homolog protein 1 (CBX1) with high affinity for H3K9me3 and fusing it with a photoactivatable fluorescent protein, we demonstrate the ability to create sub-diffraction limit resolution maps of H3K9me3 in live cells.

Acknowledgements

When I started the PhD program back in 2011, I could not have predicted where it would have taken me, personally and scientifically. I have grown as a scientist, and engineer, and a researcher. Throughout these years, I have had the support and mentorship of many individuals on both coasts of the United States.

I would first and foremost like to thank my advisor Dr. Jin Zhang, who has taught me immensely about the scientific endeavor. She has been a supportive mentor throughout the process of performing the research included in this dissertation through her guidance and leadership. She has also taught me a lot about how to approach data objectively, how to manage collaborations, and how to develop and manage a project.

I would also like to thank the members of the Zhang laboratory, who have been a pleasure to work with. Specifically, I would like to thank Dr. Gary Mo, who served as my mentor during my rotation in the Zhang laboratory and leads the FLINC project. Because of his creativity, he has always been a key person in the lab with whom I consult on scientific matters in the lab. He has also been the source of many lively discussions. I would also like to thank Brian Tenner, who has sat next to me in the laboratory since we moved to UCSD. He helped me immensely with projects at critical times, and he has been a source of support throughout the time here. He has also been the source of excellent scientific discussions and a great person with whom to brainstorm design ideas. I would like to thank Dr. Sohum Mehta for his leadership within the laboratory, his astute scientific insights, and his help with manuscript editing and illustration drawing. I would like to thank Dr. Eric Greenwald, whose microscopy knowledge was instrumental in setting up the anisotropy imaging microscopy setup in the San Diego laboratory. Many

other members of the lab, too many to name individually, have also contributed to my positive experience in the laboratory. They have gone on lab trips with me, eaten lunch together with me, engaged in scientific discussions with me, and helped me both inside and outside the laboratory. I would like to thank all of them.

There were many faculty members and colleagues, both at Johns Hopkins and UCSD with whom I have interacted throughout my graduate school process and who have contributed to my scientific knowledge and skills. Dr. Andre Levenchko and Dr. Inoue were great mentors during my rotations in their laboratory. Furthermore, my thesis committee, Dr. Jie Xiao and Dr. Scot Kuo has generously expended considerable effort on my behalf guiding me throughout the process and also serving as research collaborators. Dr. Mark Rizzo served as a mentor on the FLARE project and a member of my thesis committee. He generously allowed me to use his microscope for the FLARE project, and he gave me great advice and insights and was a pleasure to work with. The members of his laboratory, Michele Markwardt, Nicole Snell, Kendra Seckinger, and Jennifer McFarland were also of great help to me throughout my time in Baltimore and wonderful to work aside when I was at the Rizzo lab. Dr. Wei Wong and Ryan Hard, furthermore, were excellent collaborators in the histone modifications imaging project and a pleasure to work with.

I would like to thank the staff in the Johns Hopkins Biomedical Engineering and the Pharmacology departments for their support in making my graduate school educational experience a positive one. I would also like to thank the University of California, San Diego Pharmacology Department for welcoming me a as a visiting researcher.

I would like to thank my funding sources, including the National Institute of Health for making the research possible and providing the funds to support me in this research throughout the years.

To my many friends and family, in Maryland, California, and elsewhere, for helping me make these last several years an incredible time.

To my parents, you provided me with endless love, warmth, optimism and advice throughout the years, and you provided me with the foundation to allow me to accomplish this PhD. You engrained in me a love for education. You have celebrated my accomplishments and helped me troubleshoot when I had difficulties. You listened to me explain my research while I scribbling on post-it notes. Most importantly, you have supported me in this long journey.

Table of Contents

List of Figures

List of Tables

Chapter 1 Post-Translational Modifications in Signal Transduction and Epigenetic Regulation

Introduction

A wide array of chemical modifications to proteins dramatically alter their function. These post-translational modifications (PTMs) are critical for many cellular functions, such as processing information, maintaining the proper levels of protein, regulating the cell cycle, and controlling gene expression. The chemical modification may direct the protein to the proper localization, act as a switch to regulate the activity of the enzyme, affect interactions with other cellular structures, control the degradation of the protein, or a wide variety of other functions.

The controlled addition or removal of PTMs allows the cellular machinery of a cell to respond rapidly to changing conditions, both internally and externally. An enzyme can act as a sensor to detect a signal, which it relays by modifying effectors with PTMs. These effectors in turn either further transmit the signal to other effectors or mediate other cellular processes. The enzymes that conditionally facilitate the addition or removal of PTMs control the spatial patterning within the cell and temporal dynamics of the modification. By tightly regulating PTMs in space and in time, these enzymes help ensure, for example, that the proteins they modify are activated, expressed, degraded, and/or localized at the right place and time in an often rapidly changing cellular environment.

This tight spatiotemporal regulation of PTMs motivates the development of novel tools for monitoring post-translational modifications. Presented here are three novel technologies that that push the limits of our abilities to study the spatiotemporal features of phosphorylation and methylation, two critical PTMs for signal processing and gene expression regulation, respectively. Phosphorylation cascades form the backbone of signal transduction pathways, allowing the cell to sense extra-cellular signals, transmit and process that information, and elicit the appropriate cellular response. Methylation, on the other hand is a critical regulator of histone proteins, which package DNA and regulate gene expression. In this dissertation, we present a suite of genetically-encodable molecular tools compatible with live-cell fluorescence imaging that expand the amount of information we can gather about these critical PTMs in terms of their spatial distribution within the cell and their temporal dynamics.

Spatiotemporal Regulation of Kinase Activity in Signal Transduction

Cells detect, process, and respond to changes in its external and internal environment through networks of interconnected and coordinated signaling pathways. Receptors sense signals, including chemical, optical, or mechanical inputs, and then transmit these signals to a wide variety of effectors, which further process, amplify, relay, and interpret the signals. These pathways allow the cell to elicit the appropriate cellular responses to a changing environment or cellular state. Signaling activities in a cell include addition or removal of PTMs (principally phosphorylation), induction of protein-protein interactions, and the recruitment of second-messengers. Protein kinases, which add phosphate groups to other proteins, form the backbone of these signaling transduction pathways. There are approximately 500 protein kinases and approximately 100,000 phosphorylation sites in the human genome[1,2].

The correspondence between cellular input and output in signal transduction pathways are far from one-to-one. The same signal may trigger many different cascades, pathways often cross-talk with one another, and one effector may control many cellular processes. The number of genes involved in signal transduction, moreover, is surprisingly low compared to the number of cellular processes that they regulate, which implies that signaling pathways must share components[3]. Noise further limits the amount of information processed by individual signaling pathways[4]. These observations suggest that cell fate decisions are not encoded simply at the gene or protein level.

For a kinase signaling cascade to allow cells to make many cellular decisions, such as whether to migrate, proliferate, undergo cytoskeletal rearrangement, or initiate apoptosis, key components of the pathway are regulated both in terms of their temporal dynamics and spatial distribution across the cell. Different spatiotemporal profiles in activation of protein kinases result in different gene activation profiles and thus activate different cellular processes. Spatial regulation of kinase activity may occur, for example, through targeting of the enzyme to particular subcellular compartments, the localized degradation of signaling molecules, complex patterning on a membrane, and/or by coordination with anchoring proteins. Temporal dynamics of kinase activity, on the other hand can be mediated by the presence of phosphatases, for example, or can be the result of particular signaling motifs in the pathway architecture, such as feedback loops. Signaling activities may be highly transient, sustained over longer periods of time, or exhibit more complex temporal patterns, such as oscillations.

Spatiotemporal regulation of cAMP/PKA signaling Pathway

The cyclic adenosine monophosphate (cAMP)/cAMP-dependent protein kinase (PKA) pathway, a highly versatile and intensively studied signaling pathway expressed in nearly all mammalian tissues, undergoes many levels of compartmentalization and temporal control[5,6]. The pathway is initiated by a ligand, such as a hormone or neurotransmitter, binding to a G-coupled protein receptor (GPCR), which in turn activates a heterotrimeric G protein, composed of a stimulatory Gα ($G_s\alpha$) subunit and a Gβγ subunit. $G_s\alpha$ is activated when the GPCR acts as a guanine nucleotide exchange factor (GEF), causing the $G_s\alpha$ to unbind guanine diphosphate (GDP) and bind guanine triphosphate (GTP). This change causes $G_s\alpha$ to unbind from the Gβγ heterodimer and associate with the transmembrane adenylyl cyclase (tmAC), which begins to convert molecules of free ATP into cAMP. cAMP acts a second messenger, which activates a number of effectors, including the cAMP-dependent protein kinase (PKA), a heterotetrameric holoenzyme composed of two catalytic domains (C) and two regulatory (R) domains. cAMP binding to the C domain causes the R domains to move out of the way of the active site, resulting in the phosphorylation of downstream effectors, including transcription factors, metabolic enzymes, and ion channels regulators. The precise functional output of this pathway in a particular context is controlled largely by the spatial and temporal organization of the pathway. This regulation is caused by spatial restriction of cAMP into different pools as well as the binding of PKAs and other critical components of the pathway to anchoring proteins called A-kinase anchoring proteins (AKAPs).

One of the principal ways that the cAMP/PKA pathway is spatiotemporally regulated is through localized pools of cAMP, and subsequently localized PKA activity[7]. These localized signals are mediated by organization of components of the pathway among membrane subdomains, the localized degradation of cAMP, as well as anchoring of pathway components onto anchoring proteins. The spatial distribution of GPCRs, G-proteins and tmACs between different subdomains of the plasma membrane, such as lipid rafts and non-rafts regions, contributes to the spatiotemporal features of the cAMP responses. Disruption of lipid rafts, for instance, increases the amplitude and duration of cAMP responses upon signaling through β2-adrenergic receptor (β2AR), which associates with membrane rafts, but not for prostaglandin E (PGE) receptor, which is excluded from membrane rafts[8]. Likewise, in β2AR-mediated signaling the disruption of raft domains is associated with enhanced PKA activation, while the presence of rafts is associated with basal PKA activity in the vicinity of the rafts[9]. Different isoforms of tmACs also have different distributions among membrane subdomains, which establish different spatiotemporal features of cAMP[10–13].

In addition to segregation of components of the cAMP/PKA pathway into different membrane subdomains, spatial regulation of cAMP is also mediated by localized activity of phosphodiesterases (PDEs), which hydrolyze cAMP. In particular PDEs are involved in establishing cAMP gradients between cellular compartments, either acting as a diffusion barrier or as a cAMP sink[7]. One example of this type of regulation is found in cardiac myocytes, where stimulation of the β1-adrenergic receptor (β1AR) results in PKA phosphorylating phospholamban (PLB) at the sarcoplasmic reticulum (SR) and subsequently increased calcium reuptake to the SR[14]. However, stimulation of PGE2 does not result in PKA activity at the SR. It has been shown that PGE2 stimulation leads to activation of PDE4D, which blocks diffusion of cAMP from the membrane to the SR and thus prevents activation of PKA in the vicinity of the SR. Furthermore, inhibition of PDE4 can partially remove this cAMP gradient, allowing for PKA activity at the SR upon PGE2 stimulation.

A-kinase anchoring proteins (AKAPs) are also key regulators of the spatial and temporal features of the PKA pathway. AKAPs, targeted to particular subcellular locations, coordinate the positions of GPCRs, G-proteins, the PKA holoenzyme, PDEs, phosphatases, and PKA effectors to create highly localized and functionally distinct signaling complexes, called signalosomes. These complexes amplify and accelerate particular signaling events within the signalosome while preventing other effects outside of the signalosome. For example, AKAP79 binds PKA, βARs, several isoforms of tmAC, calcium dependent protein kinase (PKC), calcineurin, the voltage-gated L-type calcium channels, and M-type potassium channels[15–17]. Poly-basic regions on the AKAP79, further, localizes the AKAP to the plasma membrane through binding to phospholipids[18], and palmitoylation also targets it to lipid rafts[19]. This signalosome serves as a point of convergence between cAMP-mediated and calcium-mediated signaling, allowing for a coordinated regulation of the ion channels with which it associates.

Spatiotemporal regulation of the MAPK/Erk cascade

Like the cAMP/PKA pathway, the mitogen activated protein kinase (MAPK)/Erk cascade undergoes tight spatiotemporal regulation that determines the ultimate cellular response. The MAPK/Erk pathway is initiated by the binding of a ligand to a receptor tyrosin kinase (RTK), which upon ligand binding undergoes dimerization and autophosphorylation on tyrosine residues. Binding of growth factor receptor bound protein 2 (Grb2) to the phosphotyrosine on the RTK then recruits and activates a GEF, called son of sevenless (SOS), which mediates the exchange of a GDP for a GTP on the small GTPase Ras and activates it. Ras then recruits the serine-threonine kinase Raf to the membrane, priming it for activation. Raf then phosphorylates Mek, a protein kinase with dual serine/threonine and tyrosine specificities. Mek then phosphorylates dual threonine-tyrosine sites on Erk, a MAPK that then phosphorylates a large number of downstream effectors, such as the kinase Rsk as well as a number of transcription factors in the nucleus.

The kinetics of Erk activation and inactivation has been shown to determine the phenotypic response. For example in the pheochromocytoma cell line PC-12, transient activation of Erk activity from epidermal growth factor (EGF) stimulation results in cell proliferation[20–23]. On the other hand, sustained Erk activity from nerve growth factor receptor (NGF) causes leads to neurite outgrowth, a sign of cellular differentiation. Many mechanisms may account for the difference in Erk activity dynamics when the pathway is activated by the two different ligands. These include differential kinetics in receptor degradation or recycling upon stimulation with EGF or NGF. Furthermore, it has been suggested that a positive feedback loop between Erk and Raf functions in the case of NGF signaling to sustain Erk activity, while a negative feedback loop in the case of EGF signaling may account for the transience[23]. Cross-talk between the PKC and PKA pathways has also been implicated in determining the cellular response to activation of the MAPK/Erk pathway. Raf Kinase Inhibitor Protein (RKIP), for example, blocks the interaction between Raf and Mek and serves as a negative regulator of the MAPK/Erk pathway[24]. Phosphorylation of RKIP by PKC in the case of NGF, but not EGF signaling, releases RKIP from Raf, allowing activation of Mek and possibly a direct positive feedback loop between Erk and Raf[25]. Likewise, crosstalk with the PKA pathway for both NGF and EGF signaling has also been shown, potentially implicating cAMP/PKA signaling as another control on Erk activity dynamics. Both NGF and EGF lead to PKA activity in the vicinity of the plasma membrane, but not in the cytosol, with this gradient of activity mediated by PDE3[26]. Furthermore, this PKA activity is transient in the case of EGF stimulation but sustained in the case of NGF stimulation.

In addition to temporal regulation of Erk activity resulting in functional specificity of the pathway, spatial organization of Erk activity is also critical for determining the functional output. Compartmentalization as well as scaffolding both plays important roles in determining the phenotypic output of MAPK/Erk pathway stimulation. With regards to compartmentalization, translocation of Erk to the nucleus and subsequent activation of its transcription factor effectors has been shown to be essential for proliferation in PC-12 cells and other cell types[22,27]. However, retention of Erk in the cytosol inhibits survival and proliferation signals as well as activating some pro-apoptotic proteins[28]. Furthermore, like in the case of AKAPs in cAMP/PKA signaling, scaffolds also integrate, coordinate, and direct the signaling of the MAPK/Erk pathway at key locations within the cell[3,29]. Scaffolds for components of the MAPK/Erk pathway fine tune the dynamics of the cascade, localize the signal to particular sub-cellular regions, and act as allosteric regulators. For example, the scaffold Kinase Suppresor of Ras (KSR) binds to MEK in the cytosol in quiescent cells. However, upon activation of Ras, it translocates to the nucleus and binds Raf and Erk. By bringing together the key components of the kinase cascade into a single multi-protein complex, KSR fine-tunes the dynamics of signaling[30]. KSR also acts as an allosteric regulator of B-RAF and aids in its dimerization and subsequent activation[31].

The cAMP/PKA and the MAPK/Erk pathways share similar strategies for achieving spatiotemporal regulation, including compartmentalization, scaffolding, cross-talk, organization among plasmallemal subdomains, and feedback. These strategies allow the same protein components control a large number of cellular processes in a specific and context-dependent way.

Methods for Studying Spatiotemporal Regulation of Signaling Pathways

Traditionally, the dynamics of kinase activities were studied through *in vitro* biochemical assays, such as Western blotting, and immunofluorescence. Because Western blotting requires lysing a large population of cells, it provides bulk information about the levels of a particular protein or PTM within a population at a particular moment in time. It also does not provide single cell information or information on the variability among different cells. Dynamic experiments require the multiple repeats in different populations of cells and preparing separate blots at each time point. Moreover, information on the sub-cellular compartmentalization of signaling can be obtained through cellular fractionation. However, through *in vitro* assays, it is difficult to study more complex spatial arrangements of signaling activities. Immunofluorescence, on the other hand, does allow for single-cell observations and detailed spatial information, but it is performed in fixed cells, which prevents observations of dynamic processes in real time.

To overcome these challenges, the development of genetically-encodable fluorescent biosensors based on fluorescent proteins (FPs) has allowed the monitoring of a variety of signaling activities in live cells in real time. Genetic encodability of these molecular tools allows the researcher to take advantage of the cellular machinery to synthesize the biosensor. Furthermore, it allows targeting to particular subcellular locations using known targeting sequences, making them well-suited for spatiotemporal studies.

These biosensors work by coupling a molecular switch regulated by a particular signaling activity with a change in fluorescence of an FP[32]. The molecular switch could be the enzyme of interest if a substantial change in conformation occurs, such as in the case of the myosin light chain kinase (MLCK) sensor[33,34]. More commonly for kinase activity sensors, however, the switch is composed of two proteins or protein domains that bind or unbind in the presence of an activity. The switch for many kinase activity reporters (KARs), such as the PKA activity reporter (AKAR)[9,35], Erk kinase activity reporter (EKAR)[36], and PKC activity reporter (CKAR)[37], are composed of a substrate peptide of the kinase of interest as well as a phosphoaminoacid binding domain, that binds the substrate after phosphorylation by the kinase of interest.

This switch must be coupled with a change in fluorescence, which may be a change in the emission ratio between two FPs in a ratiometric reporter or a change in the intensity of a single wavelength in an intensiometric reporter. Most kinase activity reporters are ratiometric biosensors based on Forster's Resonance Energy transfer, a non-radiative, distance-dependent energy transfer from a donor fluorophore to an acceptor fluorophore. This transfer requires that the emission spectrum of the donor overlaps with the excitation spectrum of the acceptor. It further requires that the donor and acceptor fluorophores to be in proximity, within a distance of approximately 10 nm or less.

Single-color reporters, on the other hand, can rely on several designs for modulating the fluorescence output. Some sensors use an FP with an impaired β-barrel, which is designed to switch conformations and thus change fluorescence upon modulation of the molecular switch[32]. While this design is more common among small molecule sensors, such as the calcium GCaMP family of sensors[38,39], a similar design in the sinphos sensors for monitoring insulin receptor kinase induced tyrosine phosphorylation[40]. Fragment complementation is another single-color method for connecting a protein-protein interaction with a change in fluorescence or bioluminescence[41]. In this technique, an FP or bioluminescent protein is divided into two non-functional fragments, which are fused to two proteins of interest. Upon binding of the two proteins, the fragments reconstitute into a working FP or bioluminescent protein. The reconstitution of FPs is irreversible, while the reconstitution of bioluminescent proteins is reversible[32]. Therefore, for reversible processes like kinase activity, luminescence is favorable for this design; a luminescent version of AKAR and CKAR based on fragment complementation, called LumAKAR,and LumCKAR, has been developed[42].

A relatively new approach, using dimerization dependent FP, can in principle be used to create sensors that are either single-color or ratiometric[43–45]. ddFPs require two FPs, one called A whose fluorophore is quenched in the monomeric state, and the other called B that is completely non-fluorescent. The heterodimerization of A and B, which can be modulated by a molecular switch of interest results in an increase in the fluorescence of A. A ratiometric variant of this design, called Fluorescent Protein Exchange[45], uses a green and red variants of A (GA and RA, respectively), that share a binding partner B. B is exchanged from GA to RA in the presence of an activity of interest, resulting in a change in the ratio of green to red fluorescence. A FPX based Erk sensors based on EKAR has been demonstrated.

While all of these biosensors have the advantage of genetic encodability and the ability to monitor processes at real time, they are also subject to limitations. First, FRET sensors, because they use two fluorescent proteins of different wavelengths, they occupy a large amount of the visible spectrum, making multiplexing difficult. However, imaging two FRET sensors simultaneously in the same cell has been demonstrated. In one approach, a long-stokes shift FP, LSS-mOrange as a donor is one biosensor, while a cyan donor is used in the other sensor, so that the same wavelength can excite donors with spectrally distinct emissions[46]. In another approach, two biosensors with the same or spectrally similar donors are paired with spectrally distinct acceptors are used. For example, a cyan-yellow and a cyan-red has been shown to co-image cAMP and PKA dynamics in the same cell[47]. To image three FRET biosensors simultaneously in the same cell, application of a complex model of 3-D spectral unmixing has been demonstrated[48]. However, for most applications of multiplexed signaling measurements in live cells, single-color sensors are required.

In addition to limits on the multiplexing of genetically encodable biosensors, this approach is inherently limited in spatial resolution by the diffraction of visible light in fluorescence microscopy. The theoretical limit of spatial resolution for light microscopy is dependent on the wavelength of light and the numerical aperture of the condenser and objective and for most applications and is roughly 250 nm. Therefore, to observe signaling microdomains with features smaller or spaced closer than 250nm, new molecular tools are needed to be compatible with super-resolution techniques[49].

Histone Methylation and the Spatial Organization of the Nucleus

While phosphorylation is a key player in signal transduction pathways, PTMs also play a critical role in epigenetic regulation of the genome. This process is critical for establishing and maintaining cell-type identity by silencing the transcription of certain genes and enhancing expression of others. Genomic DNA wraps around an octomer of histone proteins, composed of two copies of histones H2A, H2B, H3, and H4, forming a nucleosome, which functions as a bead in the bead on a string chromatin structure. Another histone, H1, sits on top of the structure and participates in the formation of higher order structuring. The largely unstructured N- and C-terminal tails of histones protrude from the nucleosome and serve as regulators of DNA packing. Histone tails can facilitate binding with other nucleosomes or linker DNA regions as well as mediating the binding of other non-histone proteins to the chromatin. These processes are highly dependent on a large number of PTMs, such as methylation, acetylation, phosphorylation, ubiquitination, and citrullination at specific sites on the histone tails. These PTMs work together to provide a highly complex means of regulating chromatin structure and consequently gene expression.

Chromatin Structure and Organization

Loosely packaged chromatin called euchromatin maintains a beads on a string structure, with plenty of space to allow for transcription factor and polymerase binding, allowing transcription. However, for more silenced parts of the genome, the chromatin adopts a more highly condensed form called heterochromatin that is transcriptionally inactive. Arranging nucleosomes in a more compact configuration sterically occludes the binding of critical DNA-binding proteins essential for transcription, such as transcription factors and polymerase. Some regions of the genome, especially in gene-poor, repeat-rich areas, are found in heterochromatin in all cell-types, called constitutive heterochromatin. On the other hand, other regions are only in heterochromatin form in certain cell types, called facultative heterochromatin. Heterochromatin is found principally at telomeres, around the centromeres (pericentromeric) as well in small domains interspersed among euchromatin[50]. Its distribution within the nucleus depends highly on cell-type, but often is found on the nuclear periphery, as perinucleolar domains, or as large bodies within the nucleus[50]. These masses of heterochromatin in the interior of the nucleus include compact pericentromeric bodies as well larger bodies called chromocenters.

The Histone Code

Whether or not a segment of DNA is organized into euchromatin or heterochromatin depends largely on the interplay of PTMs on the histone tails. These PTMs may change the electric charge on the protein and in this way block particular electrostatic interactions. For example, acetylation of lysine residues on the histone tail neutralize the positive charge of the lysine, which weakens binding with DNA and other histones[51]. Likewise, phosphorylation adds negative charge to the histone tails and thus influences chromatin structure[52].

In addition to altering the electrostatics, PTMs on the histone tails also serve as docking sites for other proteins that regulate chromatin configuration. For example, lysine methylation recruits several chromatin factors, non-histone proteins that affect chromatin structure, often through enzymatic manipulation of PTMs or formation of complexes. Several protein domains mediate this recruitment, such as the Tudor "royal" family of domains (Tudor, chromodomains, PWWP, and MBT domains) as well as PHD fingers[52]. While acetylation generally favors enhancing transcription, histone methylation at particular sites has been known to either enhance or repress transcription in a site-specific way. However, the precise interplay of influences from each histone modification and how they work together to determine chromatin structure is exceedingly complex and only partially understood.

Histone 3 Tri-Methylated Lysine 9 (H3K9me3)

The tri-methylation of H3 at lysine 9 (H3K9me2/3) is a strong and well-studied marker of constitutive heterochromatin, especially when found in at pericentrosomic regions[53]. Two lysine methyltransferases, SUV39H1/2, are responsible for di- and tri-methylation of H3K9. These methyltransferases contain a chromodomain, allowing them to dock on the H3K9me3 PTM; however the mechanism of their original recruitment to pericentrosomic regions is unknown[53]. H3K9me3 also causes serves as a docking site for chromobox protein homolog 1 (CBX1), a member of the heterochromatin protein 1 (HP1) family[54]. The recruitment of CBX1 requires both H3K9me3 as well as binding to SUV39H[55]. CBX1 then recruits a large number of transcription regulators and chromatin modifying proteins[54]. Studies of the spatial distribution of H3Kme3 show that they exist in large (100 nm to 1µm sized) nanodomains, enriched at the nuclear periphery, around the nucleolus, and in the nucleoplasm[56].

Overview of Dissertation

This dissertation presents three novel technologies that expand our ability to study the spatial and temporal dynamics of PTMs in real time in live cells using genetically encodable fluorescent reporters. In Chapter 2, we present a suite of signaling activity reporters, called FLAREs, designed for multiplexed activity imaging. We then present another suite of signaling activity reporters in Chapter 3, called FLINC biosensors, which allow for monitoring of kinase activity at a sub-diffraction spatial resolution. Finally, in Chapter 4, we describe a novel genetically encodable histone modification probe for the H3K9me3 modification, to allow for sub-diffraction resolution maps of constitutive heterochromatin in live cells.

References

1. Khoury, G. A., Baliban, R. C. & Floudas, C. A. Proteome-wide post-translational modification statistics: frequency analysis and curation of the swiss-prot database. Sci. Rep. 1 (2011).
2. Manning, G., Whyte, D. B., Martinez, R., Hunter, T. & Sudarsanam, S. The protein kinase complement of the human genome. Science 298, 1912–34 (2002).
3. Kholodenko, B. N., Hancock, J. F. & Kolch, W. Signalling ballet in space and time. Nat. Rev. Mol. Cell Biol. 11, 414–26 (2010).
4. Rhee, A., Cheong, R. & Levchenko, A. Noise decomposition of intracellular biochemical signaling networks using nonequivalent reporters. Proc. Natl. Acad. Sci. U. S. A. 111, 17330–5 (2014).
5. Torres-Quesada, O., Mayrhofer, J. E. & Stefan, E. The many faces of compartmentalized PKA signalosomes. Cell. Signal. 37, 1–11 (2017).
6. Wong, W. & Scott, J. D. AKAP signalling complexes: focal points in space and time. Nat. Rev. Mol. Cell Biol. 5, 959–70 (2004).
7. Conti, M., Mika, D. & Richter, W. Cyclic AMP compartments and signaling specificity: role of cyclic nucleotide phosphodiesterases. J. Gen. Physiol. 143, 29–38 (2014).
8. DiPilato, L. M. & Zhang, J. The role of membrane microdomains in shaping beta2-adrenergic receptor-mediated cAMP dynamics. Mol. Biosyst. 5, 832–7 (2009).
9. Depry, C., Allen, M. D. & Zhang, J. Visualization of PKA activity in plasma membrane microdomains. Mol. Biosyst. 7, 52–8 (2011).
10. Crossthwaite, A. J. et al. The cytosolic domains of Ca2+-sensitive adenylyl cyclases

dictate their targeting to plasma membrane lipid rafts. J. Biol. Chem. 280, 6380–91 (2005).

11. Cooper, D. M. F. & Crossthwaite, A. J. Higher-order organization and regulation of adenylyl cyclases. Trends Pharmacol. Sci. 27, 426–31 (2006).
12. Agarwal, S. R. et al. Role of membrane microdomains in compartmentation of cAMP signaling. PLoS One 9, e95835 (2014).
13. Halls, M. L. & Cooper, D. M. F. Adenylyl cyclase signalling complexes - Pharmacological challenges and opportunities. Pharmacol. Ther. 172, 171–180 (2017).
14. Liu, S. et al. Phosphodiesterases coordinate cAMP propagation induced by two stimulatory G protein-coupled receptors in hearts. Proc. Natl. Acad. Sci. U. S. A. 109, 6578–83 (2012).
15. Oliveria, S. F., Dell'Acqua, M. L. & Sather, W. A. AKAP79/150 anchoring of calcineurin controls neuronal L-type Ca2+ channel activity and nuclear signaling. Neuron 55, 261–75 (2007).
16. Efendiev, R. et al. AKAP79 interacts with multiple adenylyl cyclase (AC) isoforms and scaffolds AC5 and -6 to alpha-amino-3-hydroxyl-5-methyl-4-isoxazole-propionate (AMPA) receptors. J. Biol. Chem. 285, 14450–8 (2010).
17. Gold, M. G. et al. Architecture and dynamics of an A-kinase anchoring protein 79 (AKAP79) signaling complex. Proc. Natl. Acad. Sci. U. S. A. 108, 6426–31 (2011).
18. Dell'Acqua, M. L., Faux, M. C., Thorburn, J., Thorburn, A. & Scott, J. D. Membrane-targeting sequences on AKAP79 bind phosphatidylinositol-4, 5-bisphosphate. EMBO J. 17, 2246–60 (1998).
19. Delint-Ramirez, I. et al. Palmitoylation targets AKAP79 protein to lipid rafts and

promotes its regulation of calcium-sensitive adenylyl cyclase type 8. J. Biol. Chem. 286, 32962–75 (2011).

20. Nguyen, T. T. et al. Co-regulation of the mitogen-activated protein kinase, extracellular signal-regulated kinase 1, and the 90-kDa ribosomal S6 kinase in PC12 cells. Distinct effects of the neurotrophic factor, nerve growth factor, and the mitogenic factor, epidermal growth. J. Biol. Chem. 268, 9803–10 (1993).
21. Marshall, C. J. Specificity of receptor tyrosine kinase signaling: transient versus sustained extracellular signal-regulated kinase activation. Cell 80, 179–85 (1995).
22. Ebisuya, M., Kondoh, K. & Nishida, E. The duration, magnitude and compartmentalization of ERK MAP kinase activity: mechanisms for providing signaling specificity. J. Cell Sci. 118, 2997–3002 (2005).
23. Avraham, R. & Yarden, Y. Feedback regulation of EGFR signalling: decision making by early and delayed loops. Nat. Rev. Mol. Cell Biol. 12, 104–17 (2011).
24. Corbit, K. C. et al. Activation of Raf-1 signaling by protein kinase C through a mechanism involving Raf kinase inhibitory protein. J. Biol. Chem. 278, 1306Ro1–8 (2003).
25. Santos, S. D. M., Verveer, P. J. & Bastiaens, P. I. H. Growth factor-induced MAPK network topology shapes Erk response determining PC-12 cell fate. Nat. Cell Biol. 9, 324–30 (2007).
26. Herbst, K. J., Allen, M. D. & Zhang, J. Spatiotemporally regulated protein kinase A activity is a critical regulator of growth factor-stimulated extracellular signal-regulated kinase signaling in PC12 cells. Mol. Cell. Biol. 31, 4063–75 (2011).
27. Robinson, M. J., Stippec, S. A., Goldsmith, E., White, M. A. & Cobb, M. H. A

constitutively active and nuclear form of the MAP kinase ERK2 is sufficient for neurite outgrowth and cell transformation. Curr. Biol. 8, 1141–50 (1998).

28. Mebratu, Y. & Tesfaigzi, Y. How ERK1/2 activation controls cell proliferation and cell death: Is subcellular localization the answer? Cell Cycle 8, 1168–75 (2009).
29. Casar, B. & Crespo, P. ERK Signals: Scaffolding Scaffolds? Front. cell Dev. Biol. 4, 49 (2016).
30. Roy, F. & Therrien, M. MAP kinase module: the Ksr connection. Curr. Biol. 12, R325–7 (2002).
31. Casar, B. & Crespo, P. MEK Binding to KSR Promotes Allosteric Activation of BRAF. Cancer Discov. 8, 385 (2018).
32. Oldach, L. & Zhang, J. Genetically encoded fluorescent biosensors for live-cell visualization of protein phosphorylation. Chem. Biol. 21, 186–197 (2014).
33. Isotani, E. et al. Real-time evaluation of myosin light chain kinase activation in smooth muscle tissues from a transgenic calmodulin-biosensor mouse. Proc. Natl. Acad. Sci. U. S. A. 101, 6279–6284 (2004).
34. Geguchadze, R. et al. Quantitative measurements of Ca(2+)/calmodulin binding and activation of myosin light chain kinase in cells. FEBS Lett. 557, 121–4 (2004).
35. Zhang, J., Ma, Y., Taylor, S. S. & Tsien, R. Y. Genetically encoded reporters of protein kinase A activity reveal impact of substrate tethering. Proc. Natl. Acad. Sci. U. S. A. 98, 14997–5002 (2001).
36. Harvey, C. D. et al. A genetically encoded fluorescent sensor of ERK activity. Proc. Natl. Acad. Sci. U. S. A. 105, 19264–9 (2008).
37. Violin, J. D., Zhang, J., Tsien, R. Y. & Newton, A. C. A genetically encoded

fluorescent reporter reveals oscillatory phosphorylation by protein kinase C. J. Cell Biol. 161, 899–909 (2003).

38. Nakai, J., Ohkura, M. & Imoto, K. A high signal-to-noise Ca(2+) probe composed of a single green fluorescent protein. Nat. Biotechnol. 19, 137–41 (2001).
39. Chen, T.-W. et al. Ultrasensitive fluorescent proteins for imaging neuronal activity. Nature 499, 295–300 (2013).
40. Kawai, Y., Sato, M. & Umezawa, Y. Single color fluorescent indicators of protein phosphorylation for multicolor imaging of intracellular signal flow dynamics. Anal. Chem. 76, 6144–9 (2004).
41. Kerppola, T. K. Bimolecular fluorescence complementation (BiFC) analysis as a probe of protein interactions in living cells. Annu. Rev. Biophys. 37, 465–87 (2008).
42. Herbst, K. J., Allen, M. D. & Zhang, J. Luminescent kinase activity biosensors based on a versatile bimolecular switch. J. Am. Chem. Soc. 133, 5676–9 (2011).
43. Alford, S. C., Abdelfattah, A. S., Ding, Y. & Campbell, R. E. A fluorogenic red fluorescent protein heterodimer. Chem. Biol. 19, 353–60 (2012).
44. Alford, S. C., Ding, Y., Simmen, T. & Campbell, R. E. Dimerization-dependent green and yellow fluorescent proteins. ACS Synth. Biol. 1, 569–75 (2012).
45. Ding, Y. et al. Ratiometric biosensors based on dimerization-dependent fluorescent protein exchange. Nat. Methods 12, 195–8 (2015).
46. Shcherbakova, D. M., Hink, M. A., Joosen, L., Gadella, T. W. J. & Verkhusha, V. V. An orange fluorescent protein with a large Stokes shift for single-excitation multicolor FCCS and FRET imaging. J. Am. Chem. Soc. 134, 7913–23 (2012).
47. Aye-Han, N.-N., Allen, M. D., Ni, Q. & Zhangy, J. Parallel tracking of cAMP and

PKA signaling dynamics in living cells with FRET-based fluorescent biosensors. Mol. Biosyst. 8, 1435–1440 (2012).

48. Woehler, A. Simultaneous quantitative live cell imaging of multiple FRET-based biosensors. PLoS One 8, e61096 (2013).
49. Sydor, A. M., Czymmek, K. J., Puchner, E. M. & Mennella, V. Super-Resolution Microscopy: From Single Molecules to Supramolecular Assemblies. Trends Cell Biol. 25, 730–48 (2015).
50. Janssen, A., Colmenares, S. U. & Karpen, G. H. Heterochromatin: Guardian of the Genome. Annu. Rev. Cell Dev. Biol. (2018). doi:10.1146/annurev-cellbio-100617-062653
51. Zhang, T., Cooper, S. & Brockdorff, N. The interplay of histone modifications - writers that read. EMBO Rep. 16, 1467–81 (2015).
52. Bannister, A. J. & Kouzarides, T. Regulation of chromatin by histone modifications. Cell Res. 21, 381–95 (2011).
53. Saksouk, N., Simboeck, E. & Déjardin, J. Constitutive heterochromatin formation and transcription in mammals. Epigenetics Chromatin 8, 3 (2015).
54. Lomberk, G., Wallrath, L. & Urrutia, R. The Heterochromatin Protein 1 family. Genome Biol. 7, 228 (2006).
55. Stewart, M. D., Li, J. & Wong, J. Relationship between histone H3 lysine 9 methylation, transcription repression, and heterochromatin protein 1 recruitment. Mol. Cell. Biol. 25, 2525–38 (2005).

56. Xu, J. et al. Super-Resolution Imaging of Higher-Order Chromatin Structures at Different Epigenomic States in Single Mammalian Cells. Cell Rep. 24, 873–882 (2018).

Chapter 2 Single-Color, Ratiometric Biosensors for Detecting Signaling Activities in Live Cells

A version of this chapter has been published, and appears in:

B. L. Ross, B. Tenner, M. L. Markwardt, A. Zviman, G. Shi, J. P. Kerr, N. Snell, J. McFarland, J. Mauban, C. W. Ward, M. A. Rizzo, J. Zhang. "Single-Color, Ratiometric Biosensors for Detecting Signaling Activities in Live Cells." *eLife*, 7: e35458 (2018).

Abstract

Genetically encoded fluorescent biosensors have revolutionized the study of signal transduction by enabling the real-time tracking of signaling activities in live cells. Investigating the interaction between signaling networks has become increasingly important to understanding complex cellular phenomena, necessitating an update of the biosensor toolkit to allow monitoring and perturbing multiple activities simultaneously in the same cell. We therefore developed a new class of fluorescent biosensors based on homo-FRET, called FLuorescence Anisotropy REporters (FLAREs), which combine the multiplexing ability of single-color sensors with a quantitative, ratiometric readout. Using an array of color variants, we were able to demonstrate multiplexed imaging of three activity reporters simultaneously in the same cell. We further demonstrate the compatibility of FLAREs for use with optogenetic tools as well as intravital two-photon imaging.

Introduction

Genetically encoded biosensors have revolutionized the study of cell signaling by allowing the real-time monitoring of signaling activities, such as enzymatic activity or the release of second messengers, in live cells. They are therefore critical tools for uncovering the precise spatial and temporal regulation of signal transduction cascades. These biosensors can be divided into two broad classes: single-color and ratiometric. Single-color sensors, with an intensiometric activity readout, only occupy a single color channel, allowing for more flexibility in multiplexed imaging experiments. However, they are sensitive to variations in probe concentration caused by changing expression levels or cell shape, as well as differences in imaging conditions, such as illumination intensity and focus. On the other hand, sensors with a ratiometric readout, such as those based on Förster Resonance Energy Transfer (FRET), cancel out many of these variations, enabling quantitative measurements of second messenger concentrations and better comparisons between experiments. However, the requirement for two distinct color channels limits their application in multiplexed imaging.

We therefore aimed to develop sensors that only occupy a single channel while still cancelling out the effects of varying imaging conditions and probe concentrations. Hence, rather than use the emission ratio between the FRET and donor channels, we instead used the loss of polarization of emitted light as a readout for FRET between two fluorescent proteins (FPs). Because this approach does not require the donor and acceptor to have distinct emission wavelengths, it can be used for either hetero-FRET (e.g., between different chromophores) or homo-FRET (e.g., between identical chromophores). Homo-FRET measurements have been useful for detecting protein clustering and protein oligomerization in live cells[1,2,3], but only recently has the possibility of using homo-FRET in biosensor designs been explored[4,5]. Here we describe the development of a panel of single-color, genetically encodable biosensors based on homo-FRET for detecting kinase activity and second messenger dynamics. We call these sensors FLuorescence Anisotropy REporters, or FLAREs.

Results and Discussion

Development of a Family of FLARE PKA Sensor

To create our FLARE probes, we adapted existing FRET-based biosensors for homo-FRET measurements by replacing the traditional FRET pair with two FPs of the same color. The resulting biosensors include a molecular switch, which changes conformation in the presence of a particular biochemical activity, flanked by two spectrally similar FPs at the N- and C-termini. Changes in the conformation of the molecular switch, and thus the biochemical activities under study, are then monitored by observing the fluorescence anisotropy of the sensor using fluorescence polarization microscopy, with increased anisotropy corresponding to a lower-FRET state of the sensor, similar to the effect of increasing the intramolecular distance between the FRET pair (Figure 2.1).

To develop a Protein Kinase A (PKA) activity FLARE, the molecular switch from A Kinase Activity Reporter 4 (AKAR4)[6,7], composed of an FHA1 domain and PKA substrate (Figure 2.2a), was flanked between two FPs of the same color. The FHA1 domain binds to the PKA substrate when the latter is phosphorylated, altering the conformation of the molecular switch and leading to a change in FRET between the flanking homo-FRET pair. To test the effect of FP circular permutation on these biosensors, we developed two FLARE-AKAR variants based on the yellow FP mVenus: one in which the C-terminal FP was circularly permuted at position 172 (cp172Venus), consistent with the hetero-FRET AKAR4 sensor, and one without circular permutation. We expressed mVenus-cp172Venus FLARE-AKAR in HEK293T cells and captured a time-course using fluorescence polarization microscopy. Following PKA activation using a cocktail of 50 µM forskolin (Fsk), an adenylyl cyclase activator, and 100 µM 3-isobutyl-1-methylxanthine (IBMX), a general phosphodiesterase inhibitor, the anisotropy decreased from 0.29±0.003 to 0.26±0.003, a decrease of 0.028±0.001 (N=44 (mean anisotropy of individual cells [biological replicates], unpaired, two-tailed t-test, $p<0.0001$), with the kinetics of the decrease matching those observed with AKAR4 (Figure 2.2b, Figure 2.3a). The yellow variant without the circular-permutation in the C-terminal FP showed slightly reduced changes in anisotropy upon stimulation with Fsk/IBMX (Figure 2.2c, Figure 2.3c), consistent with previous observations in hetero-FRET-based biosensors[8,9,10]. We observed a slight positive correlation between intensity and anisotropy change for Venus-cp172Venus FLARE AKAR; however the expression level does not significantly impact the reporting ability of these sensors in general (Figure 2.4a). The signal-to-noise ratio (SNR) of Venus-cp172Venus FLARE-AKAR was calculated to be 32 by dividing the magnitude of the anisotropy change upon maximal PKA stimulation by the standard deviation of the baseline before stimulation.

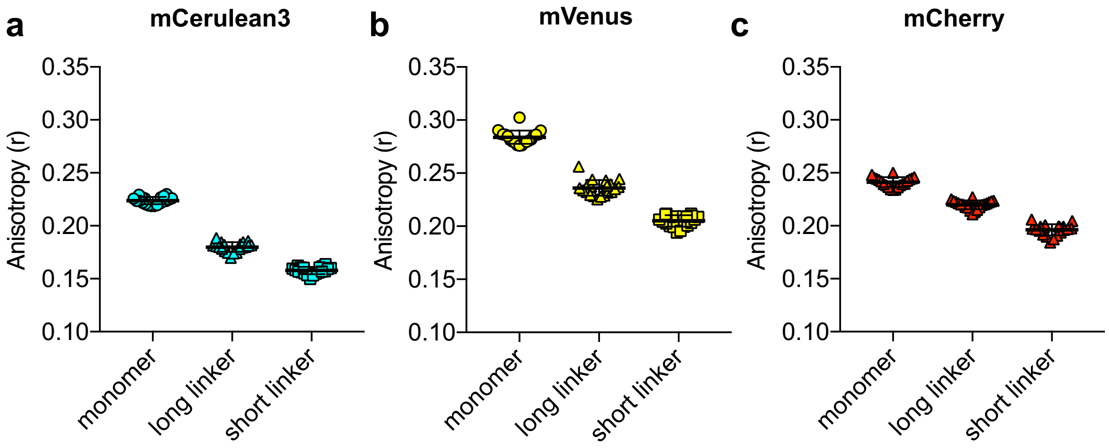

Figure 2.1 Anisotropy *vs*. Intramolecular Distance

Anisotropy measurements of monomer, as well as tandem dimers separated by either a long (44 amino acid) or a short (10 amino acid) linker, of a). mCerulean3, b). mVenus, and c). mCherry. Data points reflect the mean intensity of individual cells (biological replicates). The mean for each is shown, with the error reflecting the standard error of the mean.

.

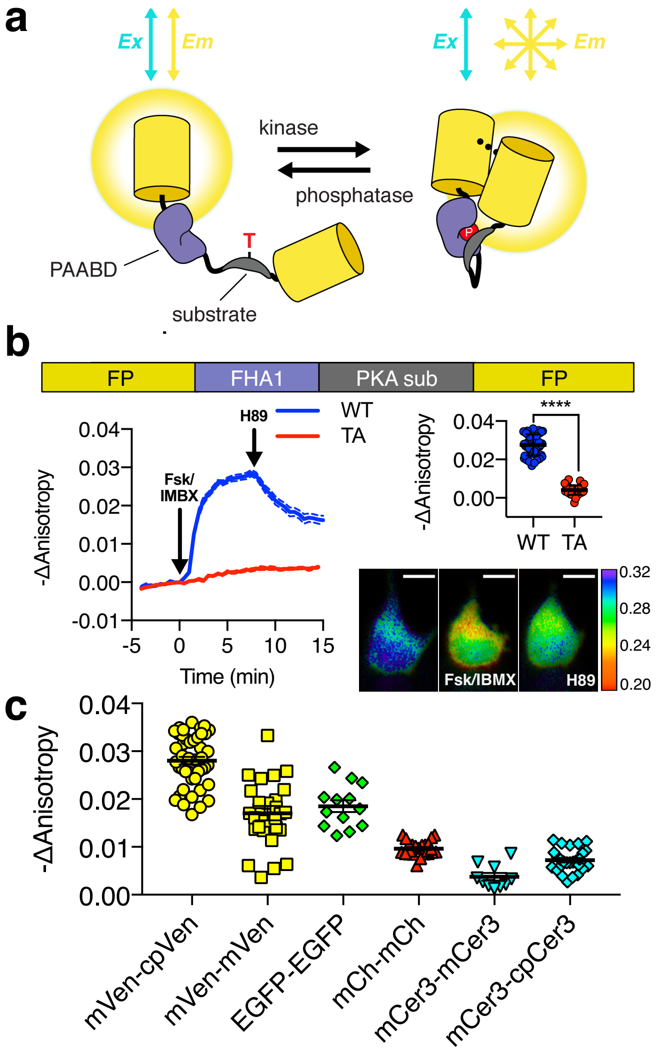

Figure 2.2 Development and Characterization of FLARE AKAR

a). Schematic of a kinase activity FLARE b). Diagram illustrating domain structure of FLARE-AKAR (top). Time-course of mean fluorescence anisotropy of Venus-cp172Venus FLARE-AKAR wild type (blue, N=44) and kinase insensitive T-to-A mutant (red, N=38) expressed in HEK293T cell, stimulated with 50 µM forskolin and 100 µM IBMX at t=0 min, and 20 µM H-89 at t=24 min (left). Dashed lines above and below represent standard error of the mean. Changes in anisotropy upon Fsk/IBMX

Figure 2.2 (continued) stimulation for both FLARE-AKAR WT and T-to-A mutant (upper right, two-tailed t-test, $p<0.0001$), calculated as the difference between the mean anisotropy from t=5 min to t=7.5 min and the mean anisotropy of the baseline before drug addition. The mean for each is shown, with the error reflecting the standard error of the mean. Representative anisotropy pseudocolor image before Fsk/IBMX stimulation (t=0 min), after Fsk/IBMX stimulation (t=7.5 min), and after inhibition of PKA with H-89 (t=24 min) (lower right) c). Comparison of the magnitude of the anisotropy change for different color variants of FLARE-AKAR upon stimulation with Fsk/IBMX including Venus-cp172Venus AKAR (N=44), Venus-Venus FLARE AKAR (N=32), EGFP-EGFP FLARE AKAR (N=13), mCh-mCh FLARE AKAR (N=22), mCerulean3 FLARE-AKAR (N=10), and mCerulean3-cp173Cerulean FLARE-AKAR (N=26). N numbers reflect the mean intensity of individual cells (biological replicates). The mean for each is shown, with the error reflecting the standard error of the mean.

Figure 2.3 Single Cell Traces for FLARE AKAR Variants

Individual and average traces for FLARE-AKAR variants, including a). Venus-cp172Venus AKAR (N=44), b). Venus-cp172Venus FLARE-AKAR T/A mutant (N=38), c). Venus-Venus FLARE AKAR (N=32), d). EGFP-EGFP FLARE AKAR (N=13), e). mCh-mCh FLARE AKAR (N=22), f). mCerulean3-mCerulean3 FLARE-AKAR (N=10), and g). mCerulean3-cp173Cerulean FLARE-AKAR (N=26). Gray lines are individual cell traces, while the red solid line is the average curve. N numbers reflect the mean intensity of individual cells (biological replicates). Red dotted lines represent the average curve plus or minus the standard error of the mean.

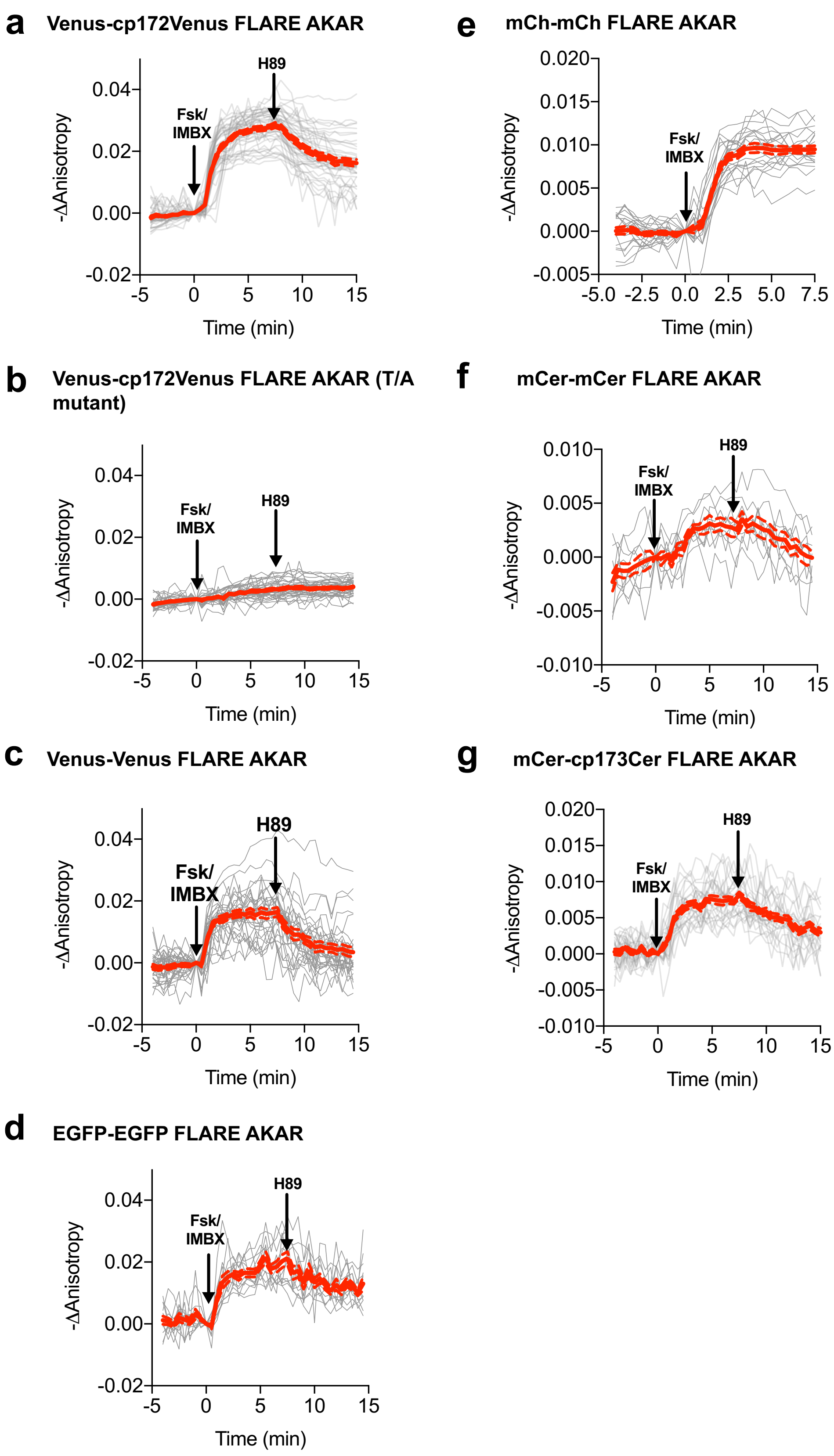
a
Venus-cp172Venus FLARE AKAR
-ΔAnisotropy
0.04
0.02
0.00
-0.02
H89
Fsk/
IMBX
-5
0
5
10
15
Time (min)
b
Venus-cp172Venus FLARE AKAR (T/A mutant)
-ΔAnisotropy
0.04
0.02
0.00
-0.02
Fsk/
IMBX
H89
-5
0
5
10
15
Time (min)
c
Venus-Venus FLARE AKAR
-ΔAnisotropy
0.04
0.02
0.00
-0.02
H89
Fsk/
IMBX
-5
0
5
10
15
Time (min)
d
EGFP-EGFP FLARE AKAR
-ΔAnisotropy
0.04
0.02
0.00
-0.02
H89
Fsk/
IMBX
-5
0
5
10
15
Time (min)
e
mCh-mCh FLARE AKAR
-ΔAnisotropy
0.020
0.015
0.010
0.005
0.000
-0.005
Fsk/
IMBX
-5.0
-2.5
0.0
2.5
5.0
7.5
Time (min)
f
mCer-mCer FLARE AKAR
-ΔAnisotropy
0.010
0.005
0.000
-0.005
-0.010
H89
Fsk/
IMBX
-5
0
5
10
15
Time (min)
g
mCer-cp173Cer FLARE AKAR
-ΔAnisotropy
0.020
0.015
0.010
0.005
0.000
-0.005
-0.010
H89
Fsk/
IMBX
-5
0
5
10
15
Time (min)

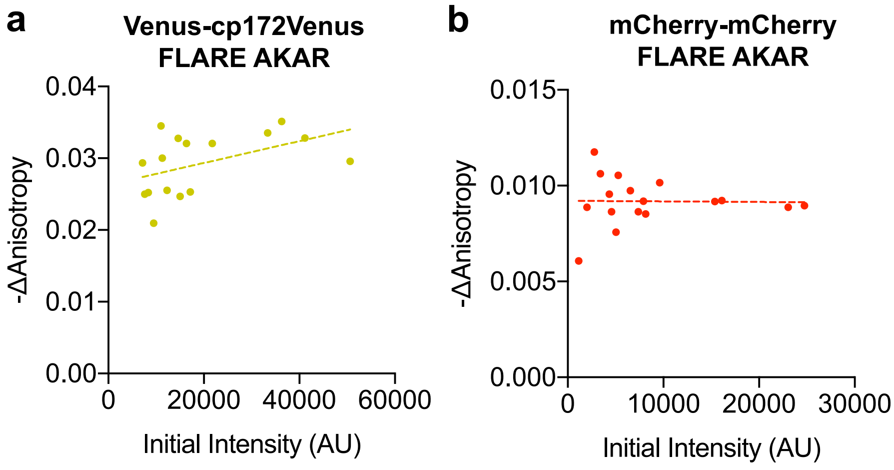

Figure 2.4 Signal vs Expression Level for FLARE AKAR

Scatter plots showing the relationship between the magnitude of the anisotropy change after treatment with 50µM forskolin and 100µM IBMX and the initial intensity for a). Venus-cp172Venus FLARE AKAR and b). mCherry-mCherry FLARE AKAR, in HEK293-T cells. The magnitude of the signal was calculated by taking the mean anisotropy from t = 5min to t = 7.5 min and subtracting the mean anisotropy of the baseline before drug addition.

Subsequent control experiments confirmed that this change in anisotropy is caused by a change in the FRET state due to the conformational change of the sensor upon stimulation of PKA activity. PKA inhibition using 20 μM H-89 led to an immediate slope change and increase in anisotropy (Figure 2.2b). On the other hand, a mutant version of the biosensor with a threonine-to-alanine (T-to-A) mutation at the phosphorylation site showed no change in anisotropy upon PKA stimulation with Fsk/IBMX or inhibition with H-89 (Figure 2.2b, Figure 2.3b), suggesting that the observed changes in anisotropy were due to phosphorylation of the PKA substrate. Furthermore, isoproterenol, a β-adrenergic agonist, induced FLARE-AKAR responses in a dose-dependent manner (Figure 2.5). To further demonstrate that the change in anisotropy upon PKA stimulation was due to a change in FRET, we mutated the chromophore of the C-terminal cp172Venus in Venus-cp172Venus FLARE AKAR from GYG to GGG. We observed that the magnitude of the response to Fsk/IBMX decreased to approximately one-third of that of the wild-type sensor (Figure 2.6). The remaining response was likely due to intermolecular FRET that occurs when the FHA1 domain of one molecule binds to the phosphorylated PKA substrate in an adjacent molecule.

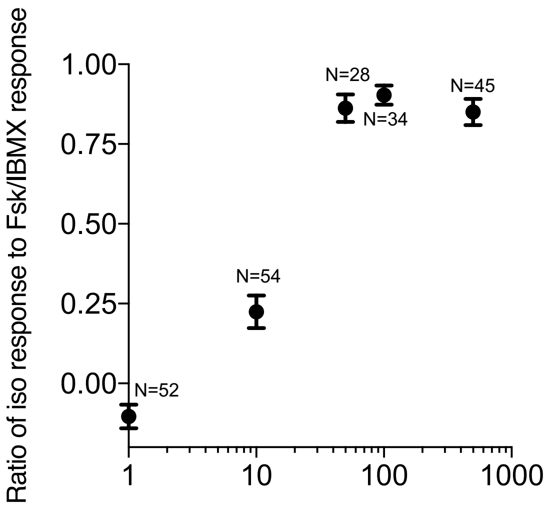

Figure 2.5 Venus-cp172 Venus isoproterenol dose response

HEK293-T cells were transiently transfected with Venus-cp172Venus FLARE-AKAR, and stimulated with varying doses of isoproterenol, followed by maximal stimulation with 50 μM forskolin and 100 μM IBMX. The ratio of the anisotropy decrease following isoproterenol dose to that after Forskolin and IBMX stimulation vs. the isoproterenol dose is plotted. Error bars reflect the standard error of the mean.

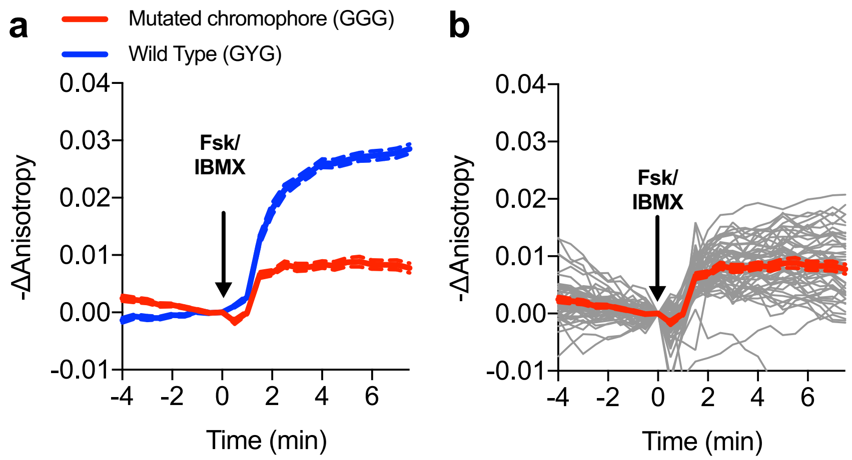

Figure 2.6 Characterization of the chromophore-dead FLARE AKAR mutant

a). Comparison of Venus-cp172Venus FLARE AKAR responses of the wild type sensor and a mutant sensor in which the chromophore of the C-terminal cp172Venus was mutated from GYG to GGG (N=53), expressed in HEK293-T cells and treated with 50µM forskolin and 100µM IBMX. b). Individual cell traces for Venus-cp172Venus FLARE AKAR (GGG mutant). The red curve represents the mean for all the cell traces, with the dotted lines above and below reflecting the standard error of the mean.

In addition to the yellow sensors, we developed a panel of color variants of FLARE-AKAR, including EGFP-EGFP, mCherry-mCherry, mCerulean3-mCerulean3[11], and mCerulean3-cp173Cerulean3 versions. All of these variants exhibited a decrease in anisotropy in cells treated with Fsk/IBMX; however, the magnitude of the anisotropy decrease depended on the choice of FP, with the mVenus-cp172Venus variant having the largest response (Figure 2.2c, Figure 2.3). As with the Venus variants, the Cerulean3-based FLARE-AKAR showed an increased dynamic range with a circularly-permutated fluorescent protein at the C-terminal position. mCherry-mCherry FLARE-AKAR, being spectrally shifted from the AKAR4 heteroFRET sensor allowed for direct comparison of FLARE and heteroFRET sensors within the same cell. As shown in Figure 2.7, changes in anisotropy in mCherry-mCherry FLARE-AKAR corresponded with the changes in normalized emission ratio in AKAR4, with similar kinetics.

We furthermore demonstrated the ability of FLARE-AKAR sensors to monitor kinase activity at particular subcellular compartments. By fusing Venus-cp172Venus FLARE-AKAR to targeting motifs from Lyn kinase and DAKAP1, we were able to detect PKA activity at the plasma membrane and outer mitochondrial membrane, respectively (Figure 2.8). Moreover, we used untargeted FLARE sensors to detect differential PKA activity dynamics in different compartments; diffusable Venus-cp172Venus FLARE AKAR in HeLa showed that PKA activity has slower kinetics and a lower magnitude in the nucleus than the cytosol (Figure 2.9).

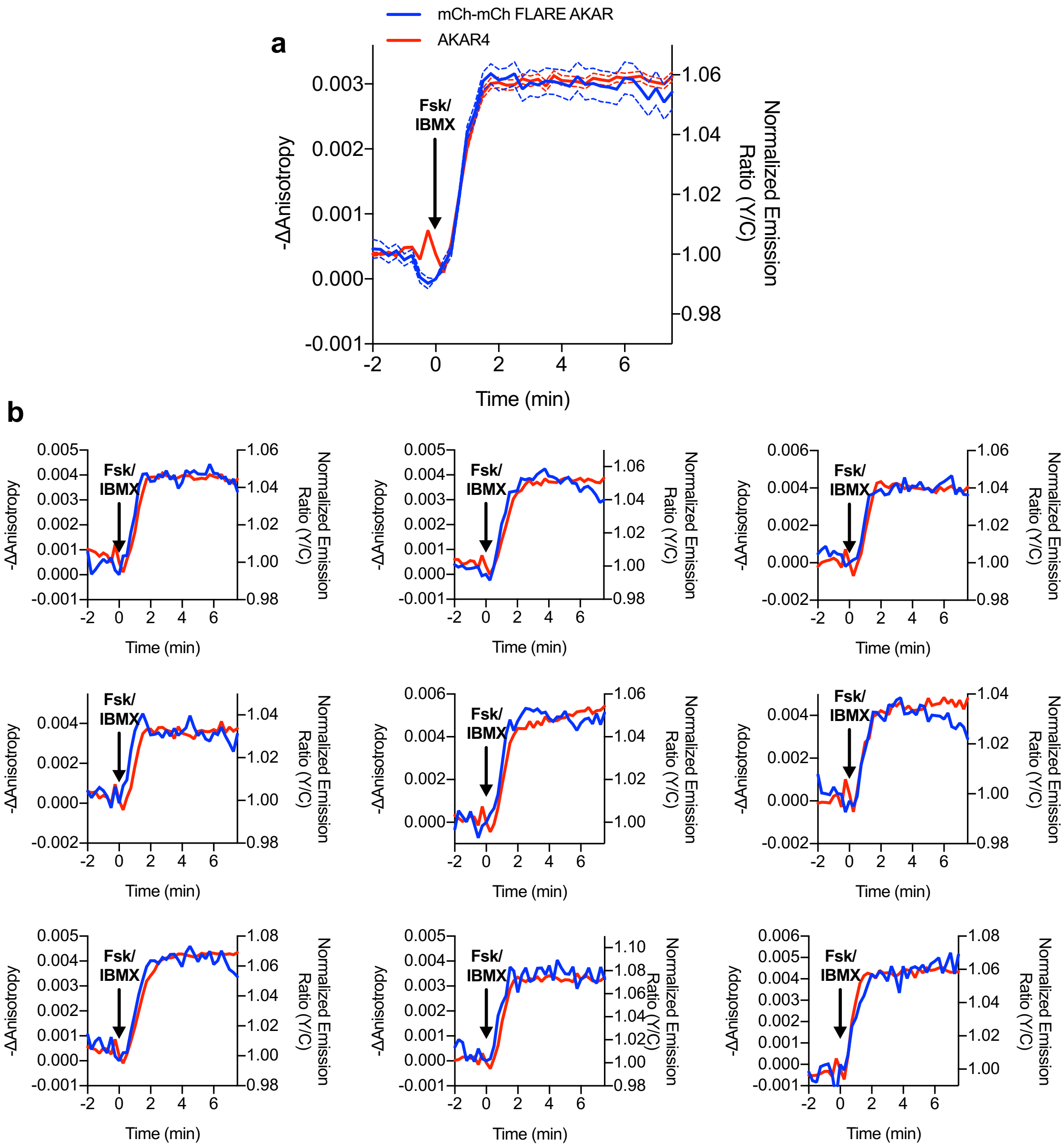

Figure 2.7 Direct comparison of FLARE and heteroFRET AKAR sensor

mCherry-mCherry FLARE-AKAR and AKAR4 were co-expressed in HEK cells, which were stimulated with 50µM forskolin and 100µM IBMX at t=0 min (N=74). a). Average anisotropy traces for mCherry-mCherry

FLARE AKAR and average normalized emission ratio traces are shown for AKAR4. The dashed lines above and below the curve represent the standard error of the mean. b). Nine representative cell traces showing both mCherry-mCherry FLARE AKAR and AKAR4 traces for the above experiment.

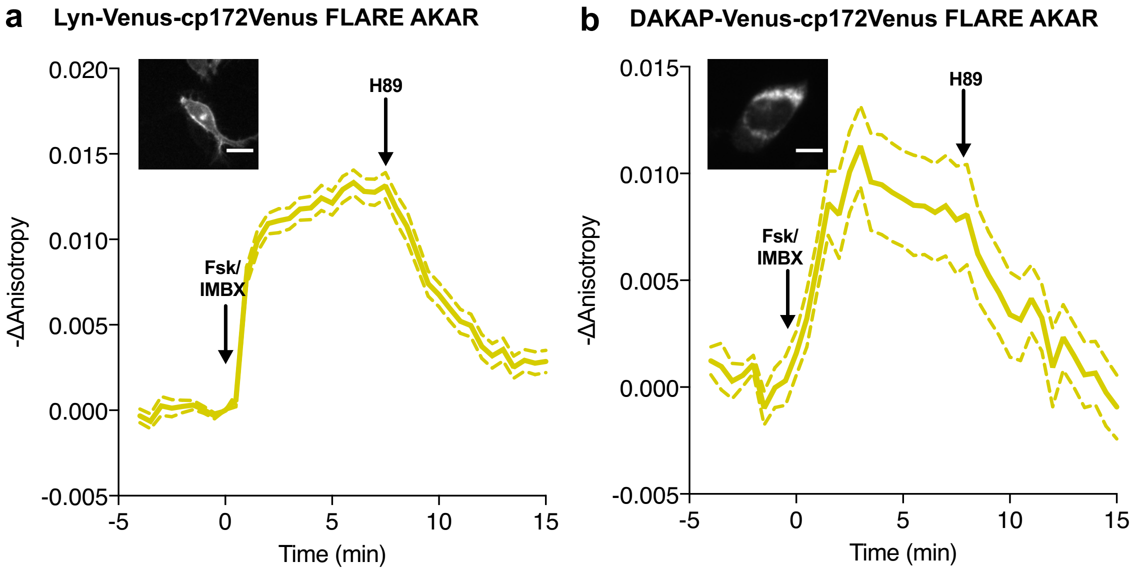

Figure 2.8 Subcellular targeted FLARE-AKARs.

Average anisotropy traces of Venus-cp172Venus FLARE AKAR subcellularly targeted to a) the plasma membrane with the Lyn-kinase targeting motif (N=77) b) the mitochondrial membrane with the targeting sequence from DAKAP (N=32), expressed in HEK cells stimulated with 50 µM forskolin and 100 µM IBMX at t=0 min, and 20 µM H89 at t=7.5 min. Scale bars are 10 µm. Dashed lines above and below the curves reflect the standard error of the mean.

Figure 2.9 Differential PKA activity kinetics in the cytosol and the nucleus

a). Comparison of Venus-cp172Venus FLARE AKAR anisotropy changes in the cytosol and the nucleus in HeLa cells treated with 50μM forskolin and 100μM IBMX (N=19). Dashed lines above and below the curves reflect the standard error of the mean. b). Comparison of the time for the anisotropy change to peak or plateau in the cytosol and the nucleus (two-tailed paired T-test, $p=0.0295$). c). Comparison of the time for the anisotropy change to reach half of the peak ($t_{1/2}$) in the cytosol and the nucleus (two-tailed paired T-test, $p=0.0065$). d). Comparison of the magnitude of the anisotropy change in the cytosol and the nucleus (two-tailed, paired T-test, $p<0.0001$). e). Eight representative anisotropy time traces for individual cells, comparing the cytosolic and nuclear anisotropies.

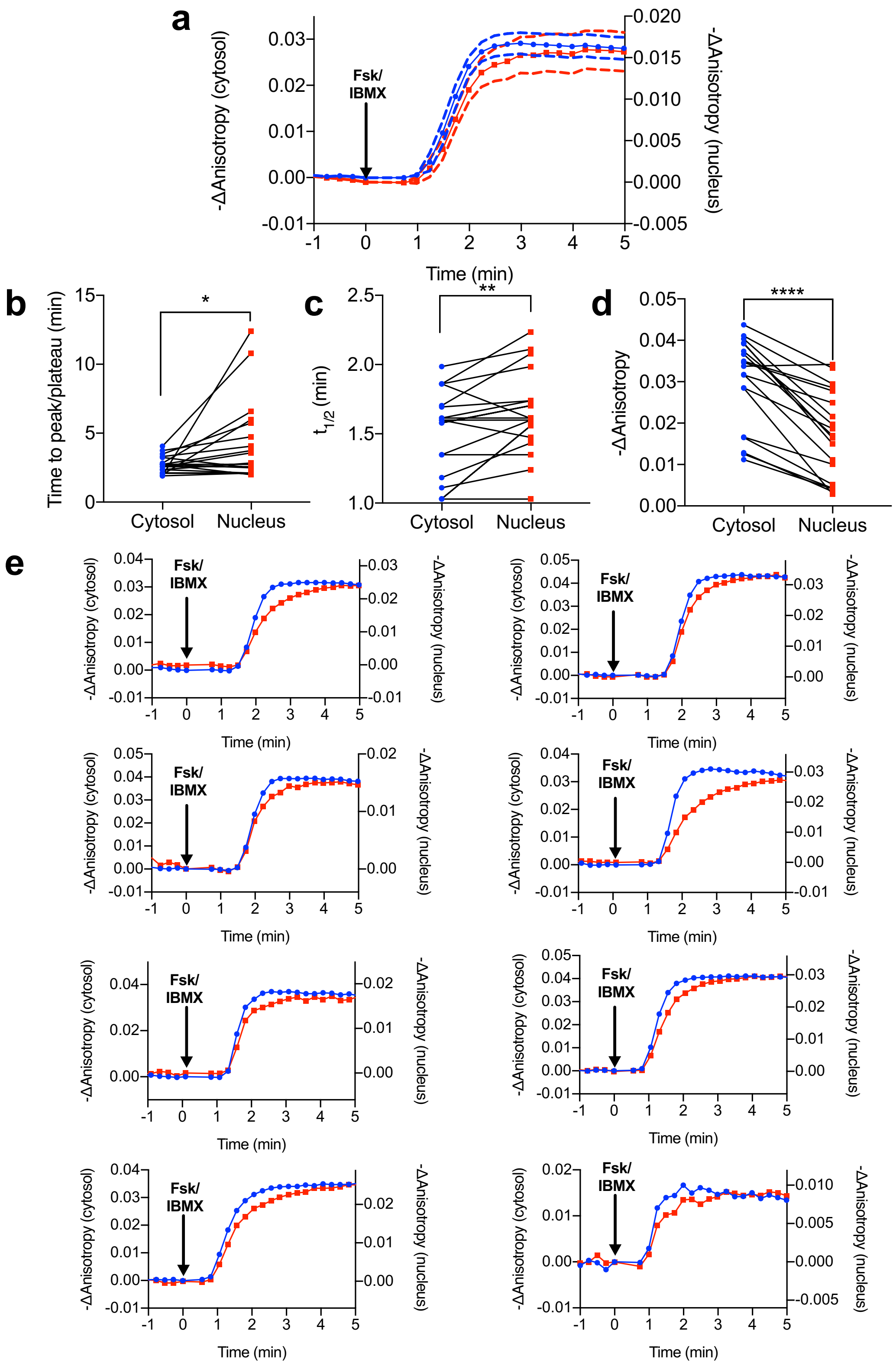
a
-ΔAnisotropy (cytosol)
-ΔAnisotropy (nucleus)
Fsk/
IBMX
Time (min)
0.03
0.02
0.01
0.00
-0.01
0.020
0.015
0.010
0.005
0.000
-0.005
-1
0
1
2
3
4
5
b
Time to peak/plateau (min)
*
15
10
5
0
Cytosol
Nucleus
c
$t_{1/2}$ (min)
**
2.5
2.0
1.5
1.0
Cytosol
Nucleus
d
-ΔAnisotropy
****
0.05
0.04
0.03
0.02
0.01
0.00
Cytosol
Nucleus
e
-ΔAnisotropy (cytosol)
-ΔAnisotropy (nucleus)
Fsk/
IBMX
Time (min)

Generalizing the FLARE Design to Other Kinase Activity and Activation Biosensors

To demonstrate the generalizability of FLAREs, we developed a family of single-color kinase activity or activation reporters in various colors (Figure 2.10). To construct a single-color Erk activity biosensor, we replaced the PKA sensor domain from Venus-cp172Venus FLARE-AKAR with the sensor domain from EKAR-EV, composed of a WW domain (PAABD), a flexible EV linker, and an Erk substrate peptide (Figure 2.10a)[12,13]. When expressed in HEK293T cells, Venus-cp172Venus FLARE-EKAR-EV exhibited a decrease in anisotropy of 0.02±0.001 (N=13) after treatment with 100 ng/mL epidermal growth factor (EGF) to activate the MAPK pathway (Figure 2.10a, Figure 2.11). This response was reversed upon MEK inhibition using 20 μM U0126, and no change in anisotropy was observed with a T-to-A mutant sensor. Likewise, we developed a panel of PKC activity reporters, called FLARE-CKARs, by flanking a PKC sensor domain composed of an FHA1 domain and a PKC substrate[14] from a CKAR2 construct (Figure 2.12) with mVenus-cp172Venus. We observed an anisotropy decrease of 0.02±0.001 (N=26) upon activation of PKC with 100 ng/mL phorbol 12-myristate 13-acetate (PMA) (Figure 2.10b, Figure 2.13). For both FLARE-EKAR (Figure 2.11) and FLARE CKAR (Figure 2.13), we likewise repeated this process for various color variants, and like the FLARE-AKARs, the sensors based on mVenus exhibited the largest responses. Furthermore, a myosin light chain kinase (MLCK) sensor was converted to a FLARE by exchanging the cyan FP for mVenus[15]. Calmodulin (CaM) association with the MLCK-CaM binding domain in between the FPs decreases FRET, leading to an increase in fluorescence anisotropy upon forced calcium (Ca^{2+}) entry with 30 mM KCl (N=13) (Figure 2.10b, Figure 2.14).

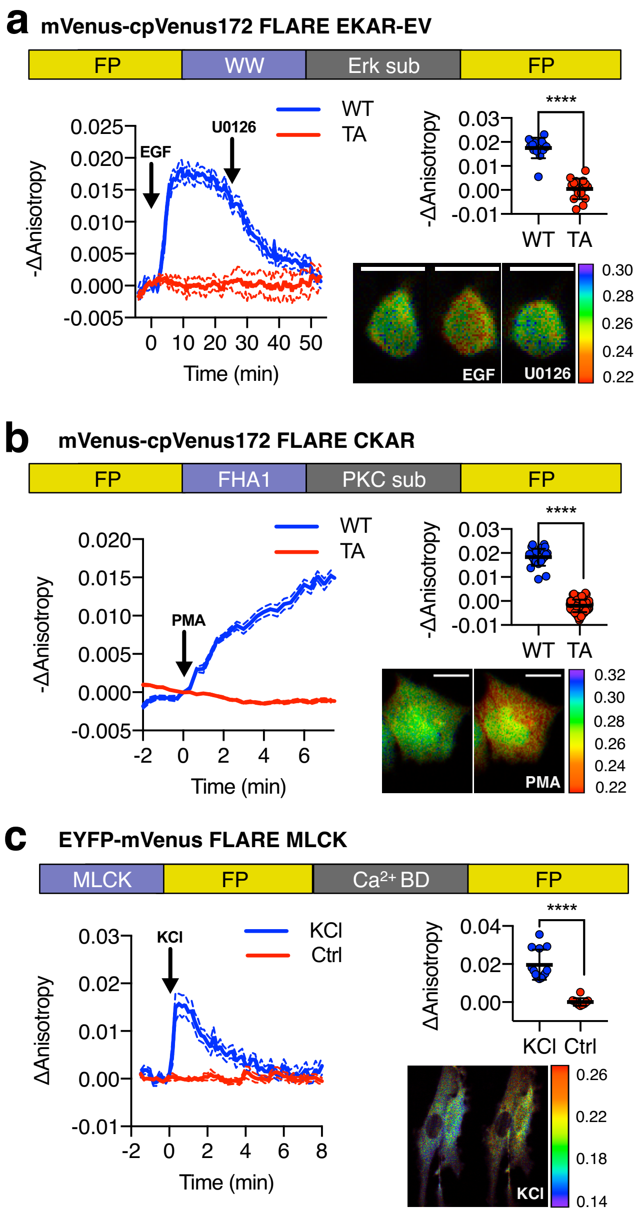

Figure 2.10 A panel of kinase activity and activation sensors

a). Domain structure of FLARE-EKAR-EV (above). Time-course of mean fluorescence anisotropy of Venus-cp172Venus FLARE-EKAR-EV WT (blue, N=13) and kinase-insensitive mutant (red, N=16) expressed in HEK293T cell, with addition of 100 ng/mL EGF at t=0min and 20 μM U0126 at t=25min (left). Summary of anisotropy changes (upper right,

Figure 2.10 (continued) two-tailed t-test, $p<0.0001$), calculated as the difference between the mean anisotropy from $t=10$ min to $t=15$ min and the mean anisotropy of the baseline before drug addition. The mean is shown, with the error reflecting the standard error of the mean. Representative anisotropy pseudocolor image before EGF stimulation ($t=0$ min), after EGF stimulation ($t=25$ min), and after inhibition of MEK with U0126 ($t=47.5$ min) (lower right). b). Domain structure of FLARE-CKAR (above). Time-course of fluorescence anisotropy of Venus-cp172Venus FLARE-CKAR WT (blue, N=26) and kinase-insensitive mutant (red, N=119) with addition of 100 ng/mL phorbol 12-myristate 13-acetate (PMA) at $t=0$min. Summary of response magnitudes (upper right, two-tailed t-test, $p<0.0001$), calculated as the difference between the mean anisotropy from $t = 10$ to $t = 11.33$ min and the mean anisotropy of the baseline before drug addition. The mean is shown, with the error reflecting the standard error of the mean. Representative anisotropy pseudocolor image before PMA addition ($t=0$ min) and after PMA addition ($t=15$ min). c). Domain structure of FLARE-MLCK (top). Anisotropy time course of a representative REF52 cell expressing YFP-Venus FLARE-MLCK treated with 30 mM KCl at $t=0$ (N=13, blue), or vehicle control (N=10). Summary of anisotropy changes, calculated as the mean difference between the anisotropy at $t = 0.333$ min and the anisotropy of the baseline, before KCl addition (upper right, two-tailed t-test, $p<0.0001$). Representative pseudocolor anisotropy images before and after KCl treatment (lower

Figure 2.10 (continued) right). Dashed lines above and below time course traces reflect the standard error of the mean. FP, fluorescent protein; CaM BD, MLCK calmodulin binding domain

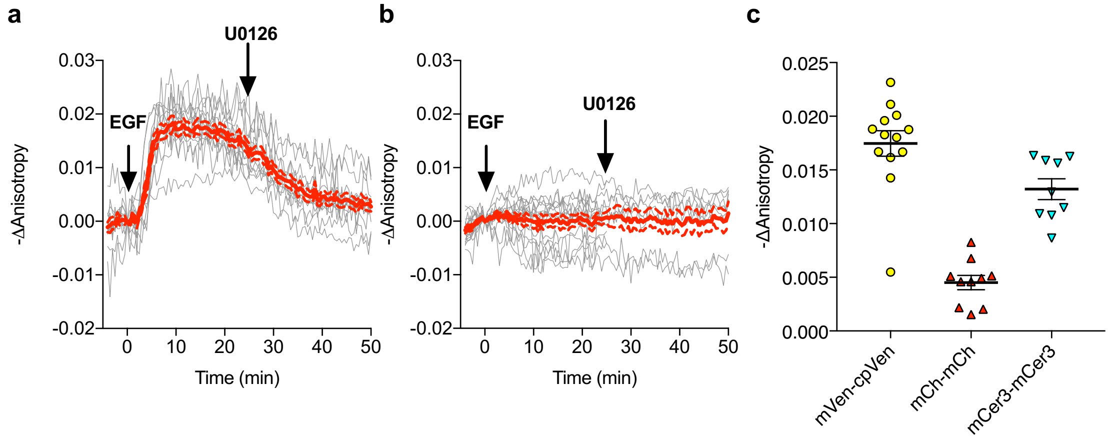

Figure 2.11 FLARE-EKAR Characterization

a). Individual (gray) and average (red) cell traces for Venus-cp172Venus FLARE EKAR (N=13), expressed in HEK293T cells and treated with 100 ng/mL epidermal growth factor (EGF) at t=0 min and the MEK inhibitor U0126 at t=25 min. b). Individual (gray) and average (red) cell traces for Venus-cp172Venus FLARE EKAR with a threonine-to-alanine (T-to-A) at the phosphorylation site (N=16), expressed in HEK293T cells and treated with 100 ng/mL epidermal growth factor (EGF) at t=0 min and the MEK inhibitor U0126 at t=25 min. c). A summary of anisotropy changes for various color-variants of FLARE-EKAR, upon stimulation with 100 ng/mL EGF. The magnitude of the signal was calculated by taking the mean anisotropy from t = 10min to t = 15 min and subtracting the mean anisotropy of the baseline before drug addition.

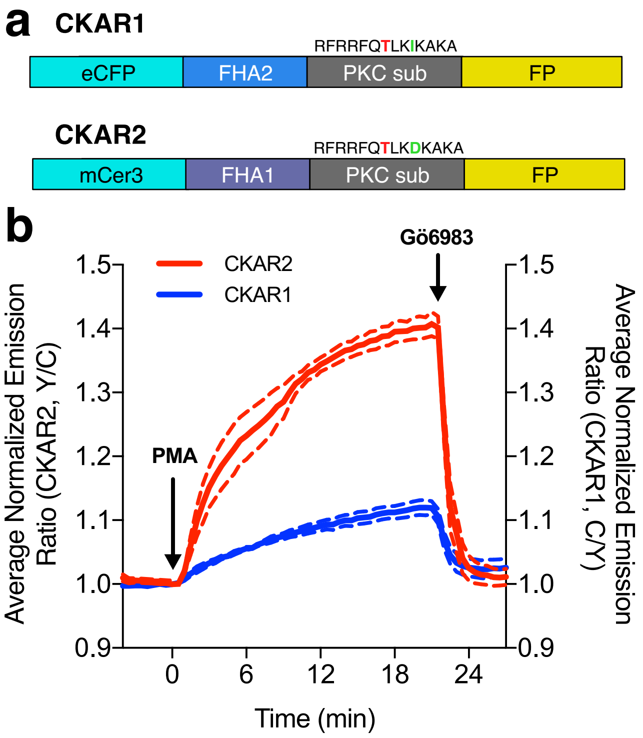

Figure 2.12 Characterization of the CKAR2 hetero-FRET sensor.

a). Comparison of CKAR1 and CKAR2 domain structures. b). Comparison of FRET responses of CKAR1 and CKAR2 expressed in HeLa cells to Protein Kinase C (PKC) stimulation with 50 ng/mL phorbol 12-myristate 13-acetate (PMA) as well as PKC inhibition with 1 µM Gö6983. Curves here represent mean curves from one representative experiment with biological replicates N=7 for CKAR1 and N=4 for CKAR2; the experiment was repeated three times.

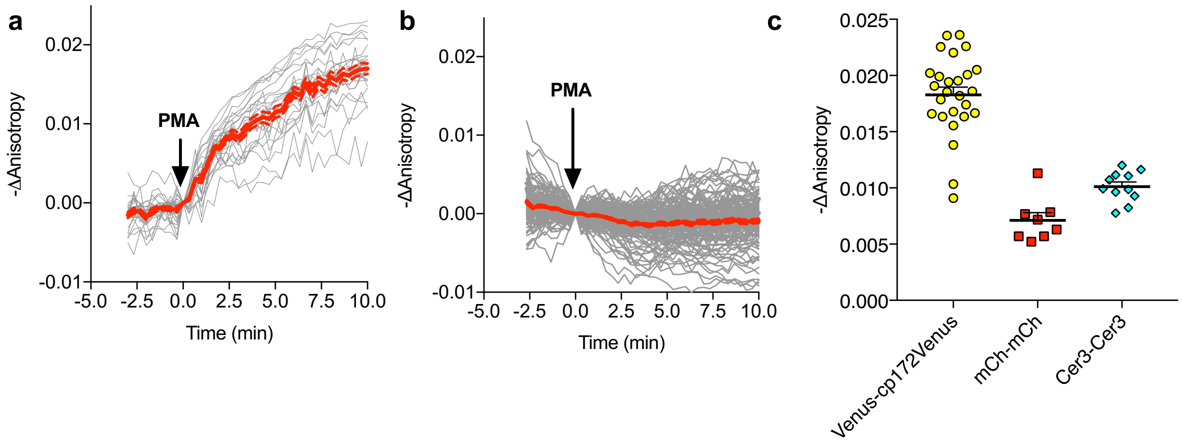

Figure 2.13 FLARE CKAR characterization.

a). Individual (gray) and average (red) cell traces for Venus-cp172Venus FLARE CKAR (N=26), expressed in HEK293-T cells treated with 50ng/mL PMA at t=0 min. Dotted lines above and below the curves reflect the standard error of the mean. b). Individual (gray) and average (red) cell traces for the kinase-inactive mutant of Venus-cp172Venus FLARE CKAR (TA mutant) (N=119), expressed in HEK293-T cells treated with 50ng/mL PMA at t=0 min. c). A summary of anisotropy changes for various color-variants of FLARE-ICUE in HEK293T cells upon stimulation with 50ng/mL PMA. The magnitude of the signal was calculated by taking the mean anisotropy from t = 10 min to t = 11.33 min and subtracting the mean anisotropy of the baseline before drug addition.

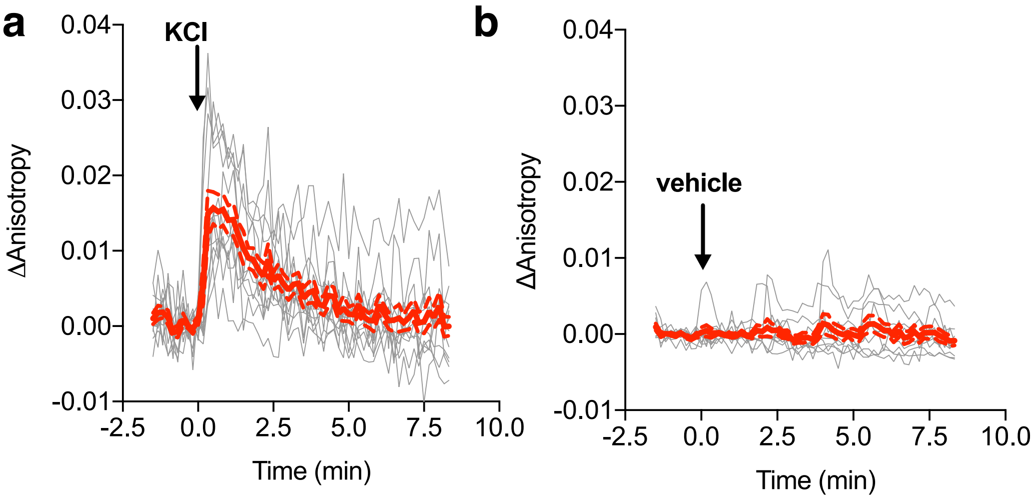

Figure 2.14 Characterization of FLARE MLCK

a). Individual (gray) and average (red) cell traces for FLARE-MLCK (N=13) with KCl added at t=0 min (N=13). b). Individual (gray) and average (red) cell traces for FLARE-MLCK with vehicle only added at t=0min (N=10). The dashed lines above and below the red curve reflect the standard error of the mean. The magnitude of the signal was calculated by taking the Δanisotropy at t = 0.33 min and subtracting the mean Δanisotropy of the baseline before drug addition.

Developing FLARE Second-Messenger Biosensors

In addition to biosensors for monitoring enzymes, we also developed FLAREs for monitoring second messenger dynamics (Figure 2.15a). We developed a Ca^{2+} FLARE by utilizing the sensor domain from the Cameleon family of biosensors, composed of CaM and the Ca^{2+}/CaM-binding peptide M13[8,16]. When expressed in HEK293T cells, Venus-cp172Venus FLARE-Cameleon exhibited a decrease in anisotropy of 0.03±0.002 (N=10) upon addition of 1 μM ionomycin and 5 mM $CaCl_2$, with the Venus-Venus, mCerulean3-mCerulean3, and mCherry-mCherry versions also showing detectable responses (Figure 2.15b, Figure 2.16a,b). The mVenus-based FLARE sensors tend to show larger dynamic ranges for a variety of FLARE sensors than mCerulean3 or mCherry variants, likely due to the superior extinction coefficient and quantum yield of mVenus, which make it a good FRET donor and acceptor. We further demonstrated the ability of Venus-cp172Venus FLARE Cameleon to detect submaximal responses by monitoring calcium transients in histamine-stimulated HeLa cells (Figure 2.16c). In order to determine the dissociation constant and Hill coefficients, we purified Venus-cp172Venus Cameleon and measured the fluorescence anisotropy in solutions of known free Ca^{2+} concentration at different temperatures (Figure 2.17). The resulting parameters are in good agreement with other Cameleon sensors[8]. Furthermore, we developed another calcium FLARE sensor, based on D1-ER[17], with a sensitivity appropriate for calcium monitoring in the ER. The anisotropy decreases upon increasing calcium concentration and increases when calcium is depleted from the ER upon treatment with thapsigargin (Figure 2.18). In addition to Ca^{2+}, we developed a FLARE to detect intracellular cAMP based on the ICUE family of sensors, in which a conformational change in the cAMP effector EPAC leads to a decrease in FRET efficiency in the presence of cAMP[18] (Figure 2.15a). When expressed in HEK293T cells, the fluorescence anisotropy of Venus-cp172Venus FLARE-ICUE increased by 0.02±0.001 (N=40) upon stimulation with Fsk/IBMX (Figure 2.15c, Figure 2.19).

Multiparameter Imaging with FLARE Biosensors

The fact that FLAREs only occupy a single color channel and are highly generalizable for different biosensors, as well as color variants, highlights their utility for multiplexed imaging applications. While multiplexing of hetero-FRET sensors is generally limited to two probes[19,20], we demonstrate that FLAREs can facilitate co-imaging of three biosensors simultaneously. We co-expressed mCherry-mCherry FLARE-AKAR, Venus-cpVenus FLARE-EKAR-EV, and mCerulean3-mCerulean3 FLARE-Cameleon in HEK293T cells and acquired a time-course with sequential treatment using Fsk/IBMX, EGF, and thapsigargin. Clear and distinct decreases in anisotropy were observed in the red channel after Fsk/IBMX treatment, in the yellow channel after EGF stimulation, and in the cyan channel after thapsigargin treatment, corresponding to an increase in PKA activity, Erk activity, and intracellular Ca^{2+}, respectively (N=17) (Figure 2.20, Figure 2.21).

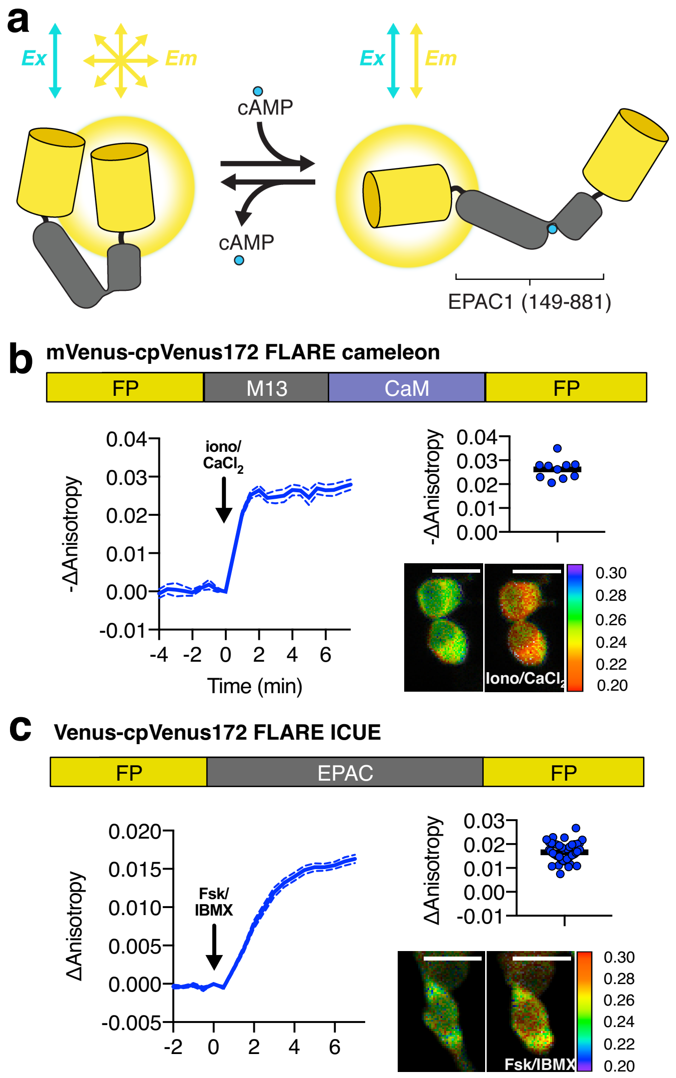

Figure 2.15 Design and characterization of FLARE second messenger sensors.

a). Schematic of FLARE ICUE cAMP second messenger sensor b). Domain structure of FLARE-Cameleon (top). Time-course of mean fluorescence anisotropy of Venus-cp172Venus FLARE-Cameleon (N=10) with addition of 1 μM ionomycin and 5 mM $CaCl_2$. Summary of

Figure 2.15 (continued) anisotropy changes after 1 μM ionomycin and 5 mM $CaCl_2$ (upper right) calculated as the difference between the mean anisotropy from t= 5min to t = 7.5 min and the anisotropy of the baseline before drug addition Representative anisotropy pseudocolor image before and after 1 μM ionomycin and 5 mM $CaCl_2$ addition. c). Domain structure of the cAMP sensor FLARE-ICUE (top). Time-course of mean fluorescence anisotropy of Venus-cp172Venus FLARE-ICUE (N=40) with addition of 50 μM forskolin and 100 μM IBMX at t=0 (left). Summary of anisotropy changes after 50 μM forskolin and 100 μM IBMX with respect to baseline (upper right), calculated as the difference between the mean anisotropy from t= 5min to t = 7.5 min and the anisotropy of the baseline before drug addition. Representative anisotropy pseudocolor image before (t=0 min) and after (t=7.5) stimulation with Fsk/IBMX (lower right). Dashed lines above and below time course reflect standard error of the mean.

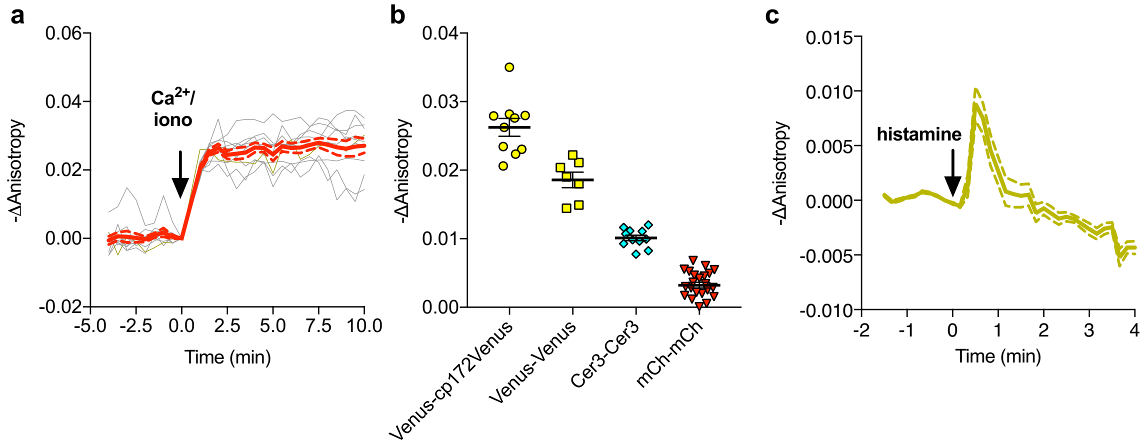

Figure 2.16 Characterization of FLARE Cameleon.

a). Individual (gray) and average (red) cell traces for Venus-cp172 FLARE Cameleon (N=10). b). A summary of anisotropy changes for various color-variants of FLARE-Cameleon in HEK293T cells upon stimulation with 1 μM ionomycin and 5mM calcium chloride. The mean for each is shown, with the error reflecting the standard error of the mean. The magnitude of the signal was calculated by taking the mean anisotropy from t = 5 min and t = 7.5 min and subtracting the mean anisotropy of the baseline before drug addition. c). Average anisotropy trace for Venus-cp172Venus FLARE-Cameleon expressed in HeLa cells upon stimulation with histamine (100 μM). Dotted lines above and below the curves reflect the standard error of the mean.

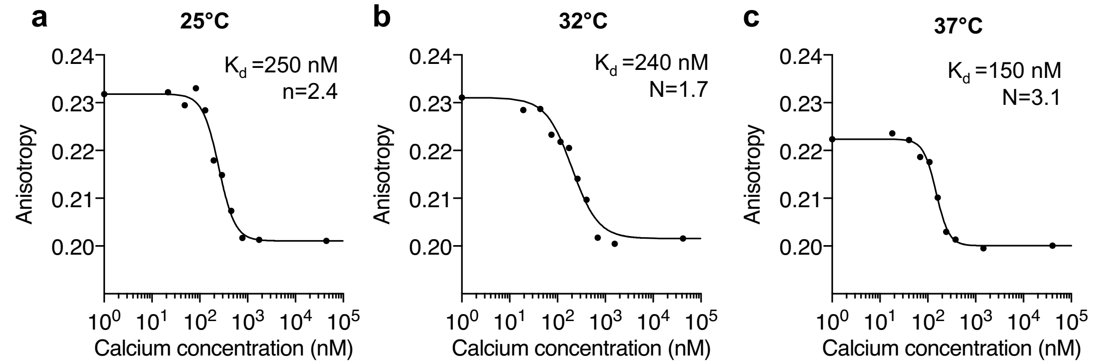

Figure 2.17 *In vitro* calibration of purified Venus-cp172 FLARE-Cameleon.

Anisotropy vs. calcium concentration calibration curves of purified Venus-cp172Venus Cameleon for a). 25°C b). 32°C, and c). 37°C.

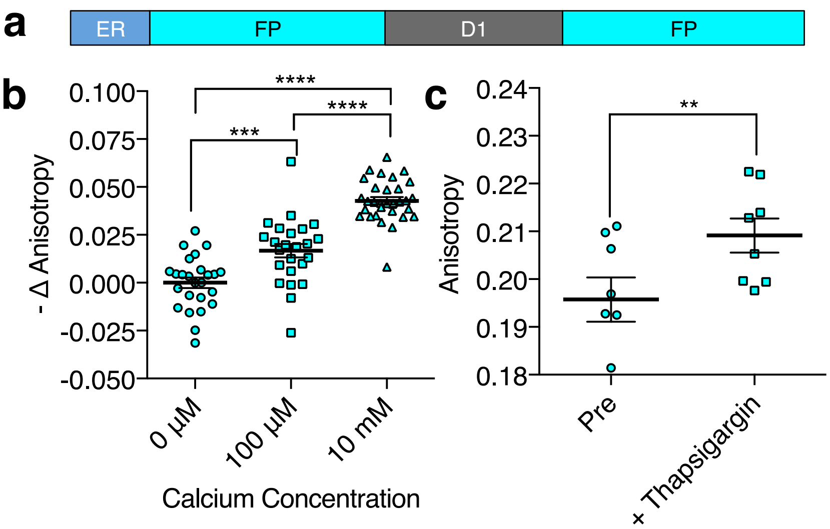

Figure 2.18 Characterization of CFP FLARE-D1ER

a). Schematic of the ER calcium sensor. b). REF52 cells expressing CFP FLARE D1ER were permeabilized using 5 μM ionomycin and equilibrated with 3 mM EGTA to remove Ca^{2+} or the indicated Ca^{2+} concentration. Fluorescence anisotropy values were normalized to the Ca^{2+} free condition. Statistical significance was assessed using an ANOVA and Tukey Multiple comparison test (*** $p < 0.001$, **** $p \leq 0.0001$). c) REF52 cells expressing CFP FLARE D1ER were treated with thapsigargin (1 uM, 5 min), to reduce ER Ca^{2+} levels (N=8, ** $p < 0.01$ by t-test). The mean for each of the above is shown, with the error reflecting the standard error of the mean

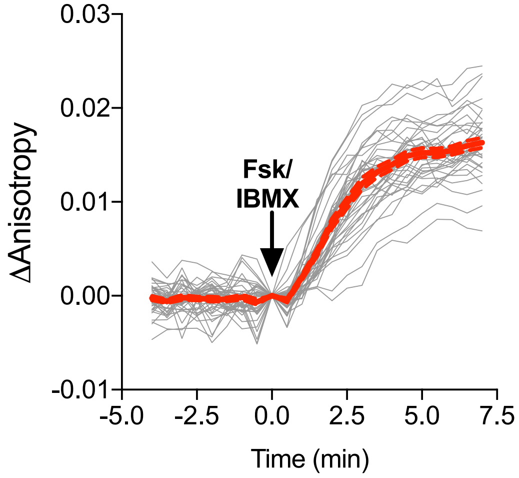

Figure 2.19 Individual Cell Traces for FLARE-ICUE

a). Individual (gray) and average (red) cell traces for Venus-cp172 FLARE-ICUE (N=40). Dashed lines above and below the average curve reflect the standard error of the mean.

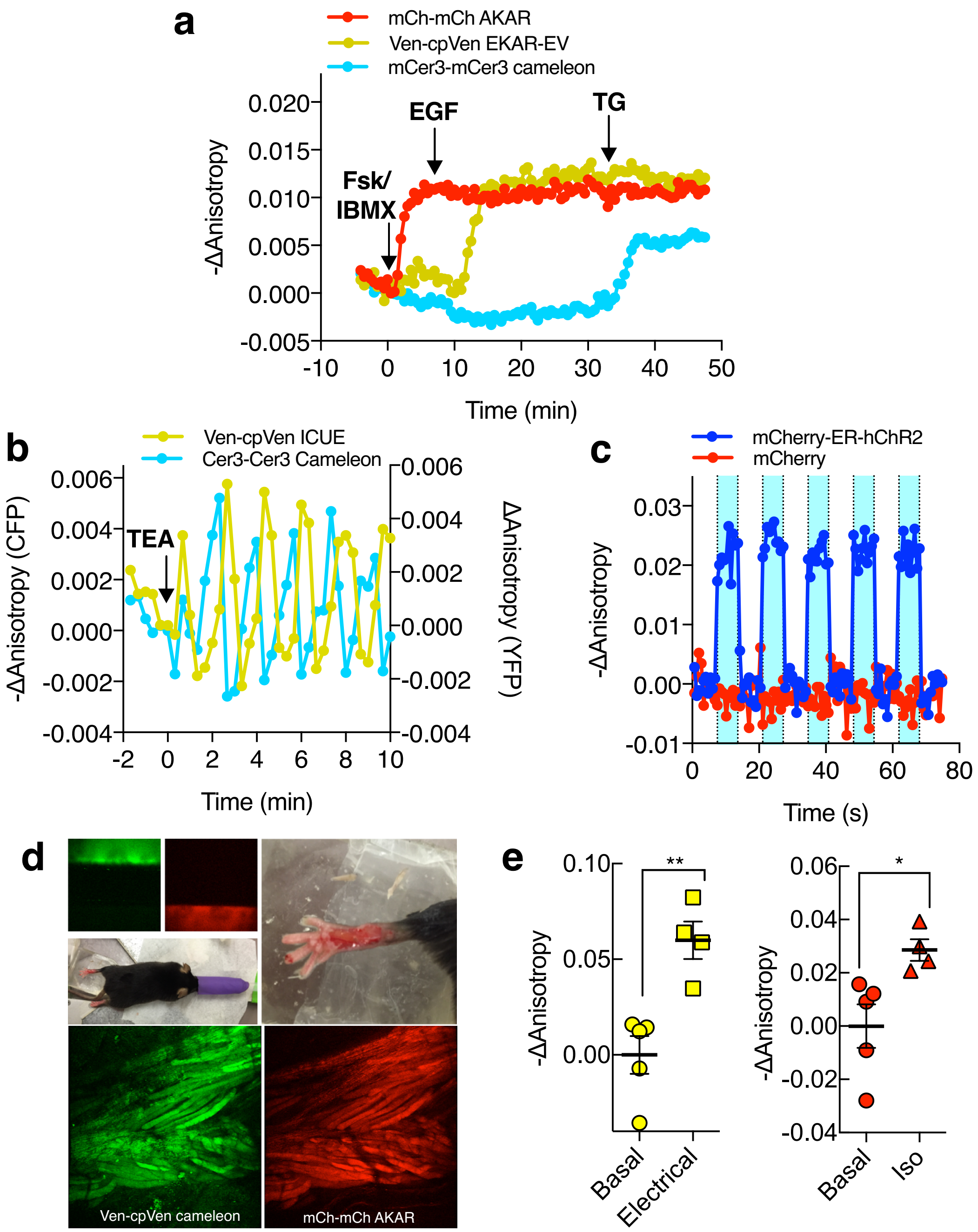

Figure 2.20 Multiparameter Imaging with FLAREs

a). Time-course of a representative HEK293T cell co-expressing mCherry-mCherry FLARE-AKAR, mVenus-cp172Venus FLARE-EKAR-EV, and mCerulean3-mCerulean3 FLARE-Cameleon, with 50 μM forskolin/100 μM IBMX added at t=0min, 100 ng/mL EGF at

Figure 2.20 (continued) t=7.5min, and 1 μM thapsigargin added at t=32.5min (N=17). b). Anisotropy response of a representative MIN6 cell co-expressing Cerulean3-Cerulean3 FLARE-Cameleon and Venus-cp172Venus FLARE-ICUE, showing robust oscillations after stimulation with TEA at t=0min (N=19). c). Venus-cp172Venus FLARE-Cameleon anisotropy time-course in REF52 cells co-expressing the sensor and either mCherry-tagged humanized channel rhodopsin2 (blue-curve) or mCherry alone (red-curve), with periodic illumination with 455nm light (indicated by cyan shading). d). Purified mVenus and mCherry proteins were placed in separate capillary tubes and imaged with 855 nm and 1200 nm two-photon excitation. Plasmids encoding Venus-cp172Venus FLARE-Cameleon and mCherry-mCherry FLARE-AKAR were electroporated into the skeletal muscle of the foot of a live mouse for *in vivo* imaging. Below are Z-stack projections of skeletal muscle co-expressing these two sensors, excited with 855 nm (left) and 1200 nm (right) light. e). Electrical stimulation decreased fluorescence anisotropy in the 855nm channel, consistent with increased cytoplasmic Ca^{2+} (left) (two-tailed T-test, p=0.0037). Intraperitoneal injection of isoproterenol activates mCherry-mCherry FLARE AKAR (two-tailed T-test, p=0.0239), as indicated by decreased anisotropy in the 1200nm channel (right). The mean for each is shown, with the error reflecting the standard error of the mean.

Figure 2.21 Average and Individual Traces for Three-Color FLARE Imaging

a). Average cell traces for mCherry-mCherry FLARE-AKAR, Venus-cp172Venus FLARE-EKAR, and mCer3-mCer3 FLARE Cameleon, expressed in HEK293T cells, and stimulated with 50 μM forskolin and 100 μM IBMX at t=0min, 100 ng/mL EGF at t=7.5 min, and 1 μM thapsigargin at t=32.5min. (Dashed lines reflect the standard error of the mean). b). Single cell anisotropy traces for above experiment.

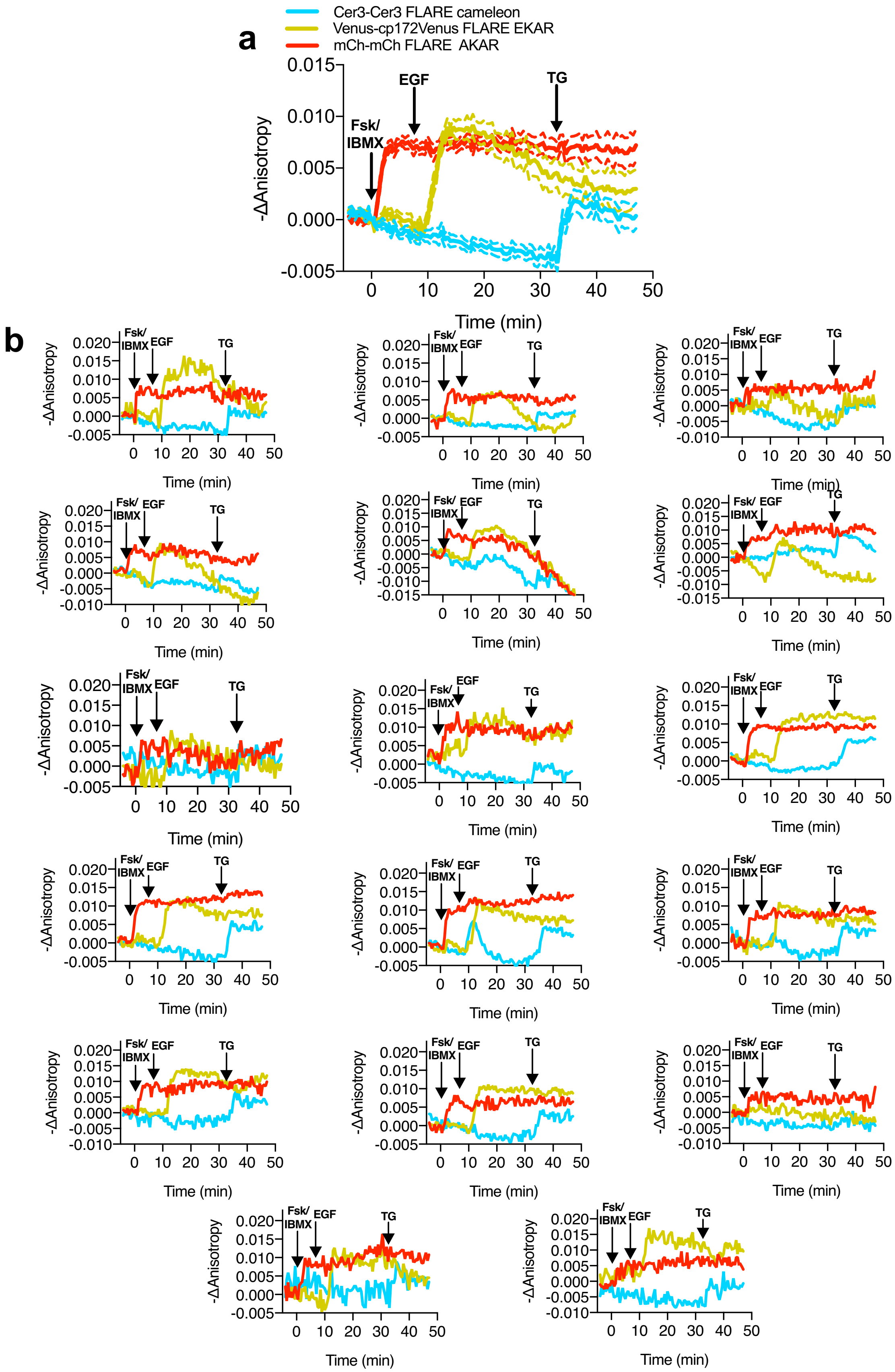
a
Cer3-Cer3 FLARE cameleon
Venus-cp172Venus FLARE EKAR
mCh-mCh FLARE AKAR
Fsk/
IBMX
EGF
TG
-ΔAnisotropy
0.015
0.010
0.005
0.000
-0.005
0
10
20
30
40
50
Time (min)
b
Fsk/
IBMX
EGF
TG
-ΔAnisotropy
Time (min)

We further aimed to show that FLARE sensors can be used to monitor multiple signaling activities simultaneously in different cellular contexts. For example, mCer3-mCer3 FLARE Cameleon, co-imaged with other FLARE sensors in HeLa cells, can detect calcium responses to physiologically relevant stimulation conditions, such as histamine (Figure 2.22). Additionally, when mCer3-mCer3 FLARE AKAR was co-imaged with Venus-cp172Venus cameleon in HEK293-T cells, activation of the β-adrenergic with isoproterenol led to a transient decrease in anisotropy in the cyan-channel (Figure 2.23). Furthermore, we used FLAREs to study the cAMP-Ca^{2+} oscillatory circuit in pancreatic β-cells. MIN6 β-cells were transiently transfected with Venus-cp172Venus FLARE-ICUE and mCerulean3-mCerulean3 FLARE-Cameleon to simultaneously monitor cAMP and Ca^{2+} dynamics, respectively (N=19). We observed clear fluorescence anisotropy oscillations in both channels following stimulation with 20 mM tetraethylammonium chloride (TEA) (Figure 2.20b, 2.24). Ca^{2+} and cAMP exhibit synchronized oscillations, with Ca^{2+} increases corresponding to cAMP decreases, consistent with previous findings[21,22]. These data demonstrate that even the lower-signal mCerulean3-based FLARE sensors can be used under sub-maximal and physiologically relevant stimulation conditions in multiplexed imaging experiments.

Figure 2.22 Multiparameter FLARE imaging of PKA, Erk and calcium, with histamine-induced calcium stimulation

Average cell traces for mCherry-mCherry FLARE-AKAR, Venus-cp172Venus FLARE-EKAR, and mCer3-mCer3 FLARE Cameleon, expressed in HeLa cells, and stimulated with 50 μM forskolin and 100 μM IBMX at t=0min, 100 ng/mL EGF at t=7.5 min, and 100 μM histamine at t=32.5min (N=11). (Dashed lines reflect the standard error of the mean). In the cyan channel, transient decreases in anisotropy can be observed both after both EGF and histamine stimulation. b). Representative cell anisotropy traces for above experiment.

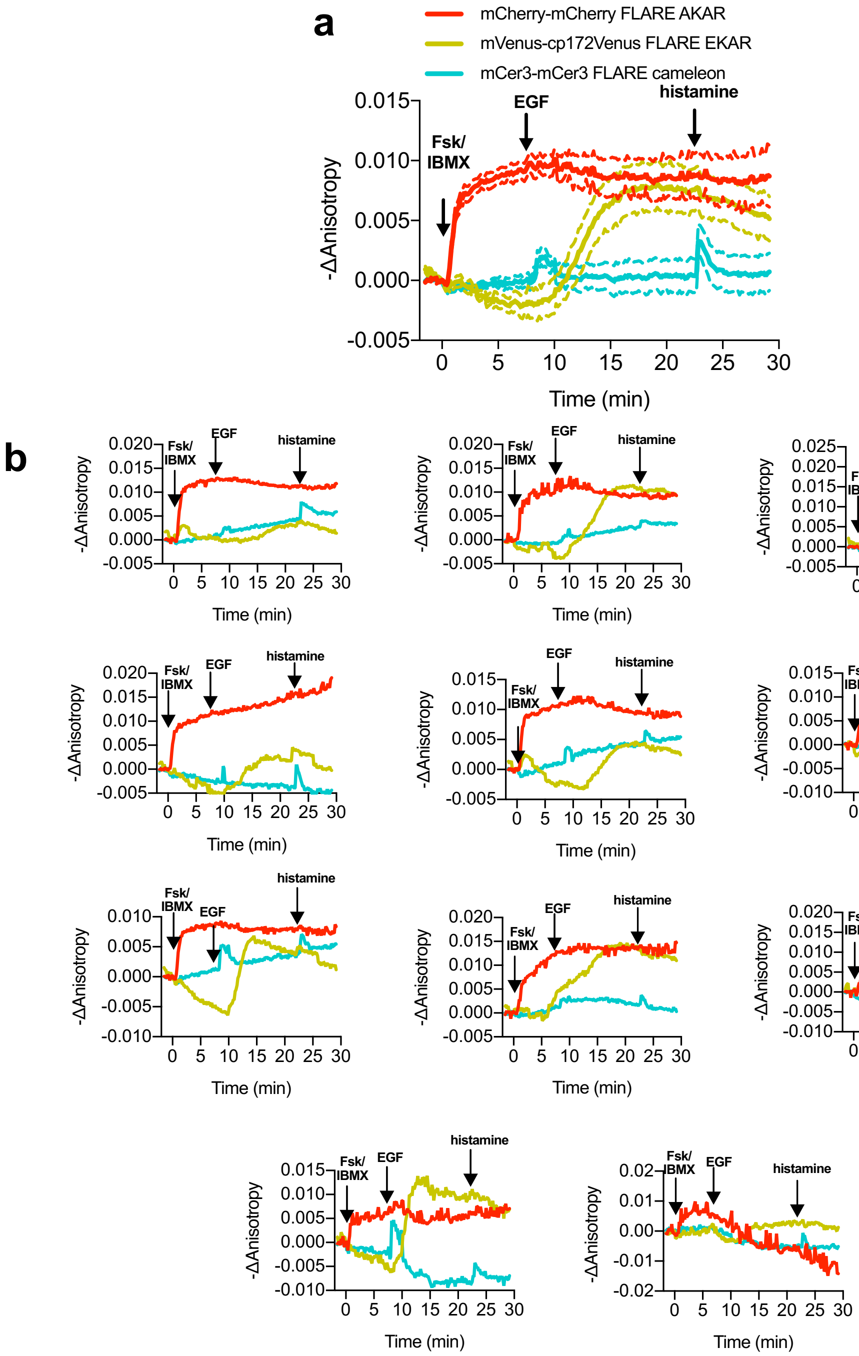
a
mCherry-mCherry FLARE AKAR
mVenus-cp172Venus FLARE EKAR
mCer3-mCer3 FLARE cameleon
Fsk/ IBMX
EGF
histamine
-ΔAnisotropy
0.015
0.010
0.005
0.000
-0.005
0
5
10
15
20
25
30
Time (min)
b
Fsk/ IBMX
EGF
histamine
-ΔAnisotropy
Time (min)

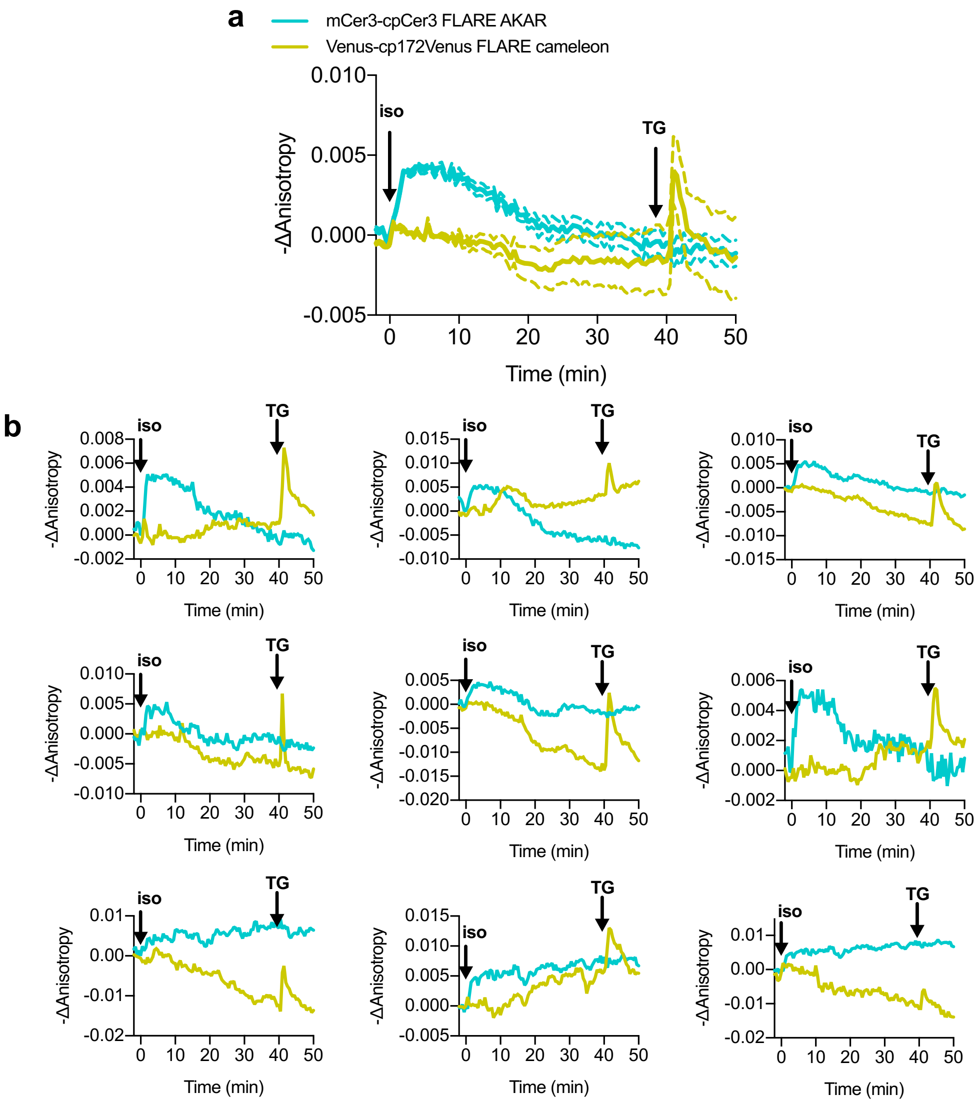

Figure 2.23 Two-color FLARE Imaging of PKA and Calcium with Isoproterenol Stimulation of PKA

a). Average cell traces for mCerulean3-mCerulean3 FLARE-AKAR, and mVenus-cp172Venus FLARE Cameleon, expressed in HEK293-T cells, and stimulated with 100 nM isoproterenol at t=0min and 1 µM thapsigargin at t=40 min (N=28). (Dashed lines reflect the standard error of the mean). b). Representative cell anisotropy traces for above experiment.

Figure 2.24 Monitoring calcium and cAMP oscillations in pancreatic beta cells.

Additional cell traces for mCer3-mCer3 FLARE-Cameleon and Venus-cp172Venus ICUE, coexpressed in Min6 cells, showing out of phase oscillations upon stimulation with TEA (N=19).

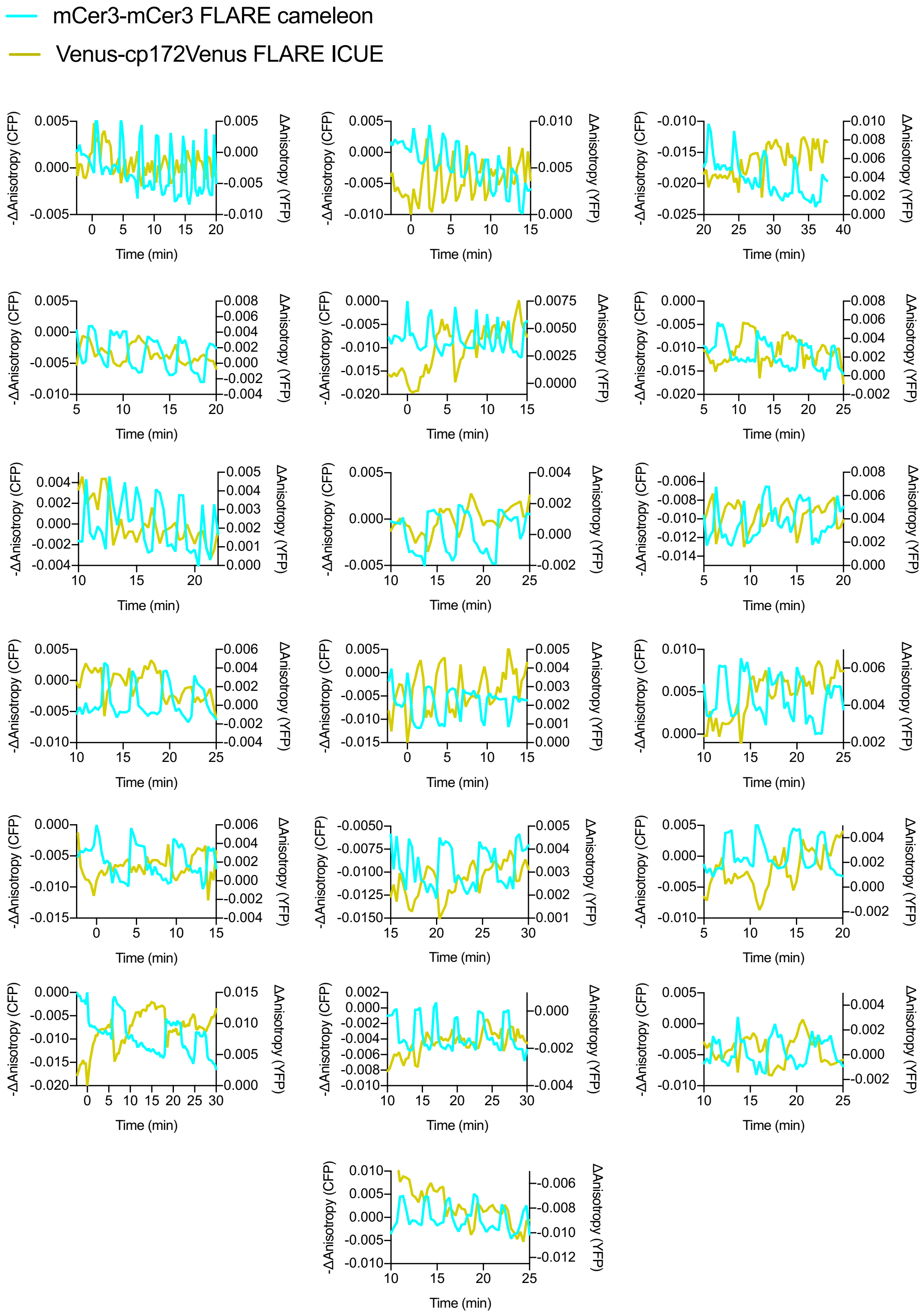
mCer3-mCer3 FLARE cameleon
Venus-cp172Venus FLARE ICUE
-ΔAnisotropy (CFP)
ΔAnisotropy (YFP)
Time (min)

In addition to multiplexed biosensor imaging, the fact that FLARE sensors occupy only a single color channel also permits simultaneously perturbing and monitoring biochemical activities using optogenetics and FLAREs, respectively. We coexpressed an mCherry-tagged, ER-targeted channelrhodopsin2 (hChR2)[23,24,25], a light-gated calcium ion channel, with Venus-cp172 FLARE-Cameleon in REF52 cells, a rat embryonic fibroblast cell line. Illumination with blue light produced an immediate decrease in anisotropy, corresponding to an increase in intracellular Ca^{2+} (Figure 2.20c, Figure 2.25). Control cells lacking hChR2 expression showed no change in anisotropy in the yellow channel.

In vivo, two-photon imaging of FLAREs was tested using a skeletal muscle preparation (Figure 2.20d,e). Exclusive excitation of mVenus (855 nm) or mCherry 1200 nm) was verified by imaging capillary tubes filled with recombinant proteins (Figure 2.20d). Plasmids encoding Venus-cp172Venus FLARE-Cameleon and mCherry FLARE-AKAR sensors were electroporated into the flexor digitorum brevis muscle of a live mouse[26, 27]. Administration of an electrical current stimulated a rise in intracellular Ca^{2+} concentration, as indicated by a decrease in FLARE-Cameleon anisotropy, independent of changes in FLARE-AKAR anisotropy (Figure 4e). Activation of AKAR was then induced by intraperitoneal injection of isoproterenol (0.5 mg/kg). Thus, FLAREs enable *in vivo* multiparametric biosensor measurements.

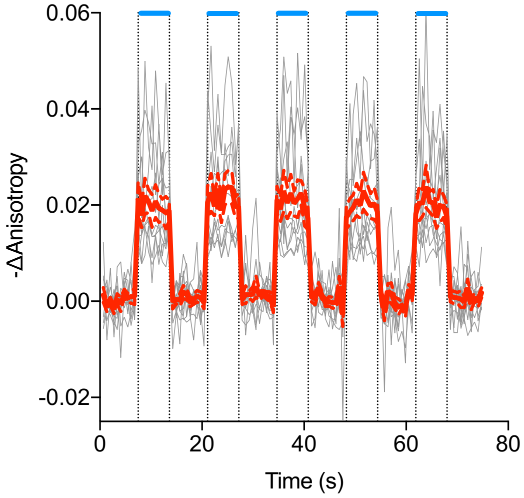

Figure 2.25 Individual and Average Cell Traces of FLARE AKAR Coexpressed with hChR2-ER

Individual (gray) and average (red) cell traces for Venus-cp172Venus FLARE AKAR co-expressed with hChR2-ER, with intermittent exposures to 455nm light (N=11). Dashed lines reflect the standard error of the mean.

We have demonstrated that FLAREs are a highly generalizable, accessible platform for creating single-color sensors to detect biochemical activities in individual cells in real time. Their ratiometric readout allows for fluctuations in light intensity and probe concentration to be cancelled out, permitting quantitative measurements of intracellular concentrations. We showed that these sensors have an SNR of 3-32 (Table 2.1) and a dynamic range comparable with first-generation FRET sensors[28,29]. Future development and optimization should further enhance their performance. We demonstrated that current FLAREs are already useful for multiplexed imaging applications. They can also be used in conjunction with optogenetic tools to enable all-optical interrogation of cellular regulation, and for intravital two-photon imaging to facilitate studies in tissues and living animals. FLAREs, by allowing researchers to monitor multiple activities within the same cell, as well as to both monitor and optogenetically perturb activities in the same cell, could be used to study the how the spatiotemporal regulation of biochemical activities in highly integrated pathways allows a small number of signals to produce diverse cellular behaviors.

Sensor	Signal to Noise Ratio (± SEM)
Venus-cp172Venus FLARE AKAR	32 ± 2.0 (N=32)
mVenus-mVenus FLARE AKAR	10 ± 1.6 (N=32)
EGFP-EGFP FLARE AKAR	6 ± 0.6 (N=32)
mCherry-mCherry FLARE AKAR	14 ± 1.5 (N=22)
mCerulean3-mCerulean3 FLARE AKAR	3 ± 0.5 (N=10)
mCerulean3-cp173 Cerulean3 FLARE AKAR	5 ± 0.3 (N=26)
Venus-cp172Venus FLARE EKAR	17 ± 3.1 (N=8)
mCherry-mCherry FLARE EKAR	4 ± 0.8 (N=10)
mCerulean3-mCerulean3 FLARE EKAR	9±2.3 (N=9)
Venus-cp172Venus FLARE CKAR	27 ± 3.3 (N=26)
mCherry-mCherry FLARE CKAR	14 ± 3.0 (N=8)
mCerulean3-mCerulean3 FLARE CKAR	9 ± 1.7 (N=6)
FLARE-MLCK	8 ± 0.8 (N=13)
Venus-cp172Venus FLARE Cameleon	19 ± 4.8 (N=10)
mCherry-mCherry FLARE Cameleon	5 ± 0.8 (N=23)
mCerulean3-mCerulean3 FLARE Cameleon	9 ± 1.5 (N=11)
Venus-cp172 Venus FLARE ICUE	19 ± 1.2 (N=40)

Table 2.1 Signal-to-noise ratios of FLARE sensors

Materials and Methods

Plasmid and Construct Construction

Cloning was performed using the pRSET-B vector using typical molecular cloning methods using polymerase chain reaction (PCR) with Phusion polymerase (New England Biolabs), restriction enzyme digestion, and ligation with T4 DNA ligase. To clone Venus-cp172Venus FLARE, AKAR4 was sub-cloned from a modified pCDNA3 to pRSET-B between the BamHI and EcoRI restriction enzyme sites. mVenus was then PCR amplified with primers encoding a BamHI site at the 5’ end and an SphI site at the 3’ end, and the resulting PCR product was digested with BamHI and SphI and ligated to pRSET-B AKAR4 digested with BamHI and SphI, with the mCerulean1 gene removed. Venus-cp172Venus FLARE AKAR was then sub-cloned back into a modified pCDNA3 vector using the BamHI and EcoRI sites. Other color variants were created by replacing the genes for the fluorescent proteins in other FLARE AKAR variants in pRSET-B, either between the BamHI and SphI sites for the N-terminal fluorescent protein, or SacI and EcoRI for C-terminal fluorescent proteins. Finalized constructs intended for mammalian expression were then sub-cloned into a modified pcDNA3 expression vector between the BamHI and EcoRI sites. FLARE variants of other sensors were created by amplifying the molecular switch from EKAR-EV, CKAR2, Cameleon and ICUE3 with primers encoding the SphI and SacI sites, digesting the PCR product with SphI and SacI enzymes, and ligating them to the relevant pRSET-B FLARE AKAR plasmid digested with SphI and SacI to remove the domains involved in the molecular switch for FLARE AKAR. The final constructs were then subcloned into a modified pCDNA3 expression vector between the BamHI and EcoRI sites. Targeted versions of the sensors were created either by PCR amplifying the sensor with primers containing the targeting sequence and ligating it to the pCDNA3 expression vector between BamHI and EcoRI, or by subcloning the construct into a plasmid already containing the targeting sequence. N-terminal targeting sequences were placed between HindIII and EcoRI, and C-terminal targeting sequences between EcoRI and XbaI. All cloning steps were performed using DH5α strain of *E. coli.*

The threonine to alanine mutants for Venus-cp172Venus FLARE AKAR and FLARE EKAR were created by performing site-directed mutagenesis using a standard single-primer PCR-based protocol. The threonine to alanine mutant for Venus-cp172Venus FLARE CKAR, as well as the chromophore-dead variant of Venus-cp172Venus FLARE AKAR, was created using Gibson assembly, amplifying the appropriate fragment with a primer containing the desired mutation.

The YFP MLCK FLARE sensor was created by replacing the CFP portion of an existing two color sensor[15,30] with a PCR amplified mVenus fragment flanked by XhoI and AgeI restriction sites. Moreover, the coding sequence for the CFP D1 ER sequence was manufactured by Genewiz. The sensor consists of two oxmCer3 proteins (https://www.ncbi.nlm.nih.gov/pubmed/26158227) flanking the D1 ER calcium sensing domains[17] and a C-terminal KDEL ER retention sequence.

Cell Culture and Transfection

HEK293-T and HeLa cells cells were maintained using Dulbecco's Modified Eagle's Medium (DMEM) supplemented with 10% fetal bovine serum (FBS) and 1% penicillin/streptomycin. Cells were seeded onto a 35-mm glass-bottom imaging dish and incubated at 37°C with 5% ambient carbon dioxide. HEK293-T, HeLa, Min6, and REF-52 cell lines were maintained separately from other cells and were screened regularly to confirm the absence of mycoplasma contamination using Hoechst staining. As the origin of the cells was not central to the nature of these experiments, we did not further validate the identity of the cell lines. Cells were transfected using Lipofectamine 2000 (Invitrogen), Polyjet (SignaGen), or calcium phosphate and incubated for 12-48 hours before imaging. The growth media was removed immediately before imaging, and the cells were washed two or more times with Hanks Balanced Salt Solution (HBSS) buffer with glucose at room temperature. The cells were imaged in HBSS buffer with glucose at either room temperature or 37°C.

Fluorescence Polarization Microscopy

Widefield images were collected using an Zeiss AxioObserver equipped for fluorescence polarization microscopy, using one of two setups. In the first setup, a wire grid polarizer (Meadowlark Optics) was placed in the excitation pathway between the LED illuminators and reflector turret containing filter cubes specific for CFP (Zeiss), YFP (Zeiss), and mCherry (Semrock). Images were generally collected using a 20× 0.75 NA objective lens. Polarizations parallel and perpendicular to the excitation polarizations were separated using Optical Insights Dual-View using their polarization splitting module. Both images were simultaneously collected in a single image collected by a water-cooled Orca-R2 (Hamamatsu). In the second setup, a polarizer (Chroma) was placed in the excitation pathway between the xenon arclamp and the excitation filters. Images were collected using a 20× 0.45 NA objective lens. Polarizations were separated using an

Opto-Split II LS image splitter, with two wire grid polarizers (Meadowlark) oriented parallel and perpendicular to the excitation polarizer. Images of both polarizations were collected using a Hamamatsu Flash 4.0 sCMOS camera. Two-photon imaging was performed using a Zeiss 7 MP with GaAsP non-descanned detectors housed at the University of Maryland School of Medicine confocal facility. Coherent Chameleon and OPO lasers were used for excitation. Fluorescence was filtered using an ET680 short pass filter for two-photon microscopy (Chroma) prior to separating polarizations with a 1 inch broadband polarizing beamsplitter cube (Thorlabs) mounted using a custom 3D printed cube. Images were collected using a 10×, 0.3 NA Plan-apochromat objective lens. *In vivo* imaging was performed on C57Bl/6 mice under isoflurane anesthesia.

Image Analysis

Image analysis was performed using Fiji (ImageJ) open-source image processing software. Polarization images were cropped and aligned using either the Zeiss Axiovision software or Fiji's built-in StackReg registration plugin. In Fiji, regions of interest (ROIs) were drawn around each cell, as well as one in the background. ROI intensities were background subtracted in each channel to estimate fluorescence emission intensity, and anisotropy was calculated as described by Lakowicz *et al*[31].. Anisotropies were calculated using the conventional equation[30]:

$$r = \frac{P - gS}{P + 2gS}$$

(Where g is the correction factor that accounts for differences in polarization transmission efficiencies within the instrument. The g-factor was calculated using an isotropic fluorescein solution as described by Piston *et al.*[32] Δanisotropy was calculated by subtracting the anisotropy at each time point by the anisotropy at the time point right before drug addition. The magnitude of the anisotropy changes were calculated by taking the difference between the average anisotropy when the signal peaked or plateaued and the average anisotropy of the baseline time points before drug was added.

Protein Purification

Purification of the FLARE-Cameleon sensors was done using the BL21-RIL Codon Plus strain of *E. coli*, which were transformed with the construct cloned in the pRSET-B vector, with a Poly-His tag in the header sequence to allow for metal ion binding. The cells were grown to an OD of 0.2, when expression was induced with IPTG and allowed to grow overnight. The cells were then pelleted, frozen, resuspended, and lysed by sonication. Protein purification was performed using column chromatography with Ni-NTA resin. Fractions were collected and analyzed using SDS-PAGE; fractions showing sufficiently pure protein product were pooled.

In vitro *Calcium Calibration*

In vitro calibration of the FLARE-Cameleon sensor was performed using fluorescence anisotropy spectroscopy in solutions with varying concentrations of free calcium in a temperature-controlled environment. These solutions were made by titrating known concentrations of free EGTA and calcium-saturated EGTA at pH 7.1 (Calcium Concentration Kit #1--Thermo Scientific). The fluorescence anisotropy was measured using a Photon Technology International QuantaMaster spectrofluorometer equipped with a Xenon flash lamp, fluorescence polarizers, and a Peltier cuvette holder for temperature control. Anisotropies were calculated using integrated intensities of S- and P-polarized emission spectra. The correction factor G was measured by measuring the P- and S-polarized emission spectra of fluorescein, which is assumed to be isotropic, and taking the ratio of their measured integrated fluorescence intensities. To determine the dissociation constant (K_d) and Hill coefficient (n), the anisotropy vs. calcium concentration data were fit to the following equation:

$$r = r_{min} + (r_{max} - r_{min}) * (\frac{[Ca^{2+}]}{K_d + [Ca^{2+}]})^n$$

Personal Contributions

I conceived of the FLARE sensor design of applying the anisotropy-based homo-FRET principle to enzymatic activity and second messenger sensors. I also performed the cloning and anisotropy imaging for all the FLARE AKAR, EKAR, and Cameleon variants as well as the subsequent co-imaging and control experiments. I also performed the image analysis and was responsible for the visualization of the data. Furthermore, I involved with the set up of the anisotropy imaging setup in the Zhang lab. I worked with B. Tenner on the cloning and imaging of the FLARE ICUE, and CKAR variants, as well as the co-imaging experiments in Min6 cells. I finally was responsible for the writing and compiling of the manuscript and the creation of the figures.

References

1. Bader, A. N. *et al.* Homo-FRET imaging as a tool to quantify protein and lipid clustering. *Chemphyschem* 12, 475–83 (2011).
2. Bader, A. N., Hofman, E. G., Voortman, J., en Henegouwen, P. M. P. van B. & Gerritsen, H. C. Homo-FRET imaging enables quantification of protein cluster sizes with subcellular resolution. *Biophys. J.* 97, 2613–22 (2009).
3. Gautier, I. *et al.* Homo-FRET microscopy in living cells to measure monomer-dimer transition of GFP-tagged proteins. *Biophys. J.* 80, 3000–8 (2001).
4. Warren, S. C., Margineanu, A., Katan, M., Dunsby, C. & French, P. M. W. Homo-FRET Based Biosensors and Their Application to Multiplexed Imaging of Signalling Events in Live Cells. *Int. J. Mol. Sci.* 16, 14695–716 (2015).
5. Cameron, W. D. *et al.* Apollo-NADP(+): a spectrally tunable family of genetically encoded sensors for NADP(+). *Nat. Methods* 13, 352–8 (2016).
6. Zhang, J., Ma, Y., Taylor, S. S. & Tsien, R. Y. Genetically encoded reporters of protein kinase A activity reveal impact of substrate tethering. *Proc. Natl. Acad. Sci. U. S. A.* 98, 14997–5002 (2001).
7. Depry, C., Allen, M. D. & Zhang, J. Visualization of PKA activity in plasma membrane microdomains. *Mol. Biosyst.* 7, 52–8 (2011).
8. Nagai, T., Yamada, S., Tominaga, T., Ichikawa, M. & Miyawaki, A. Expanded dynamic range of fluorescent indicators for Ca(2+) by circularly permuted yellow fluorescent proteins. *Proc. Natl. Acad. Sci. U. S. A.* 101, 10554–9 (2004).
9. DiPilato, L. M. & Zhang, J. The role of membrane microdomains in shaping beta2-adrenergic receptor-mediated cAMP dynamics. *Mol. Biosyst.* 5, 832–7 (2009).

10. Allen, M. D. & Zhang, J. Subcellular dynamics of protein kinase A activity visualized by FRET-based reporters. *Biochem. Biophys. Res. Commun.* 348, 716–21 (2006).
11. Markwardt, M. L. *et al.* An improved cerulean fluorescent protein with enhanced brightness and reduced reversible photoswitching. *PLoS One* 6, e17896 (2011).
12. Harvey, C. D. *et al.* A genetically encoded fluorescent sensor of ERK activity. *Proc. Natl. Acad. Sci. U. S. A.* 105, 19264–9 (2008).
13. Vandame, P. *et al.* Optimization of ERK activity biosensors for both ratiometric and lifetime FRET measurements. *Sensors (Basel).* 14, 1140–54 (2014).
14. Herbst, K. J., Allen, M. D. & Zhang, J. Luminescent kinase activity biosensors based on a versatile bimolecular switch. *J. Am. Chem. Soc.* 133, 5676–9 (2011).
15. Isotani, E. et al. Real-time evaluation of myosin light chain kinase activation in smooth muscle tissues from a transgenic calmodulin-biosensor mouse. Proc. Natl. Acad. Sci. U. S. A. 101, 6279–6284 (2004).
16. Miyawaki, A., Griesbeck, O., Heim, R. & Tsien, R. Y. Dynamic and quantitative Ca2+ measurements using improved cameleons. *Proc. Natl. Acad. Sci. U. S. A.* 96, 2135–40 (1999).
17. Palmer, A. E., Jin, C., Reed, J. C. & Tsien, R. Y. Bcl-2-mediated alterations in endoplasmic reticulum Ca2+ analyzed with an improved genetically encoded fluorescent sensor. *Proc. Natl. Acad. Sci. U. S. A.* 101, 17404–9 (2004).
18. DiPilato, L. M. & Zhang, J. The role of membrane microdomains in shaping beta2-adrenergic receptor-mediated cAMP dynamics. *Mol. Biosyst.* 5, 832–7 (2009).

19. Depry, C., Mehta, S. & Zhang, J. Multiplexed visualization of dynamic signaling networks using genetically encoded fluorescent protein-based biosensors. *Pflugers Arch.* 465, 373–81 (2013).
20. Shcherbakova, D. M., Hink, M. A., Joosen, L., Gadella, T. W. J. & Verkhusha, V. V. An orange fluorescent protein with a large Stokes shift for single-excitation multicolor FCCS and FRET imaging. *J. Am. Chem. Soc.* 134, 7913–23 (2012).
21. Landa, L. R. *et al.* Interplay of Ca2+ and cAMP signaling in the insulin-secreting MIN6 beta-cell line. *J. Biol. Chem.* 280, 31294–302 (2005).
22. Ni, Q. *et al.* Signaling diversity of PKA achieved via a Ca2+-cAMP-PKA oscillatory circuit. *Nat. Chem. Biol.* 7, 34–40 (2011).
23. Nagel, G. *et al.* Channelrhodopsin-2, a directly light-gated cation-selective membrane channel. *Proc. Natl. Acad. Sci. U. S. A.* 100, 13940–5 (2003).
24. Lin, J. Y., Lin, M. Z., Steinbach, P. & Tsien, R. Y. Characterization of engineered channelrhodopsin variants with improved properties and kinetics. *Biophys. J.* 96, 1803–14 (2009).
25. Markwardt, M. L., Seckinger, K. M. & Rizzo, M. A. Regulation of Glucokinase by Intracellular Calcium Levels in Pancreatic β Cells. *J. Biol. Chem.* 291, 3000–9 (2016).
26. DiFranco, M., Quinonez, M., Capote, J. & Vergara, J. DNA transfection of mammalian skeletal muscles using in vivo electroporation. J. Vis. Exp. (2009). doi:10.3791/1520
27. Kerr, J. P. *et al.* Detyrosinated microtubules modulate mechanotransduction in heart and skeletal muscle. *Nat. Commun.* 6, 8526 (2015).

28. Newman RH, Zhang J. Visualization of phosphatase activity in living cells with a FRET-based calcineurin activity sensor. *Mol Biosyst* 4(6), 496-501 (2008).

29. Zhou, Xin *et al.* Dynamic Visualization of mTORC1 Activity in Living Cells. *Cell Reports*. 10(10), 1767 – 1777

30. Gebuchadze, R; Zhi G, Lau KS, Isotani E, Persechini A, Kamm KE, S. J. No Title. *FEBS Lett.* 16, 121–124 (2004).

31. Lakowicz, Joseph R. *Principles Of Fluorescence Spectroscopy*. 1st ed. New York: Springer, 2010. Print.

32. Piston, D. W. & Rizzo, M. A. FRET by fluorescence polarization microscopy. *Methods Cell Biol.* 85, 415–30 (2008).

Chapter 3 Genetically encoded biosensors for visualizing live-cell biochemical activity at super-resolution.

A version of this chapter has been published, and appears in:

G. C. H Mo, **B. Ross**, F. Hertel, P. Manna, X. Yang, E. C. Greenwald, C. Booth, A. M. Plummer, B. Tenner, Z. Chen, Y. Wang, E. J. Kennedy, P. A. Cole, K. G. Fleming, A. Palmer, R. Jimenez, J. Xiao, P. Dedecker, and J. Zhang, "Genetically-Encoded Biosensors for Visualizing Live-cell Biochemical Activity at Superresolution", *Nature Methods*, 14: 427-434 (2017).

Abstract

Compartmentalized biochemical activities are essential to all cellular processes, but there is no generalizable method to visualize dynamic protein activities in living cells at a resolution commensurate with their compartmentalization. Here we introduce a new class of fluorescent biosensors that detect biochemical activities in living cells at a resolution up to three-fold better than the diffraction limit. Utilizing specific, binding-induced changes in protein fluorescence dynamics, these biosensors translate kinase activities or protein-protein interactions into changes in fluorescence fluctuations, which are quantifiable through stochastic optical fluctuation imaging. A Protein Kinase A (PKA) biosensor allowed us to resolve minute PKA activity microdomains on the plasma membrane of living cells and uncover the role of clustered anchoring proteins in organizing these activity microdomains. Together, these findings suggest that biochemical activities of the cell are spatially organized into an activity architecture, whose structural and functional characteristics can be revealed by these new biosensors.

Introduction

Protein-based nanomachinery processes biochemical information and underlies all aspects of cellular function. Coordinated protein assembly and biochemical activity at specific loci in living cells ultimately leads to functional changes in cell growth, division, migration, or programmed death. An emerging picture is that these biochemical activities are dynamically regulated in various temporal waveforms[1,2] and spatially organized into distinct micro- or nano-domains[3–5]. The concept suggests that in addition to their physical structure, cells also maintain an “activity architecture” that is composed of organized, activated molecules and their regulatory partners. This model has not been directly tested, and critical questions about spatial organization of biochemical activities remain. The classical example of compartmentalized signaling is that of PKA, where PKA holoenzyme is anchored3 via A Kinase Anchoring Proteins (AKAPs) into signaling microdomains. However, this compartmentalization is achieved through the regulatory (R) subunits rather than the catalytic (C) subunits. PKA stimulation and subsequent release/diffusion of the C subunit would diminish this spatial compartmentalization. Therefore, even in this classical model, it is unclear whether and how the kinase activity is spatially organized in living cells. In recent years, many superresolution imaging methods that reveal the location of nanoscale cellular features[6,7] with vastly improved spatial resolution, such as STED[8], PALM/STORM[9, 10], SOFI/pcSOFI[11, 12], and SIM[13], have emerged. While there have been considerable efforts to move superresolution imaging beyond biomolecule localization[14–16], currently there is no general methodology to visualize dynamic biochemical activities such as protein-protein interactions and posttranslational modifications in live cells at superresolution. Here, we address this need by introducing a new class of generalizable, genetically encodable biosensors that enabled the first direct visualization of dynamic biochemical activities at a resolution beyond the diffraction limit. Using these new biosensors in combination with existing superresolution techniques, we report direct evidence of highly active PKA activity microdomains in the plasma membrane.

Results

Discovery and Characterization of FLINC

Examining the fluorescence dynamics of TagRFP-T in a series of plasma membrane-tethered constructs, we discovered that the proximity of Dronpa[17] significantly increases the fluorescence fluctuations of TagRFP-T[18]. We characterized this phenomenon using Dronpa-TagRFP-T (DpTT), where these two fluorescent proteins (FPs) are directly fused together by a short flexible linker. Several characteristics were revealed. First, fluctuations are easily detected in live cells expressing membrane targeted DpTT (Figure 3.1a, Figure 3.2). The single molecule fluorescence fluctuations generated by purified DpTT is quantitatively more robust than that from TagRFP-T (Figure 3.1b). Secondly, this effect occurs specifically between tethered Dronpa and TagRFP-T (Figure 3.1c). Thirdly, the external residues of Dronpa, not its chromophore, are key determinants of this effect (Figure 3.1d, Figure 3.2). Lastly, decreasing the distance between Dronpa and TagRFP-T by using rigid helical linkers of successively shorter lengths[19] revealed a corresponding increase in TagRFP-T fluorescence fluctuations (Figure 3.1e), indicating an effective range of 5–6 nm.

We termed this phenomenon Fluorescence fLuctuation INcrease by Contact (FLINC). Despite a low intrinsic affinity between Dronpa and TagRFP-T (Figure 3.3, Kd = 159–917 μM), the high effective concentrations in the fusions facilitate their intramolecular binding. While TagRFT-T, like many FPs, "blinks" stochastically[20, 21], the specific binding of Dronpa can alter the blinking behavior of TagRFP-T, making a larger percentage (25%) of TagRFP-T undergo dark-state conversion at a 25% faster rate (Figure 3.4). This photophysical mechanism gives rise to the modulated single molecule fluorescence fluctuation that can be utilized to assess whether Dronpa is in close proximity to TagRFP-T.

Figure 3.1 TagRFP-T (TT) red fluorescence fluctuations increase with Dronpa (Dp) proximity in a distance-dependent manner.

a). Representative images and single-pixel fluorescence intensity traces in HeLa cells expressing DpTT (Dronpa–linker–TagRFP-T), n = 7 cells) and TagRFP-T alone (n = 8), excited by a 561-nm laser. A.u., arbitrary units. Scale bar, 10 μm. b). Aggregated mean normalized autocorrelation function (ACF) of many single-molecule fluorescence traces from purified fluorescent DpTT and TagRFP-T. The amplitude increase demonstrates the clear gain in autocorrelation signal from increased millisecond fluctuations of DpTT. c). Quantified fluctuation in various constructs, demonstrating the specific nature of the fluctuation increase. TT (n = 8), DpTT (n = 7), Dp + TT (n = 9), EGTT (EGFP–linker–TagRFP-T, n = 8) and EGFP–linker–mCherry (EGmCh, n = 9) were analyzed. d). Quantified fluctuation in various mutant constructs, demonstrating that Dronpa's chromophore is not involved, but external Dronpa residues are important for the phenomenon. TT alone (n = 8), WT (n = 7); chromophore mutants (mut) DpS142D–TT (S142D, n = 8) and DpC62G Y63G–TT (GGG, n = 11); and FP surface mutants DpN102I–TT (N102I, n = 12) and DpN102I R149E–TT (NIRE, n = 9) were analyzed. e). A variable number of rigid helical repeats permit measurement of distance dependence and sensitivity of changes in fluctuation. Hn, number of rigid (EAAAK) repeats; DpTT (short linker) and Dp + TT (not fused) were included as comparisons. H2–H5 linkers are shown with the nominal FP distances reported in the

Figure 3.1 (continued) literature. All constructs in e were targeted to the plasma membranes of HeLa cells by the lyn sequence and examined for the following: DpTT (n = 5), H1 (n = 7), H2 (n = 6), H3 (n = 14), H4 (n = 17), H5 (n = 10) and Dp + TT (n = 9). Pairwise t-test results in c–e are shown for data compared with the reference (ref) construct. NA, not applicable; NS, not significant; *P < 0.05; **P < 0.01; ***P < 0.001. In all dot plots and e, center line and whiskers mark the average and s.e.m., respectively. N numbers reflect individual cells (biological replicates).

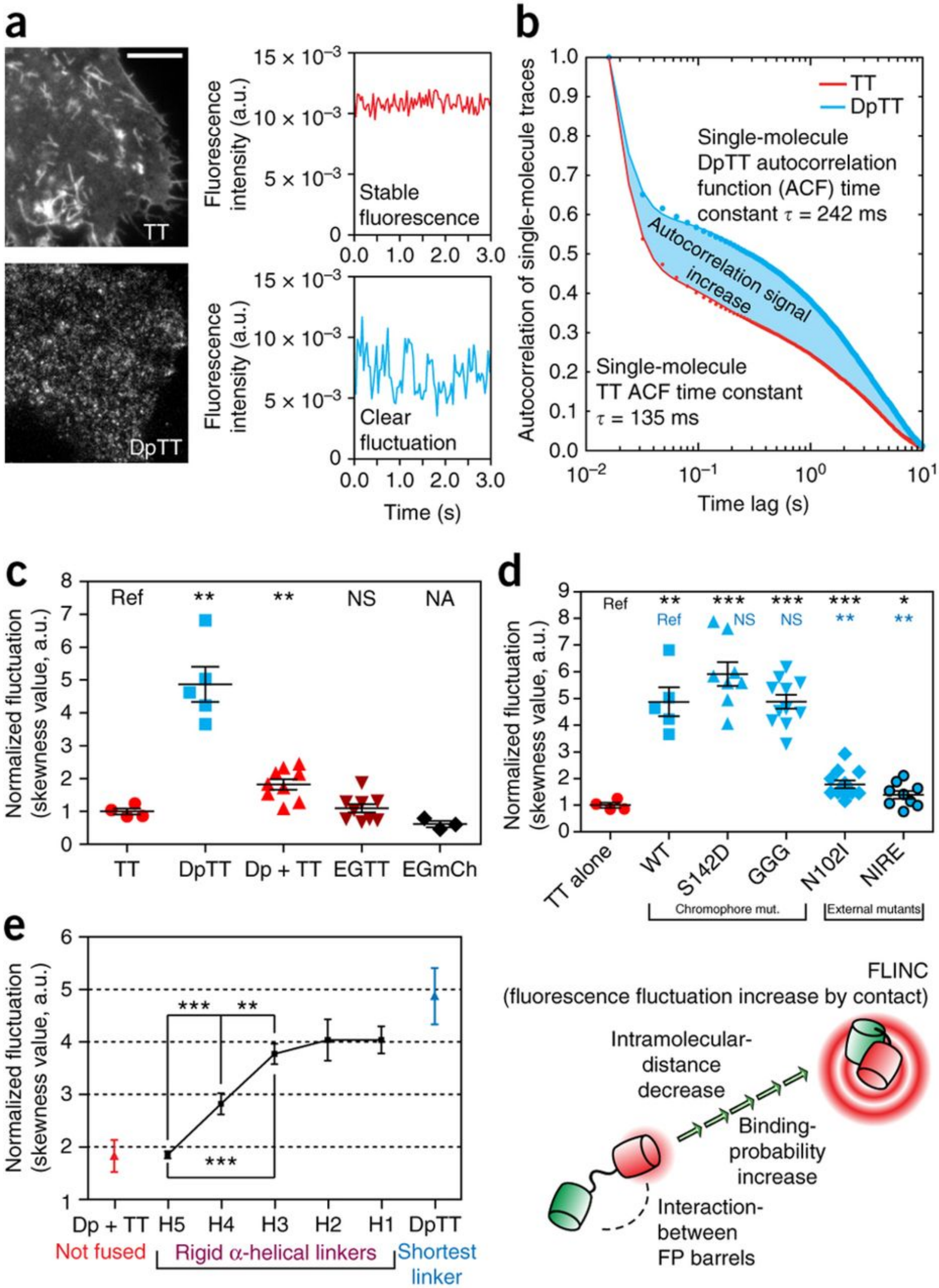
a
TT
DpTT
Fluorescence intensity (a.u.)
15 × 10⁻³
10 × 10⁻³
5 × 10⁻³
0
Stable fluorescence
Clear fluctuation
0.0 1.0 2.0 3.0
Time (s)
b
Autocorrelation of single-molecule traces
TT
DpTT
Single-molecule DpTT autocorrelation function (ACF) time constant τ = 242 ms
Autocorrelation signal increase
Single-molecule TT ACF time constant τ = 135 ms
Time lag (s)
c
Normalized fluctuation (skewness value, a.u.)
Ref ** ** NS NA
TT
DpTT
Dp + TT
EGTT
EGmCh
d
Normalized fluctuation (skewness value, a.u.)
Ref ** *** *** *** *
Ref NS NS ** **
TT alone
WT
S142D
GGG
N102I
NIRE
Chromophore mut.
External mutants
e
Normalized fluctuation (skewness value, a.u.)
*** **
***
Dp + TT
H5
H4
H3
H2
H1
DpTT
Not fused
Rigid α-helical linkers
Shortest linker
FLINC
(fluorescence fluctuation increase by contact)
Intramolecular-distance decrease
Binding-probability increase
Interaction-between FP barrels

Figure 3.2 Additional Characterization in the Discovery of FLINC

a). Representative images from a single, 35 ms exposure using 561 nm laser on HeLa cells expressing DpTT and control constructs: TagRFP-T alone (TT), co-targeted Dronpa and TagRFP-T (Dp+TT), Dronpa-linker-TagRFP-T (DpTT), EGFP-linker-TagRFP-T (EGTT). Scale bar: 10 μm. b). Averaged fluorescence intensity of HeLa cells expressing various constructs. n numbers are: TT (8), DpTT (7), Dp+TT (9), EGTT (8), and EGFP-linker-mCherry (EGmCh, n=9). c). Representative images from a single, 35 ms exposure using 561 nm laser on HeLa cells expressing mutant DpTT constructs: Dp[S142D]-TT (S142D), Dp[C62G/Y63G]-TT (GGG), Dp[N102I]-TT (N102I), Dp[N102I/R149E]-TT (NIRE). Scale bar: 10 μm. d). Averaged fluorescence intensity of HeLa cells expressing various mutant and control constructs; tandem model DpTT containing wild-type Dronpa (WT), singly-expressed TagRFP-T (TT-alone). n numbers are: TT-alone (8), WT (7), S142D (8), GGG (11), N102I (12), and NIRE (9). e). Normalized skewness quantification demonstrates that Dronpa fluctuation is not significantly affected by co-transfection (Dp+TT) or fusion (DpTT) with TagRFP-T on the membrane of HeLa cells. f). Normalized average fluorescence intensity of bacterial colonies in error-prone (K178R, N208K) and site-directed (residues N102 and R149) mutagenesis. Pair-wise t-test results in (B), (D), (E) are marked where data were compared with the construct marked “ref”; n numbers are marked in the corresponding columns. n.s.: not-significant; *: $p<0.05$; **:

Figure 3.2 (continued) $p<0.01$; ***: $p<0.001$ where applicable. Center line and whiskers mark mean and s.e.m. values, respectively. N numbers reflect individual cells (biological replicates)

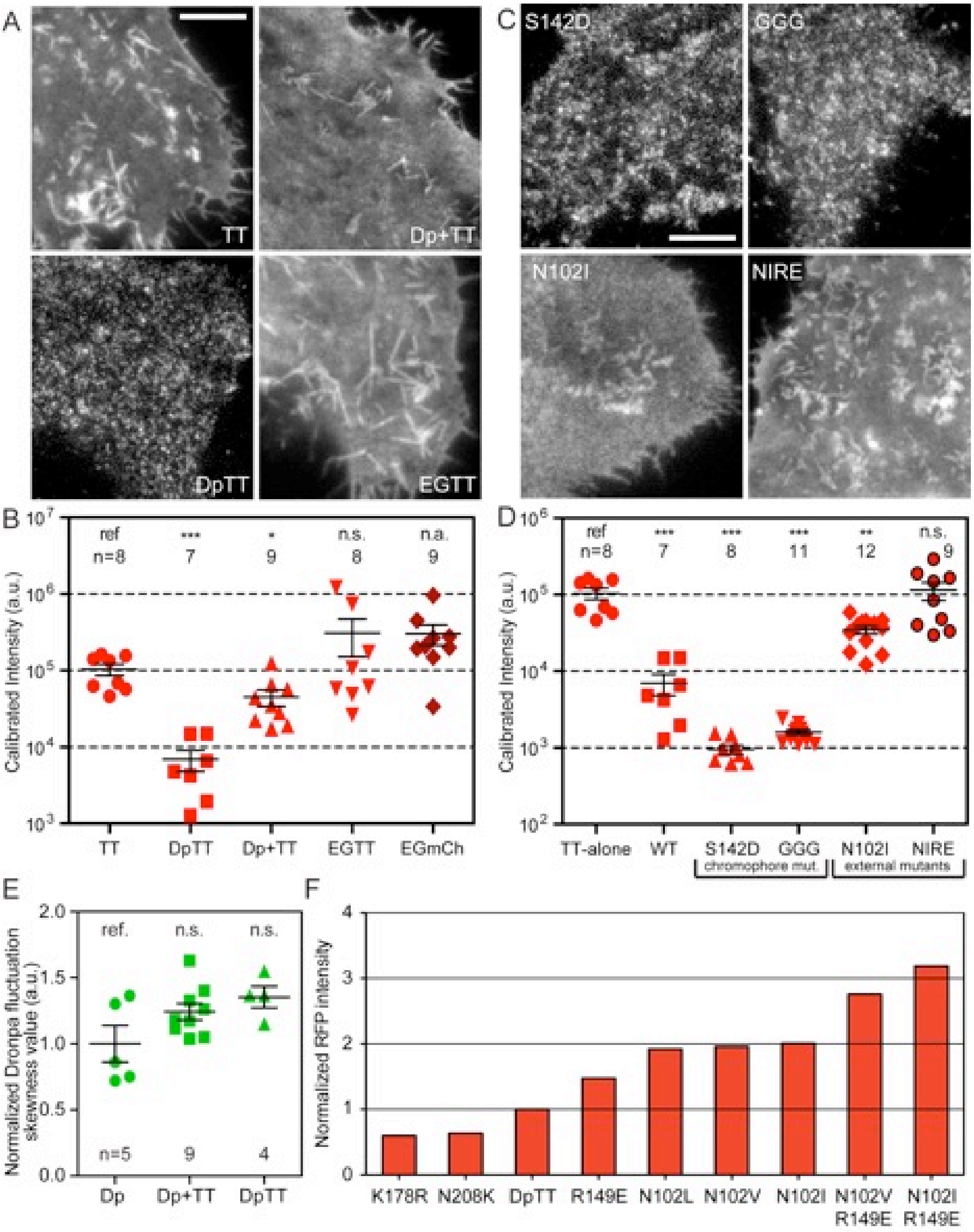

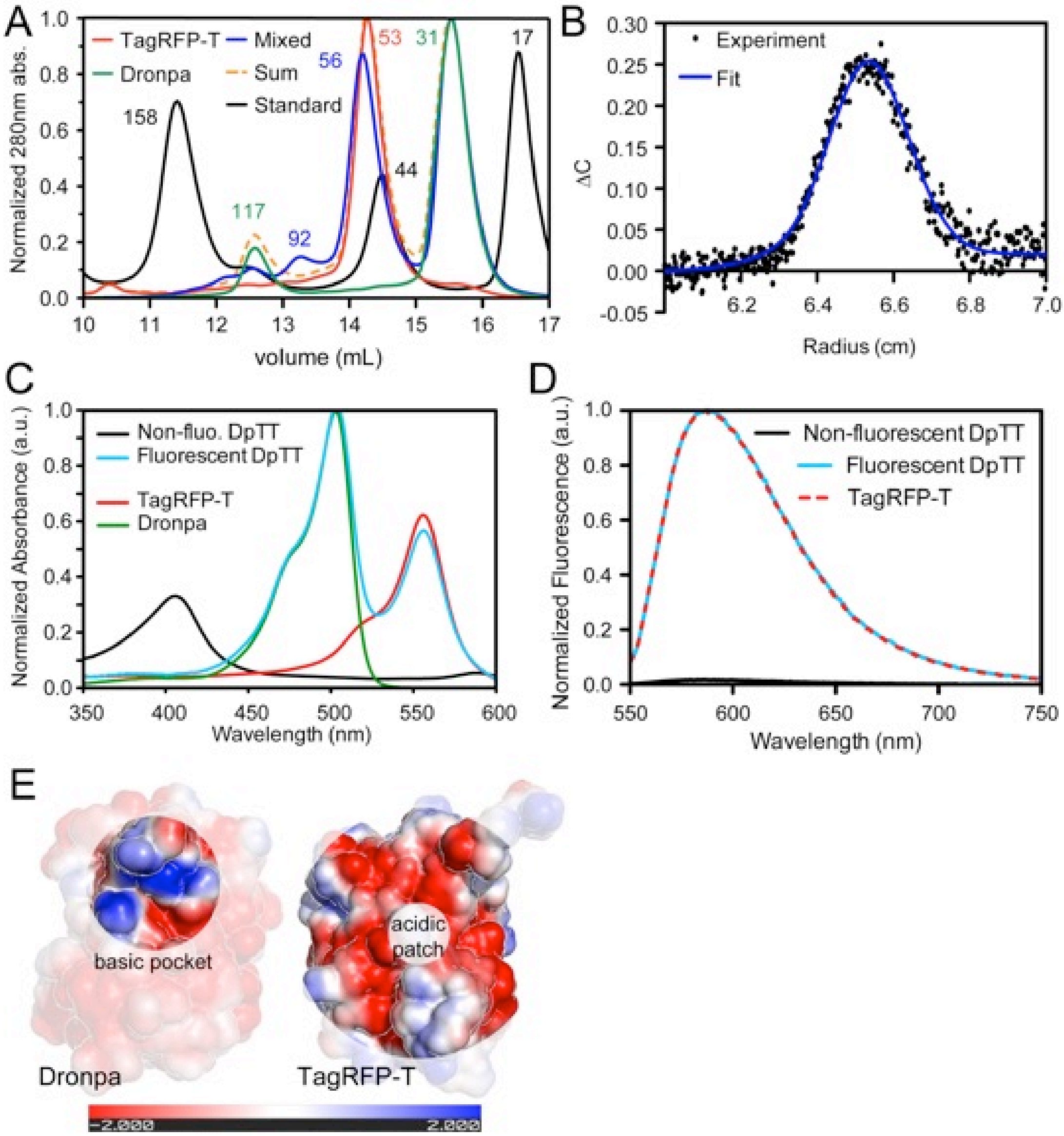

Figure 3.3 In Vitro Characterization of FLINC

a). Size-exclusion chromatography permits a qualitative assessment of the interaction between Dronpa and TagRFP-T. Sizes of the protein oligomers are as indicated. A peak at 92 kDa was observed only in the mixed solution, indicating a trace amount of a 3-fluorescent-protein hetero-oligomer formed at protein concentrations of 60 μM each. Color codes: red, TagRFP-T; green, Dronpa; orange, algebraic sum of Dronpa/TagRFP-

Figure 3.3 (continued) T chromatographs; blue, mixture. b). SedAnal plot of ΔC as a function of cell radius for fitting of Dronpa+TagRFP-T mixed sample data from analytical ultracentrifugation. The experimental data are shown as black dots, while the calculated fitting curve for the A + B ↔ C model is shown as a solid blue line. Data from scans 55 to 100 are included in this fit; the input parameters include: S(Dronpa) = 2.15, S(TagRFP-T) = 3.30, and S(Dronpa+TagRFP-T) = 4.0. c). Absorption and d). fluorescence spectroscopy of purified DpTT fractions compared to TagRFP-T or Dronpa. e). Electrostatic surfaces of Dronpa and TagRFP-T calculated by the Adaptive Poisson-Boltzmann Solver (APBS) plug-in in PyMOL. The basic pocket in Dronpa and the acidic patch around the chromophore in TagRFP-T, both features believed to be important for FLINC, have been highlighted.

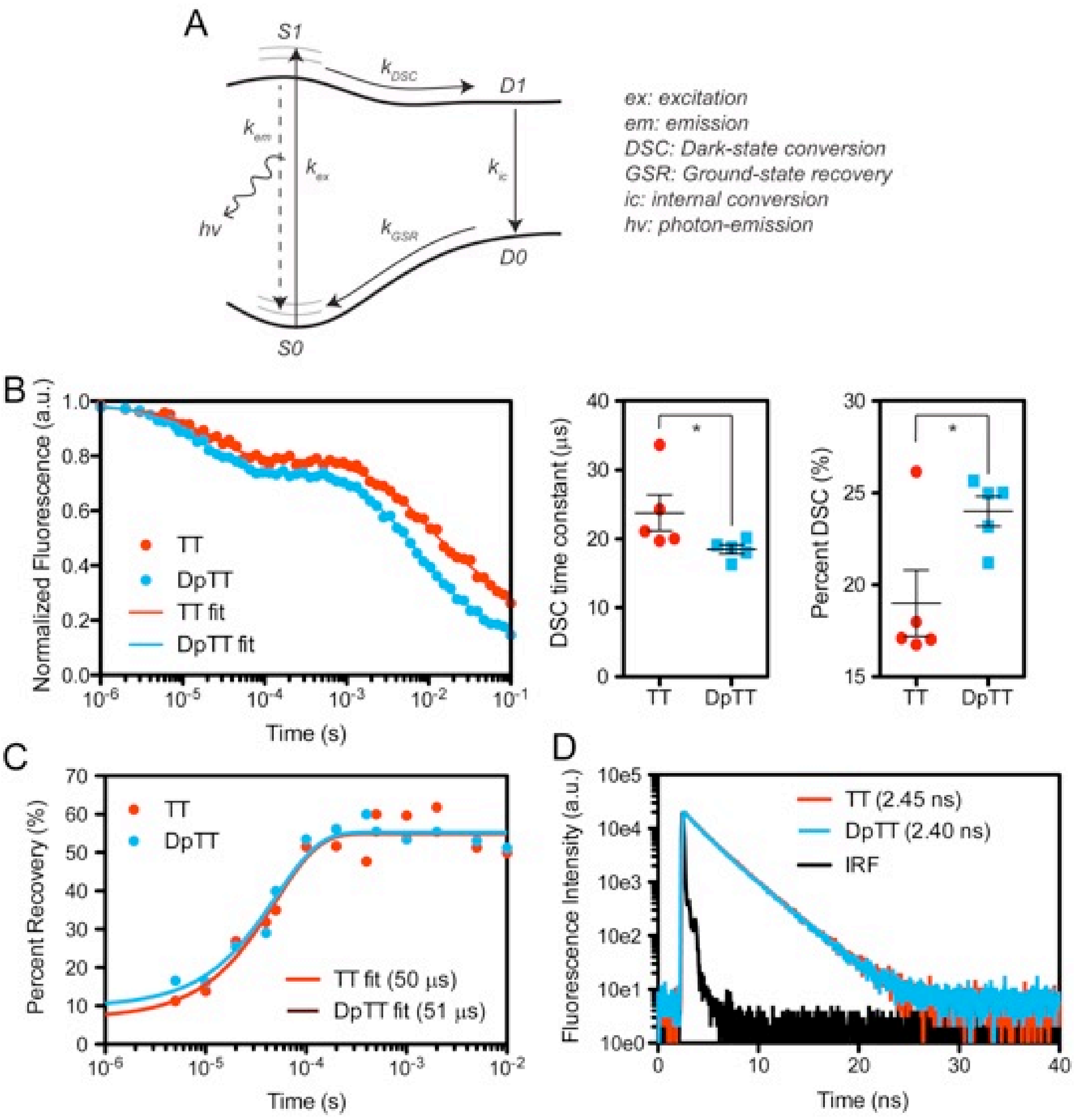

Figure 3.4 The photophysical characteristics differences between DpTT and TT (TagRFP-T) is mainly observed in dark-state conversion

a). A simplified schematic depicting the 4-state model of the TagRFP-T chromophore transition. b). Results of the Dark-State Conversion (DSC) measurement and fit. The bottom two figures summarize the difference in

Figure 3.4 (continued) DSC time constant and Percent DSC. c). Results of the Ground-State Recovery (GSR) measurement and fit. d). Results of the fluorescence (em) life time measurement; IRF is instrument response function. Pair-wise t-test results in (b) are marked where data were compared with the construct marked “ref”; n numbers are marked in the corresponding columns. *: $p<0.05$. Center line and whiskers mark mean and s.e.m. values, respectively.

FLINC-Based Biosensors

FLINC therefore forms the basis of a new class of fluorescent biosensors that could provide activity information in superresolution. Engineered molecular switches can modulate the proximity between Dronpa and TagRFP-T in a manner similar to FRET-based biosensors[22]. The output of these FLINC-based biosensors is activity-dependent changes in the fluorescence fluctuations, which are readily quantified at superresolution using photochromic Stochastic Optical Fluctuation Imaging (pcSOFI)[11]. In pcSOFI, time series of fluorescence images are recorded to obtain many single molecule fluctuations across the field of view. Pair-wise cross-cumulant, calculated utilizing the appropriate pixel-pairings, yields an autocorrelation-like “pcSOFI value” at sub-pixel resolution that quantifies the strength of fluctuation[23] with high signal-to-noise (Figure 3.5). The collection of pcSOFI values constitutes a quantitative image, which provides a superresolution map of the biochemical activity under study.

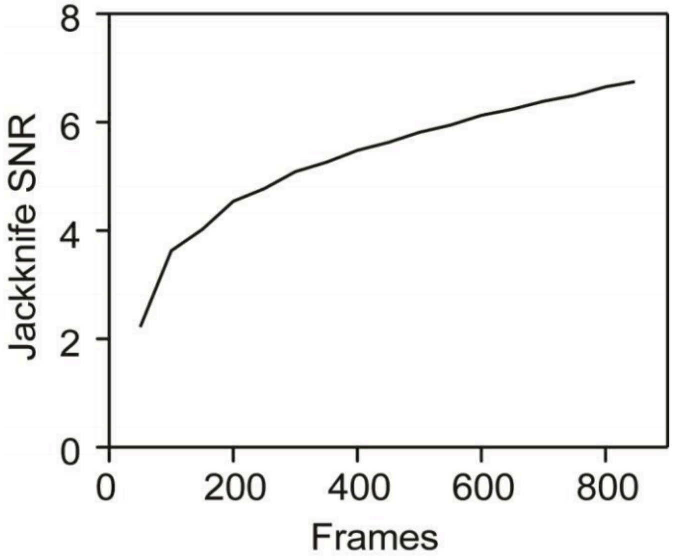

Figure 3.5 Signal-to-noise estimation for pcSOFI imaging

Jackknife resampling on a typical FLINC dataset demonstrates the accuracy of pcSOFI imaging in terms of signal-to-noise ratio (SNR). We obtain a high SNR of 6.7.

We modeled FLINC-based activity biosensors after FRET-based biosensors, which serve as surrogate substrates of the kinase of interest. Phosphorylation of these biosensors leads to a change of fluorescence properties, thereby allowing us to monitor kinase activity by imaging a reporter, without labeling or disrupting the active kinase. In the FLINC-based PKA biosensor, we combined the molecular switch in AKAR[24] with an EV linker (AKARev)[25] with Dronpa and TagRFP-T into FLINC-AKAR1 (targeted to the plasma membrane). Here, FLINC would be affected in a phosphorylation-dependent manner, such that high pcSOFI values indicate high PKA activities (Figure 3.6a). Normalizing the pcSOFI values to correct for uneven biosensor distribution (Figure 3.7), we could quantify PKA activity both at the single pixel level or averaged across the entire cell. The average normalized pcSOFI value rapidly increased in the first minute after PKA activation in HeLa cells treated with a cocktail of the adenylyl cyclase activator forskolin (Fsk) and phosphodiesterase inhibitor 3-isobutyl-1-methylxanthine (IBMX), reaching a plateau at 25–39% increase after 7–10 minutes (Figure 3.6b-d) and showing a dynamic range of up to 40% increase. Addition of the PKA-specific inhibitor H-89 (20 μM) gradually decreased the average normalized pcSOFI value, demonstrating the reversibility. Additional experiments using a negative control biosensor that cannot be phosphorylated (Figure 3.6c-d) and membrane-targeted PKA inhibitor PKI (Figure 3.6c) demonstrated that the response was dependent on phosphorylation of the biosensor and PKA activity, respectively. Time courses with H-89 inhibition and submaximal dosage of Fsk (Figure 3.8) showed that FLINC-AKAR1 could accurately report over a range of PKA activity. We could quantify PKA activity initially every 5 minutes (Figure 3.6c), and with further development every 30 s (Figure 3.6d). The kinetics of PKA stimulation as monitored by FRET-based or FLINC-based AKAR showed no significant difference (FRET t1/2 = 1.2 min, n = 7; FLINC t1/2 = 0.73 min, n = 4). Importantly, our analysis of FLINC-AKAR1 fluctuations generated superresolution images of PKA activity at each time point throughout the treatment course. Monitoring the same profile line in the normalized pcSOFI images before and after Fsk/IBMX treatment (Figure 3.6e) showed that we can resolve sub-diffraction-limit activity features (Figure 3.6f) that have responded to stimulation. Actin-targeted FLINC-AKAR1 enabled us to distinguish the stimulated PKA activity with an average Gaussian full-width-half-maximum of 179 ± 6 nm (n = 7) and 116 ± 6 nm (n = 7), consistent with the respective use of second- and third-order analyses (Figure 3.9a-b). Furthermore, we could resolve the stimulated membrane PKA activity in converging filopodial features separated by 160 nm and 107 nm using second- and third-order cumulant analyses, respectively (Figure 3.9c-d). Under the conditions described here, biosensor diffusion does not affect the temporal and spatial resolution of pcSOFI11 and its accurate quantification of FLINC. Thus, as a reporter of kinase activity, FLINC-AKAR1 provides not only a consistent readout for PKA activity, but also allows us to monitor the dynamic changes of PKA activity with high contrast at superresolution.

Figure 3.6 FLINC resolves PKA activity microdomains on the plasma membrane at super-resolution.

a). Schematic of the FLINC–AKAR design principle, the domain structure of FLINC–AKAR1 and the acquisition of super-resolution activity images with pcSOFI. b). FLINC–AKAR1 super-resolution images clearly resolve the response to Fsk/IBMX stimulation (Fsk 50 μM and IBMX 100 μM) and inhibition (H-89 20 μM), and detailed spatial information on membrane PKA activity emerges. Color scales are identical. c). Mean normalized pcSOFI response time course from live HeLa cells expressing WT (n = 9 cells) FLINC–AKAR1, nonphosphorylatable mutant (TA, n = 7) and WT coexpressed with PKI (WT + PKI, n = 4), after PKA stimulation and inhibition. d). The normalized pcSOFI response time course from live HeLa cells expressing WT (n = 4) FLINC–AKAR1 and nonphosphorylatable mutant (TA, n = 5), after PKA stimulation and inhibition, determined with a fast acquisition imaging scheme. e). A profile line at the same position across the pcSOFI images before and after Fsk/IBMX (FI) stimulation clearly demonstrates sensing of PKA activity at super-resolution; the profile is marked by a red line in b. f). Zoom view of the active PKA feature (p1) in f, showing resolution of the Gaussian fitting and full width at half maximum (FWHM) size of this subdiffraction-limit PKA activity microdomain. g). Comparison of the changes in the fraction of membrane area occupied by punctate structures after stimulation across various FLINC constructs, all targeted with the

Figure 3.6 (continued) same CAAX motif. In FLINC–AKAR1 experiments, cells (WT, $n = 10$; TA, $n = 8$) were stimulated with Fsk/IBMX; in DpTT experiments, cells ($n = 8$) received no drug treatment. Unless indicated otherwise, pairwise t-test results are shown for data compared with the reference (ref) construct. NS, not significant; $^{**}P < 0.01$. In c and d, center line and whiskers mark the average and s.e.m., respectively.

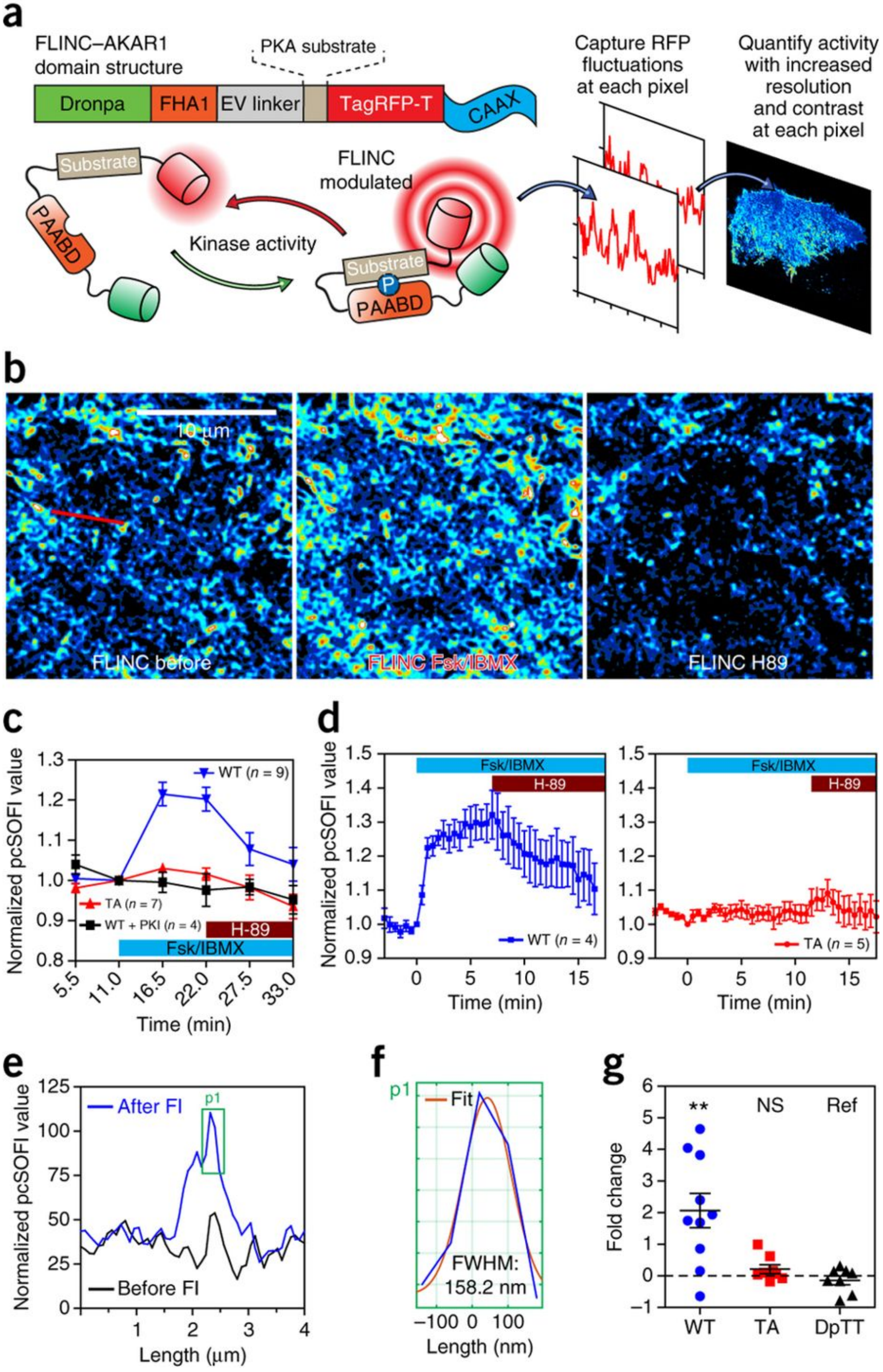
a
FLINC–AKAR1 domain structure
PKA substrate
Dronpa
FHA1
EV linker
TagRFP-T
CAAX
Substrate
PAABD
Kinase activity
FLINC modulated
Substrate
P
PAABD
Capture RFP fluctuations at each pixel
Quantify activity with increased resolution and contrast at each pixel
b
10 μm
FLINC before
FLINC Fsk/IBMX
FLINC H89
c
Normalized pcSOFI value
WT (n = 9)
TA (n = 7)
WT + PKI (n = 4)
H-89
Fsk/IBMX
1.3
1.2
1.1
1.0
0.9
0.8
5.5
11.0
16.5
22.0
27.5
33.0
Time (min)
d
Normalized pcSOFI value
Fsk/IBMX
H-89
1.5
1.4
1.3
1.2
1.1
1.0
0.9
WT (n = 4)
0
5
10
15
Time (min)
Fsk/IBMX
H-89
TA (n = 5)
Time (min)
e
Normalized pcSOFI value
After FI
p1
Before FI
125
100
75
50
25
0
1
2
3
4
Length (μm)
f
p1
Fit
FWHM: 158.2 nm
−100
0
100
Length (nm)
g
Fold change
**
NS
Ref
6
5
4
3
2
1
0
−1
WT
TA
DpTT

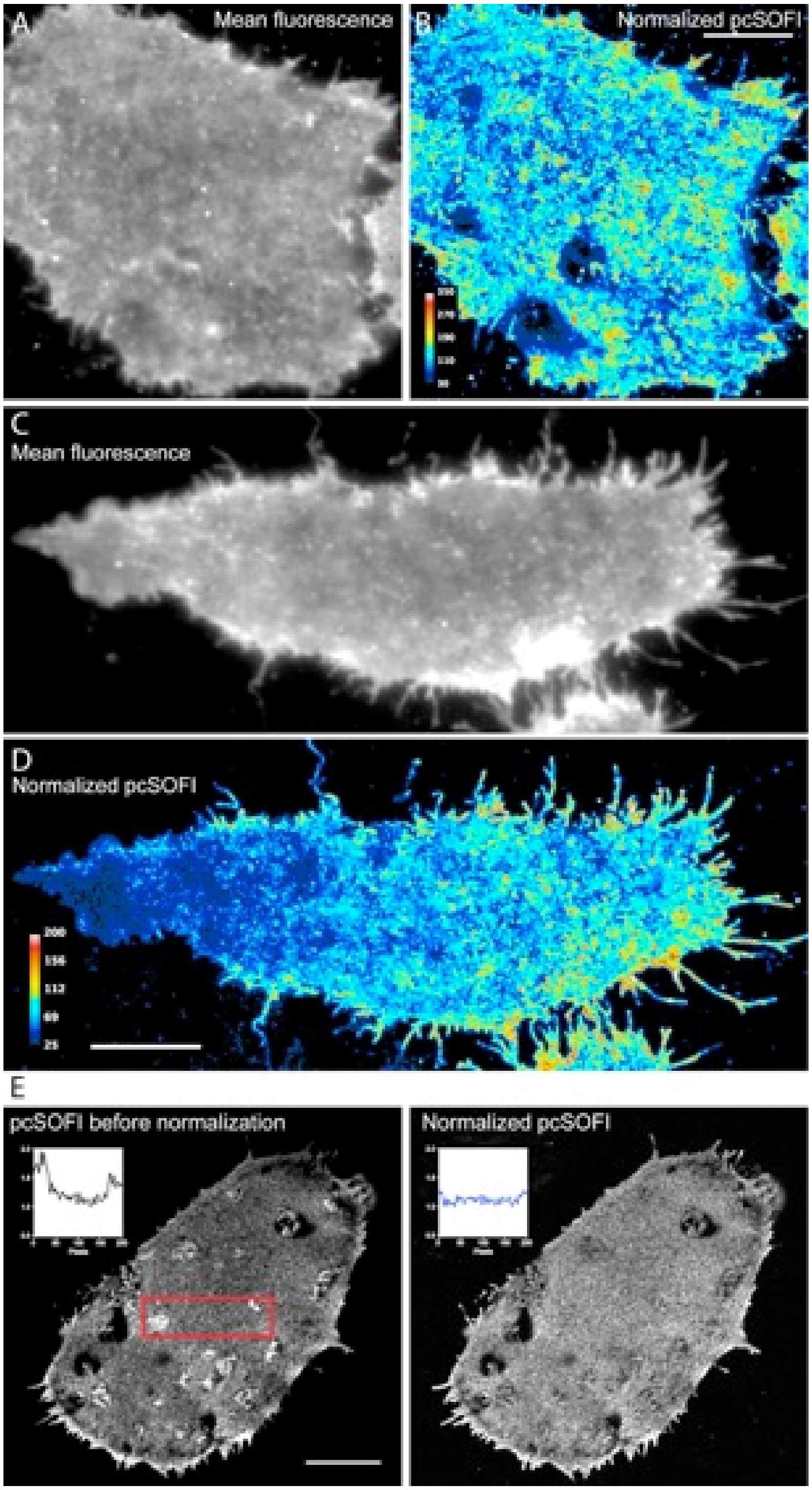

Figure 3.7 Validation for pcSOFI Normalization Algorithm

a). and c). show average fluorescence images of plasma membrane targeted FLINC-AKAR1, where uneven distribution of the probe could be

Figure 3.7 (continued) observed. b). and d). show normalized pcSOFI images of the same cells. e). The effectiveness of the pcSOFI normalization scheme is demonstrated by performing normalization on HeLa cells expressing membrane targeted Dronpa. Normalization removes the clearly present concentration bias, as seen by the profile (averaged along the y-axis of the region indicated by the red box). All scalebars are 10 μm.

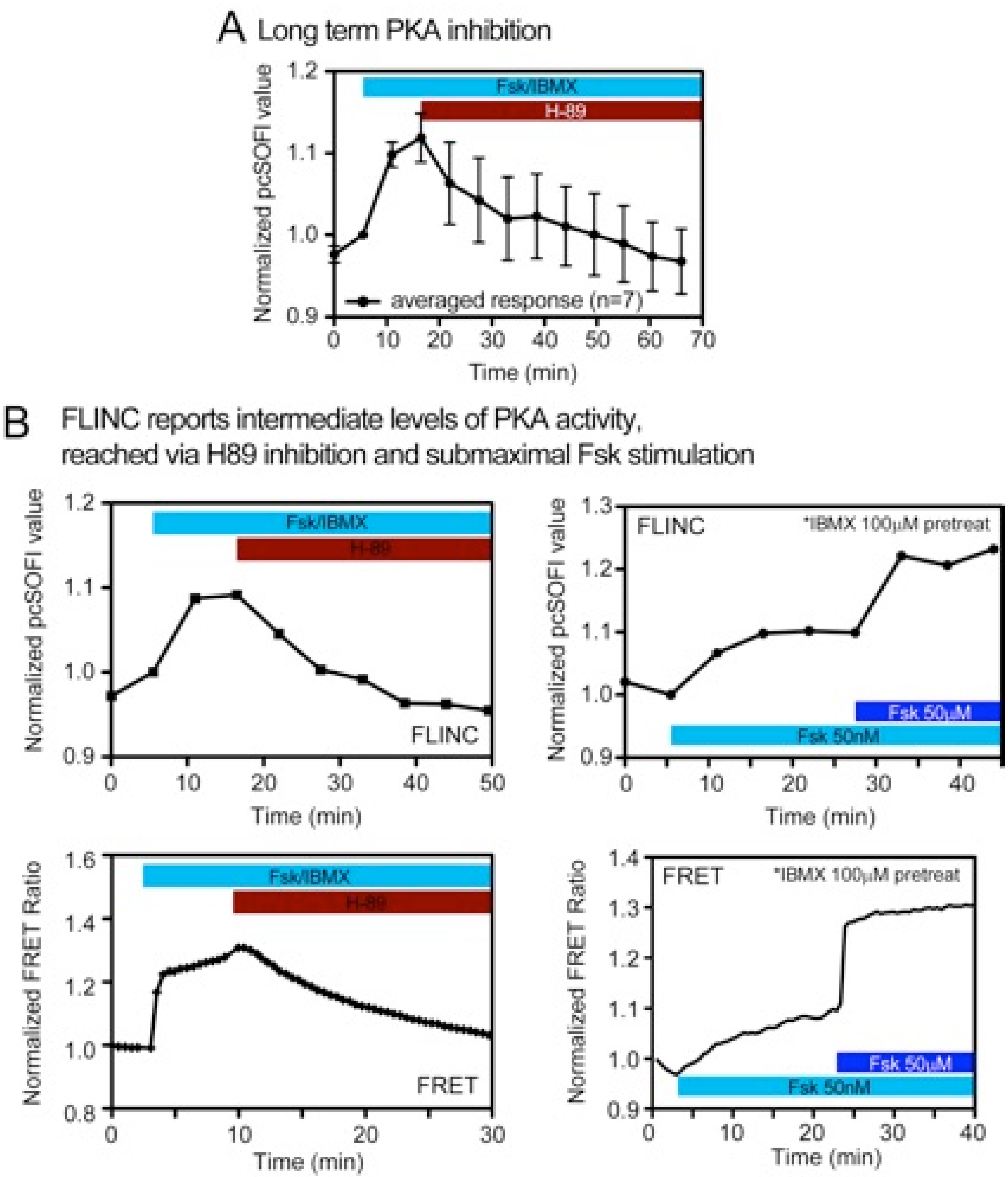

Figure 3.8 Additional control data supporting the accuracy, biological relevance and function of FLINC biosensing

a). Treatment of Fsk/IBMX stimulated HeLa cells with 20 μM H89 over time can inhibit PKA activity to baseline levels. b). FLINC-AKAR1 is

Figure 3.8 (continued) sensitive to intermediate levels of PKA activity as demonstrated by representative response during 1) H89 inhibition (left column of b), and 2) submaximal forskolin (Fsk) dosage (right column of b). The response of the FRET-based biosensor is provided for comparison in each case. In (a), center line and whiskers mark mean and s.e.m. values, respectively.

Figure 3.9 Resolution analyses of FLINC-KAR biosensors

In each row, the feature can be located in the mean fluorescence (Avg) images, and the enzyme activity detected from the feature is shown in the pcSOFI images, labeled by order of calculation. a-b). Resolution analyses on lifeact-targeted FLINC-AKAR1, where the PKA activity detected on actin filament under different treatments is quantified by either 2nd or 3rd order pcSOFI. The profile of the filament at the red line was plotted in the graph to the right. The activity profile before and after Fsk/IBMX stimulation of PKA are shown to highlight the sensing of activity during superresolution imaging. After Gaussian fitting of many filament profile lines, the average FWHM the filaments were found to be 179±6 nm (n=7) and 116±6 nm (n=7) for (a) 2nd and (b) 3rd order pcSOFI images, respectively. (c-e) Resolution analyses using filopodia features. In each panel, the mean fluorescence (Avg) and the pcSOFI (2nd or 3rd order) image of the same region of interest are shown, while the profiles of the active feature marked by the red dashed line were plotted in the graph to the right. As demonstrated by a graph and a surface plot to aid the eye at the right end of rows c-e, the joints of two filopodial features can be clearly resolved across 3 pixels, allowing the spatial resolution to be estimated. We find a resolution of 160 nm for the 2nd order pcSOFI with FLINC-AKAR1 (c), a resolution of 107 nm for the 3rd order pcSOFI with FLINC-AKAR1 (d), and a resolution of 160 nm for 2nd order pcSOFI with FLINC-EKAR (e).

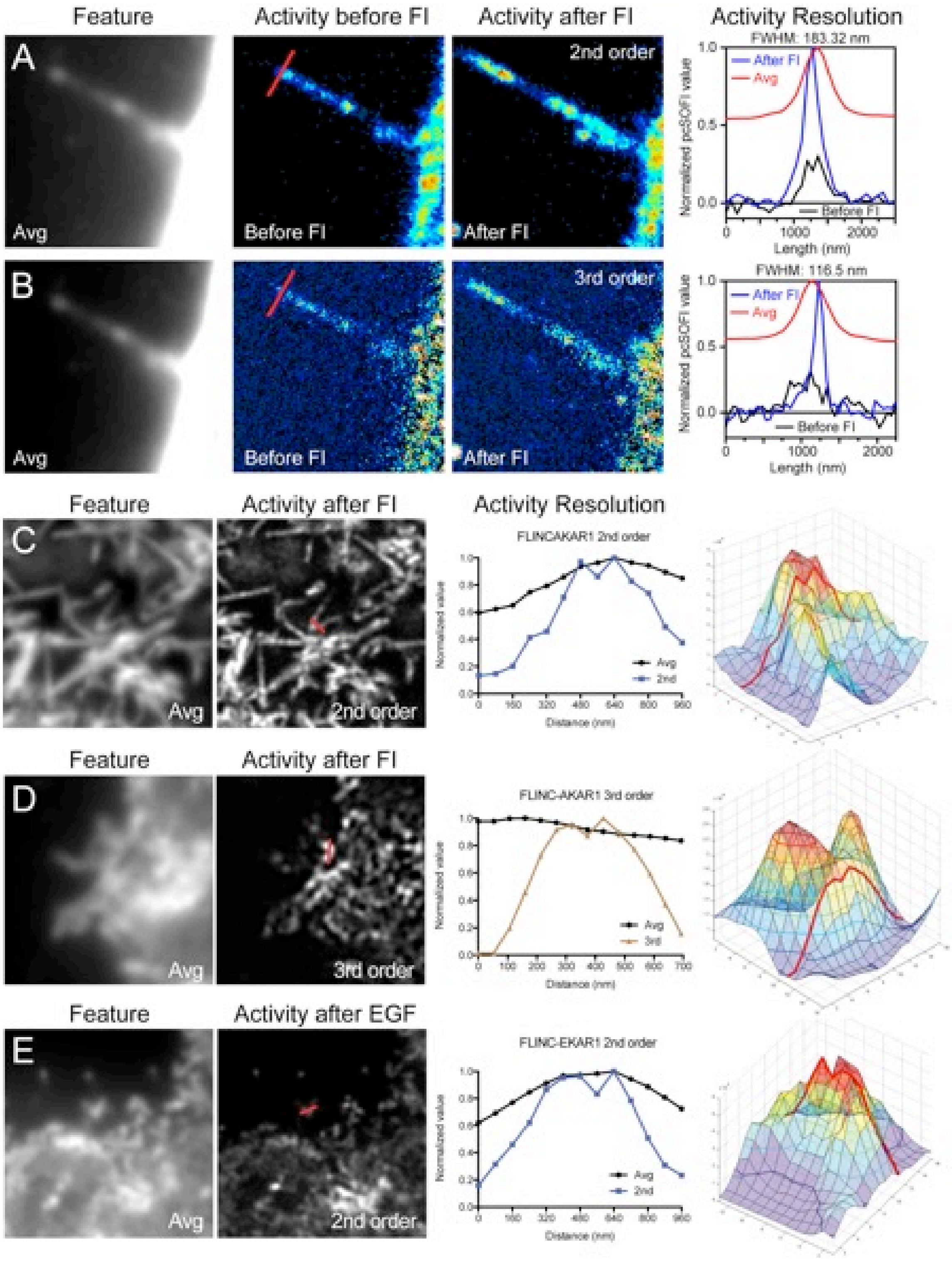
Feature
Activity before FI
Activity after FI
Activity Resolution
A
Avg
Before FI
2nd order
After FI
FWHM: 183.32 nm
After FI
Avg
Before FI
Normalized pcSOFI value
Length (nm)
B
Avg
Before FI
3rd order
After FI
FWHM: 116.5 nm
After FI
Avg
Before FI
Normalized pcSOFI value
Length (nm)
Feature
Activity after FI
Activity Resolution
C
Avg
2nd order
FLINCAKAR1 2nd order
Normalized value
Distance (nm)
Avg
2nd
Feature
Activity after FI
D
Avg
3rd order
FLINC-AKAR1 3rd order
Normalized value
Distance (nm)
Avg
3rd
Feature
Activity after EGF
E
Avg
2nd order
FLINC-EKAR1 2nd order
Normalized value
Distance (nm)
Avg
2nd

PKA Activity Microdomains

The PKA activity maps generated by FLINC-AKAR1 revealed many minute and highly active punctate features on the basal membrane of living cells. These activity puncta, with a mean diameter of 350 nm, were clearly resolved after Fsk/IBMX stimulation. Activating PKA induces a 2-fold increase in microdomain coverage over the basal membrane, and is not observed with the DpTT control or the non-phosphorylatable mutant (TA) (Figure 3.6g). Using Stochastic Optical Reconstruction Microscopy (STORM) in total internal reflection fluorescence (TIRF) condition, we further verified the presence of these highly active PKA microdomains. Phospho-PKA-substrates (p-PKAsub) were clearly clustered (Figure 3.10a-b), forming distinct microdomains on the basal membrane with a mean diameter of approximately 250 nm (Figure 3.10c). The basal membrane of cells stimulated by Fsk/IBMX again displayed a significant 4.8 fold increase in phospho-PKA-substrate clusters per unit membrane area (Figure 3.10d). All these characteristics observed in STORM are consistent with those observed using FLINC-AKAR1 in live cells. Thus, despite the conventionally held views of rapid cAMP diffusion[26–30] and mobility of PKA catalytic subunits[31,32], PKA activity is not uniform but confined within microdomains on the plasma membrane of living mammalian cells.

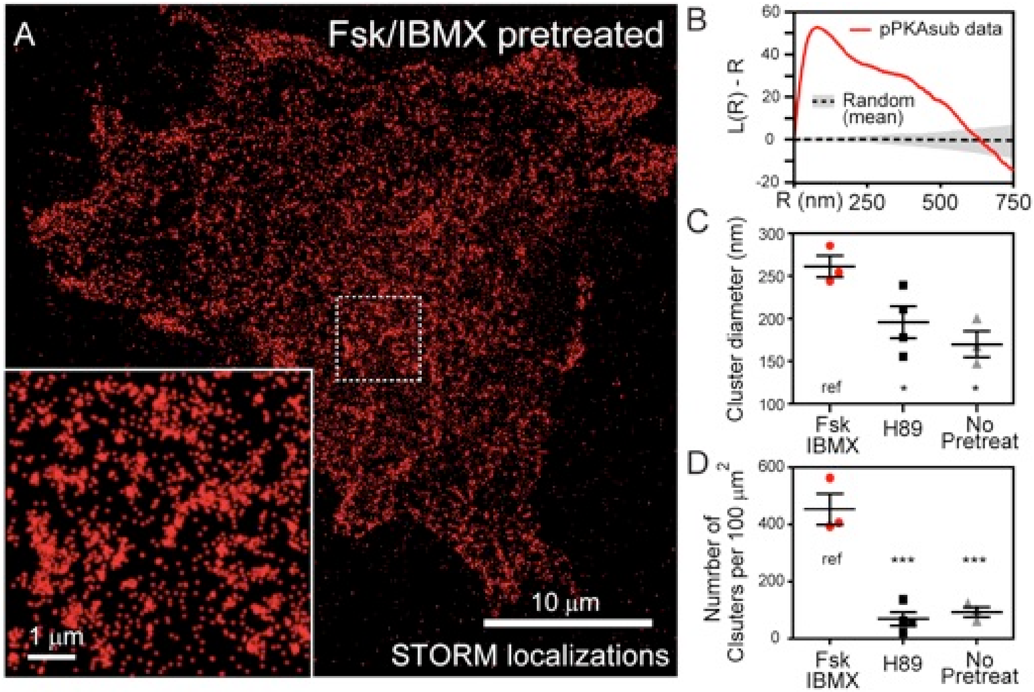

Figure 3.10 STORM superresolution imaging of PKA activity microdomains using a phospho-PKA substrate antibody

a). A representative view of the p-PKAsub localization on the basal membrane of HeLa cells. Inset: a zoom-view illustrating the PKA microdomains observed. b). Ripley's K analysis of p-PKAsub localizations show clear clustering above random sampling. The average clustering length scale is 102 nm (n = 3). c). and d). Mean-shift clustering analysis reveals the average cluster diameter and number of clusters on the basal membrane, respectively, upon Fsk/IBMX stimulation (n=3 cells), H89 inhibition (n=4 cells), and without pretreatment (n=3 cells). Unless indicated otherwise, pair-wise t-test results are marked where data were compared with the construct marked "ref". n.s.: not-significant; *: $p<0.05$; **: $p<0.01$; ***: $p<0.001$ where applicable. In c) and d), center line and whiskers mark mean and s.e.m. values, respectively.

Clustered anchoring proteins spatially organize PKA activity microdomains

AKAPs are critical components of the PKA compartmentalization. We set out to directly determine the precise spatial relationship between highly active PKA microdomains and the loci of specific PKA anchoring. AKAP79/AKAP5 is a doubly-lipidated, predominately membrane-localized scaffold known to associate with RII PKA holoenzymes and other regulators of PKA signaling[33,34]. Two-color STORM imaging in fixed cells (Figure 3.11a-b) showed that AKAP79 was itself highly clustered (Figure 3.11c, Figure 3.12a-b), with a mean diameter of 127 nm. Getis-Franklin co-clustering (Figure 3.11d) demonstrated a high degree of spatial correlation between AKAP79 and p-PKAsub (Figure 3.12c). 76% of total AKAP79 localizations, whether in clusters or dispersed, were associated with p-PKAsub microdomains. Surprisingly, however, a total of 24% of AKAP79 localizations could not be associated with p-PKAsub, suggesting heterogeneity of AKAP-mediated complexes and that a sub-pool of these complexes could be regulated differentially, e.g. due to a difference in phosphatase activity. Through a combination of AKAP79 localization and FLINC-AKAR1 imaging in the same cells, we observed characteristics that mirrored those reported above. Significant overlap with PKA activity microdomains was observed above random clustering (Figure 3.11c), and we again observed so-called “orphaned” AKAP79 molecules.

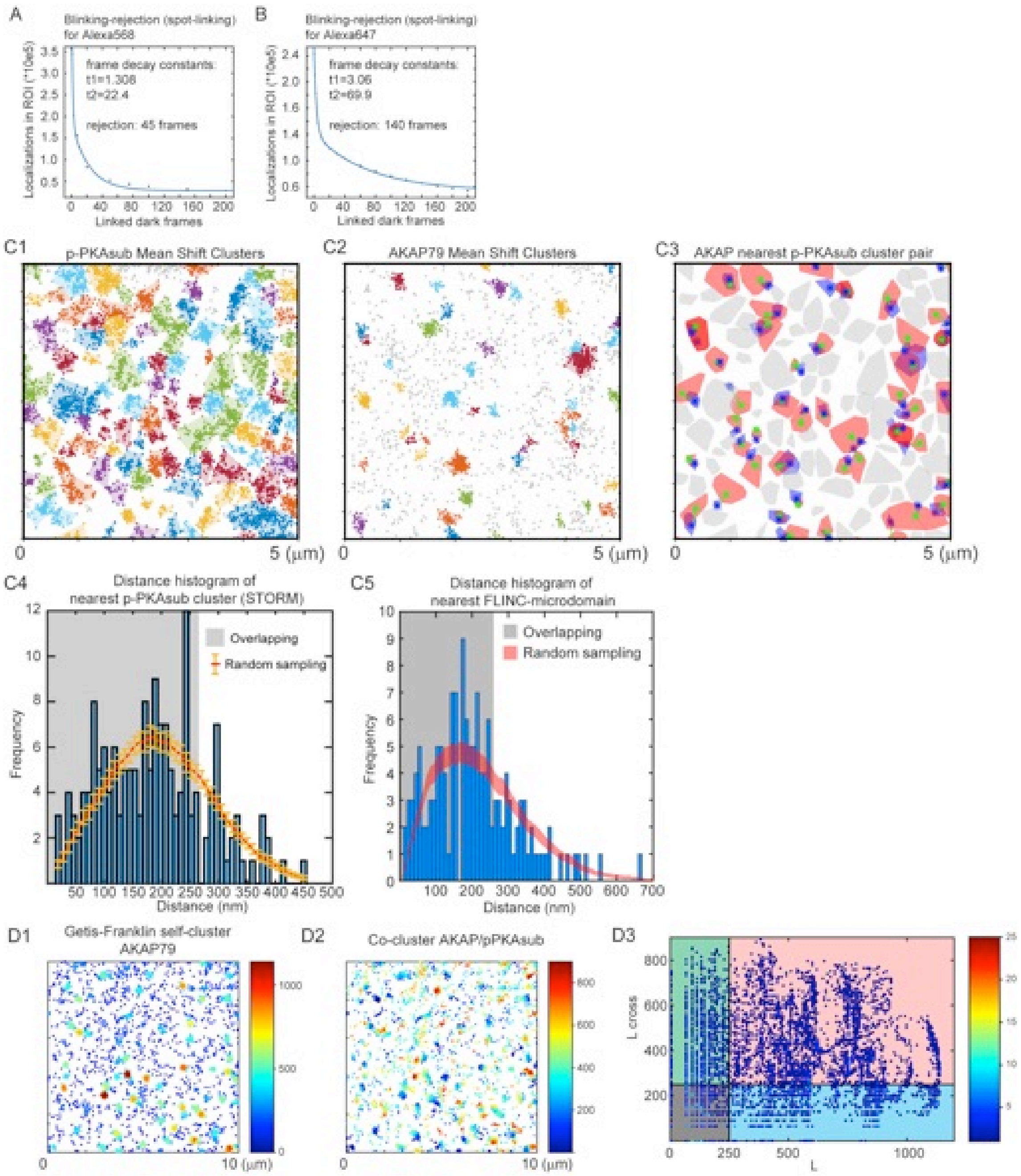

Figure 3.11 Representative data analysis for STORM imaging and STORM/FLINC imaging

a). and b). Double exponential fit and parameters for the spot-linking or blinking-rejection utilized in post-processing of STORM dataset in Alexa568 and Alexa647 dyes, respectively. All data were treated by spot-

Figure 3.11 (continued) linking prior to further analysis to avoid over-counting. c). Representative processing from mean-shift clustering analysis. c1). Identification and clustering of phospho-PKA substrates localizations; c2). Identification and clustering of AKAP79 localizations; c3). Convex-hull cluster pairs highlighting the AKAP79 clusters (blue) and their respective phospho-PKA substrate clusters (red). c4). Histogram displaying the frequency of occurrence for centroid distances between AKAP79 clusters and their respective nearest p-PKAsub clusters; representative of n=5 cells. c5). Histogram displaying the frequency of occurrence for centroid distances between AKAP79 and FLINC microdomain; representative of n=5 cells. d). Representative processing from the Getis-Franklin co-clustering analysis. d1). Self-clustering of AKAP79 by Getis-Franklin, which is a precursor to co-clustering analysis; red color indicates increasing tendency of clustering. d2). Co-clustering analysis plotl; red color indicates increasing tendency of clustering. d3). Representative quadrant analysis from Getis-Franklin co-clustering, reported in Figure 3.12c.

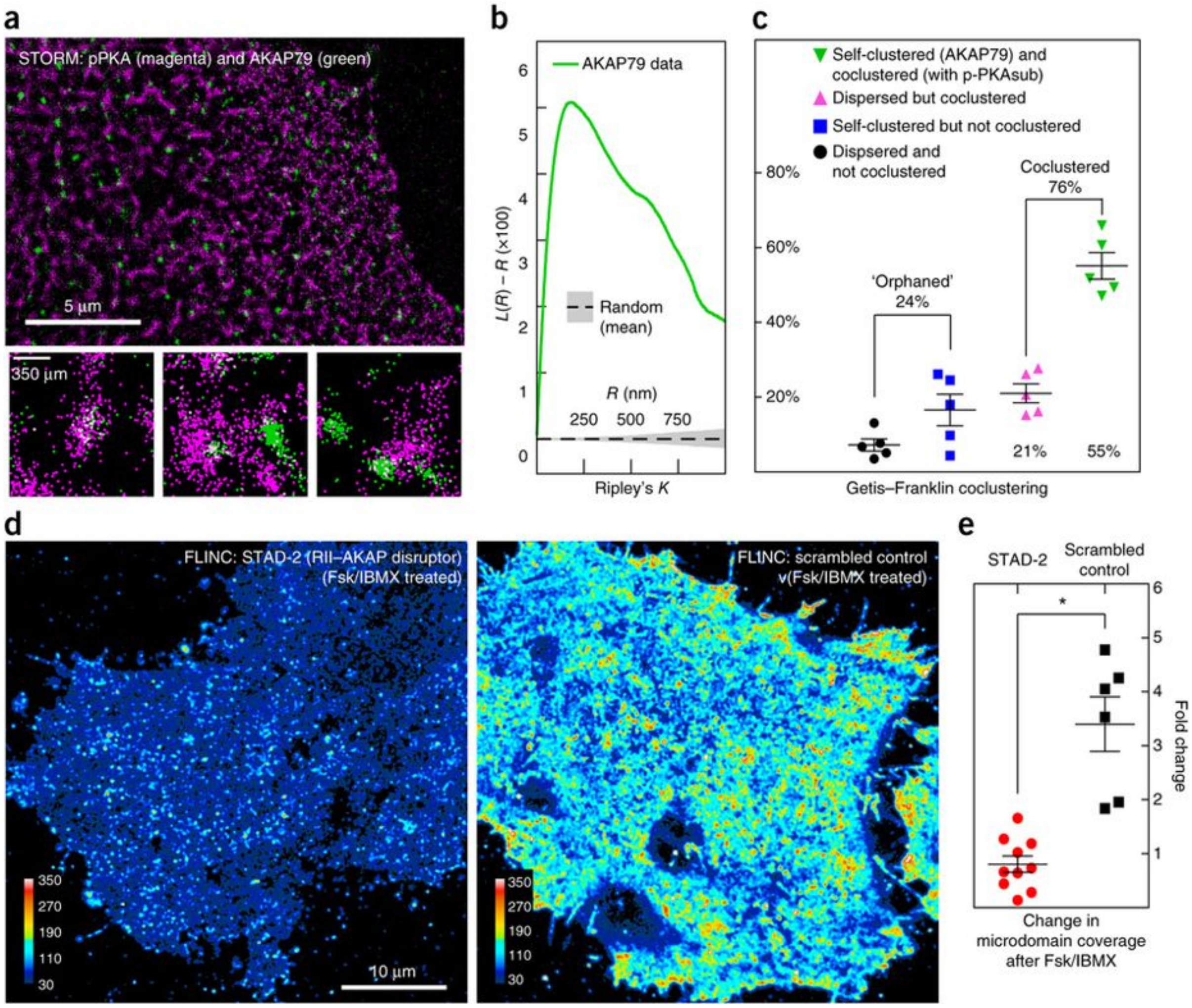

Figure 3.12 A kinase–anchoring proteins (AKAPs) are coclustered with PKA activity microdomains and are required for microdomain formation

a). A representative two-color STORM image of p-PKAsub (magenta) and AKAP79 (green), with specific examples of the p-PKAsub/AKAP79 relationship shown beneath. b). (n = 5 cells) Ripley's K analysis of AKAP79 localizations shows clear clustering above random sampling. c). Getis–Franklin coclustering analyses of the two-color STORM images,

Figure 3.12 (continued) identifying populations with different p-PKAsub/AKAP79 relationships; the majority (55 + 21 = 76%) of AKAP79 is associated with p-PKAsub (n = 5). d). Representative live-cell super-resolution FLINC–AKAR1 images of stimulated PKA activity after the disruption of AKAP–PKA RII interactions with a synthetic AKAP disruptor, STAD-2 (n = 10), in comparison with its scrambled control (n = 6). Scale bar, 10 μm. The color scales are identical. e). The effect of RII–AKAP disruption on PKA activity microdomains, quantified by fold change in microdomain coverage. Cells were pretreated with either STAD-2 (n = 10) or scrambled peptide control (n = 6) before Fsk/IBMX stimulation. Unless indicated otherwise, pairwise t-test results are shown for data compared with the reference (ref) construct. *$P < 0.05$. In c and e, center line and whiskers mark the average and s.e.m., respectively.

Next we tested whether, beyond a high degree of spatial correlation, AKAP anchoring is required for the formation of highly active membrane PKA microdomains in living HeLa cells. To this end, we used the synthetic peptide (STAD-2), which specifically disrupts the interaction between AKAPs and the PKA regulatory subunit RII isoform[35]. Consistent with previous observations, the membrane PKA activity in living cells pretreated with STAD-2 was low after Fsk/IBMX stimulation (Figure 3.13) and devoid of highly active PKA microdomains, in contrast to cells treated with scrambled peptide (Figure 3.12d,e). These live cell data indicated that beyond a high degree of spatial correlation, PKA activity microdomains require anchoring by AKAPs such as AKAP79.

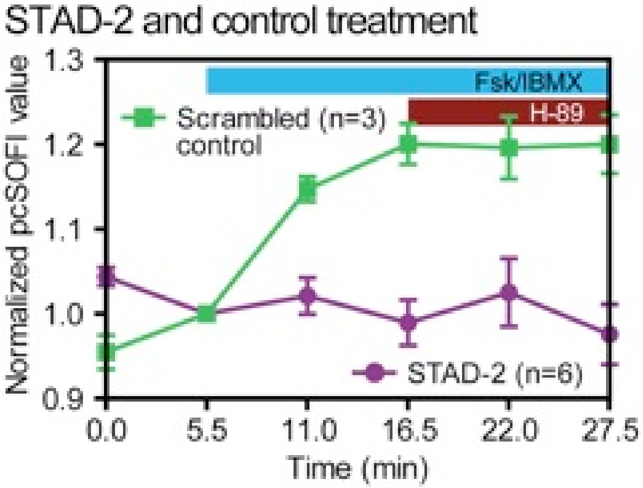

Figure 3.13 Normalized pcSOFI response to inhibition by STAD-2 and its scrambled peptide control

STAD-2 treatment (n=6) to dissociate PKA-RII subunit from A Kinase Anchoring Proteins (AKAP) inhibited membrane PKA activity while scrambled-control peptide (n=3) did not.

Polarized Distribution of Activity Microdomains

Having confirmed that cells do maintain a well-structured PKA spatial signaling architecture, we next examined the presence and organization of highly active PKA microdomains during integrin-dependent cell migration, which requires effective polarization. Chinese Hamster Ovary cells stably expressing α4 integrin (α4CHO) exhibit a gradient of PKA activity as they migrate toward wounds[36]. This migration-dependent PKA gradient was resolved at superresolution using live α4CHO cells expressing FLINC-AKAR1 (Figure 3.14a). The difference between the normalized pcSOFI values in the leading and that in trailing regions was highly significant (WT, Figure 3.14b) and absent in cells expressing the non-phosphorylatable biosensor (TA, Figure 3.14c). Inhibiting PKA activity globally using H-89 markedly suppressed PKA activity in the leading front, whereas the trailing edge showed little change (Figure 3.15). The gradient observed using FLINC was approximately linear (Figure 3.14d), similar to that seen using a FRET-based biosensor36. However, the superresolution images reveal that the leading front of the cell hosted many microdomains of high PKA activity, which were missing in the trailing end. With a median diameter of approximately 280 nm, these highly active microdomains in CHO cells displayed significantly different levels of PKA activity depending on their subcellular location, with most elevated activity at the filopodia. In 8/9 cells, microdomains within the filopodia displayed a significantly higher PKA activity as compared to those on the remainder of the basal membrane (Figure 3.14e), consistent with the model that a pool of PKA molecules (such as integrin-anchored Type I PKA) are highly active at the very tip of migrating cells[37]. These data suggest that distinct PKA microdomains in the same cell can have differentially regulated amplitude and spatiotemporal characteristics.

FLINC is a General Platform for Biosensing

To demonstrate the generalizability of the design, we constructed a FLINC biosensor for Extracellular signal-Regulated Kinase (ERK) activity based on EKARev[25] (Figure 3.15a). In HEK293 cells expressing plasma membrane-targeted FLINC-EKAR1, pcSOFI values again provided consistent and robust ERK activity readouts. Stimulation of ERK using epidermal growth factor (EGF, 100 ng/mL) increased the averaged normalized pcSOFI value by 21–27% within 10 minutes (WT, Figure 3.16b n = 16). Stimulation in cells expressing a non-phosphorylatable mutant biosensor or pretreated with an upstream inhibitor of ERK (U0126, 20 μM) gave no response (TA/pretreat, Figure 3.16b). The superresolution ERK activity maps (Figure 3.16c) showed a similar resolution enhancement of 160 nm at second-order (Figure 3.9e).

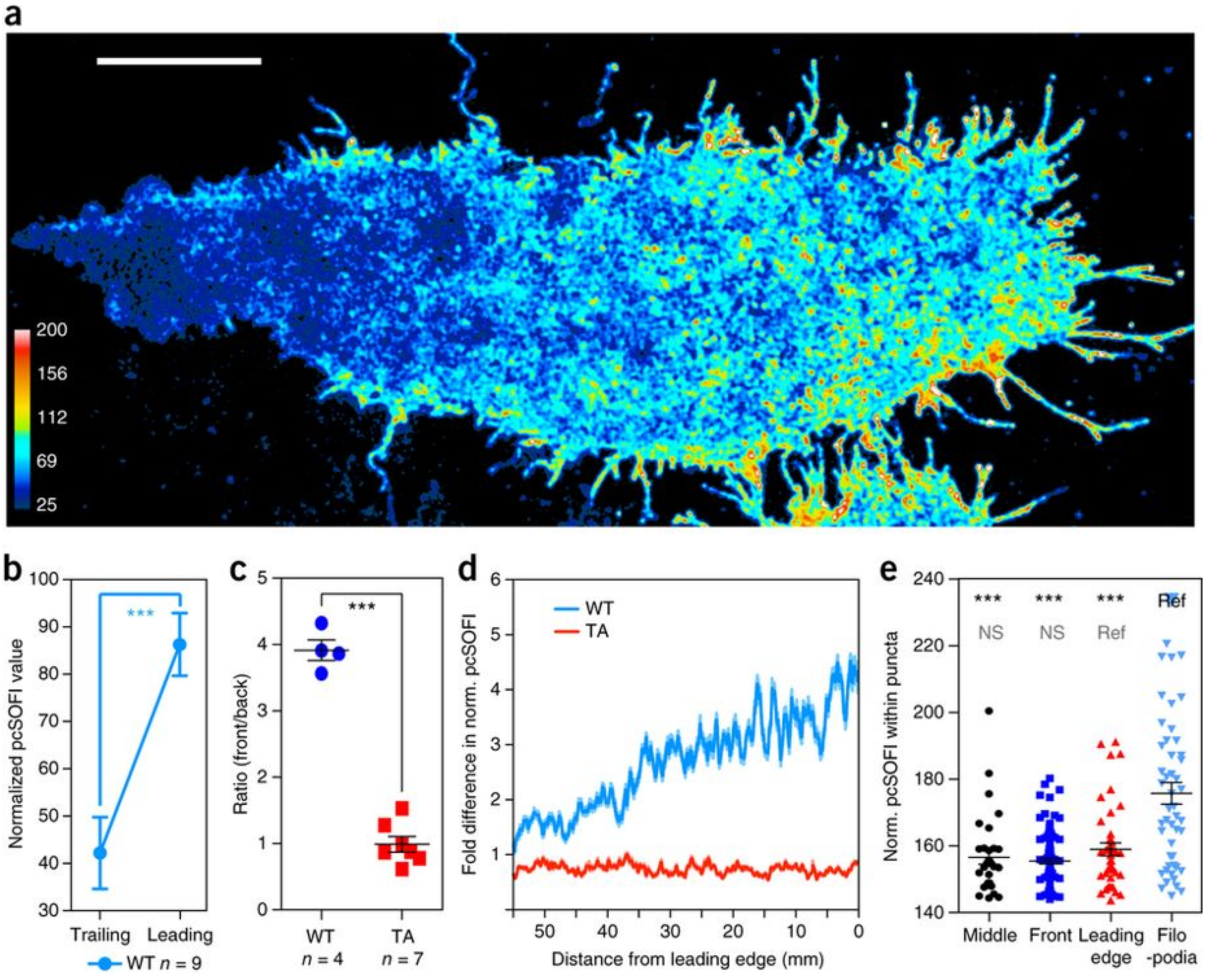

Figure 3.14 PKA activity gradient of a migrating cell at super-resolution.

a). The PKA activity gradient in a migrating α4CHO cell expressing WT FLINC–AKAR1. Scale bar, 10 μm. b). Average normalized (norm) pcSOFI values within leading- and trailing-edge regions of migrating cells show clearly different PKA activities. c). Migrating α4CHO cells expressing WT FLINC–AKAR1, compared with cells expressing a nonphosphorylatable TA mutant, show a significant gradient in terms of normalized pcSOFI values. Pairwise t-test results are shown. d).

Figure 3.14 (continued) Representative PKA activity profile (n = 9 cells) observed along the migration direction, for FLINC–AKAR1 and its TA mutant. e). Representative data (n = 9) showing that active microdomains within the filopodia have significantly higher PKA activity than that elsewhere on the basal membrane of migrating CHO cells; basal-membrane regions are indicated according to their increasing distance from the leading edge of the migration direction (filopodia, leading edge, front and middle) (n = 9). Unless indicated otherwise, pairwise t-test results are shown for data compared with the reference (ref) construct. NS, not significant; ***$P < 0.001$. In c and e, center line and whiskers mark the average and s.e.m., respectively.

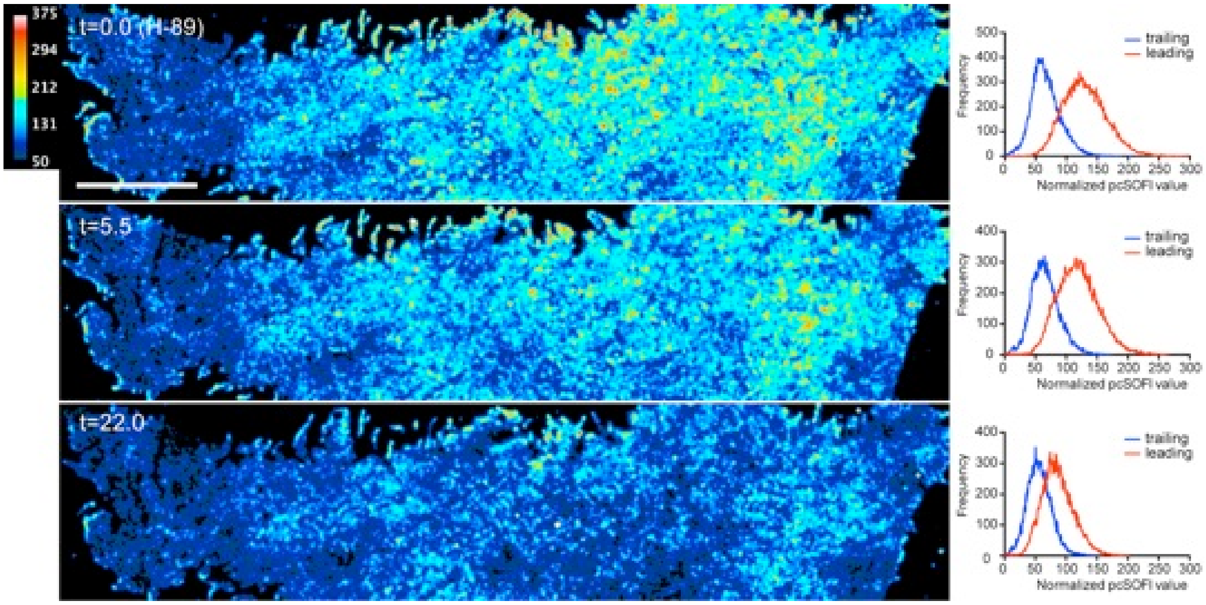

Figure 3.15 Inhibition of global PKA activity using H-89 reduces PKA activity at the leading front

Normalized pcSOFI images and their corresponding histograms for a migrating α4 CHO cell at t=0 min, 5.5 min, and 22 min after addition of 20 μM of H-89, a PKA inhibitor. All images are displayed using the same color scale. A shift to lower normalized pcSOFI values was observed for the leading region, but not the trailing region, of the cell. Scale bar: 10 μm.

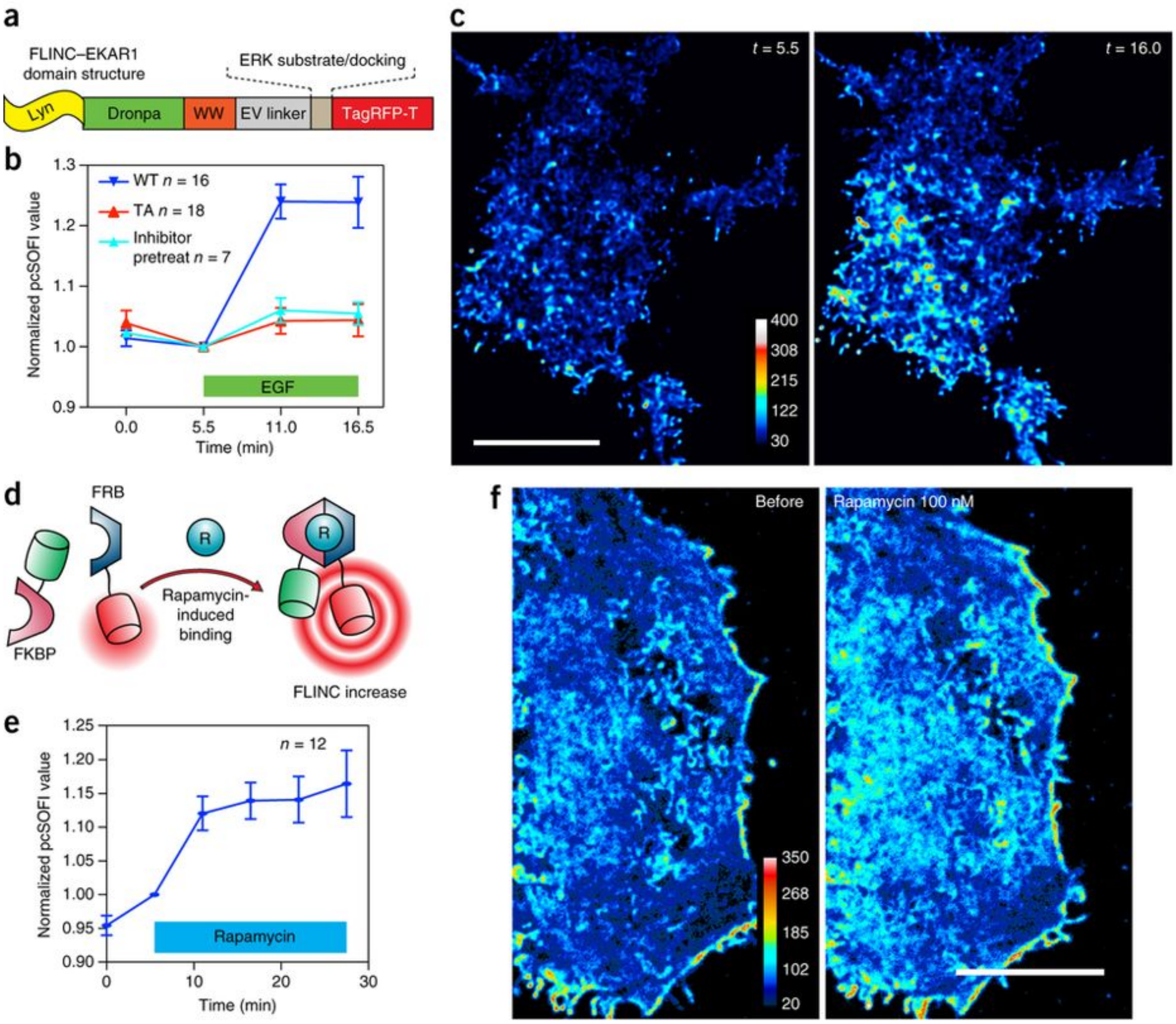

Figure 3.16 FLINC-based design is generalizable.

a). Domain structure of FLINC–EKAR1. b). Normalized pcSOFI response time course from live HEK293 cells expressing WT FLINC–EKAR1 (n = 16 cells), nonphosphorylatable mutant (TA, n = 18) FLINC–EKAR1 and cells expressing WT but pretreated with the ERK upstream inhibitor U0126 (20 µM; inhibitor pretreat, n = 7), all subjected to growth-factor stimulation (EGF 100 µM). c). Representative super-resolution images (n = 16) of ERK activity dynamics after growth-factor stimulation and

Figure 3.15 (continued) chemical inhibition. Scale bar, 10 μm. d,e). Schematic of the design (d) and normalized pcSOFI time course of the bimolecular PPI sensor based on FKBP–rapamycin–FRB (n = 12) in response to rapamycin (100 nM) (e). f). Normalized pcSOFI images of a HeLa cell before and after stimulation with rapamycin to induce the dimerization between FKBP and FRB. Scale bar, 10 μm. The color scales for the before and after images are identical in c and f, respectively.

FLINC could also be harnessed to monitor protein-protein interactions (PPI), and we demonstrate this by using the inducible dimerization system of cytosolic FK506 Binding Protein (FKBP) and membrane targeted FKBP12-Rapamycin Binding domain (FRB, Figure 3.15)[38]. Addition of rapamycin (100 nM) led to the rapid heterodimerization of FKBP and FRB, which could be detected by a fast normalized pcSOFI value increase across the cell membrane that plateaued at 15% in 20 minutes (Figure 3.16e,f). When optimized, FLINC can also detect weaker PPI. We split FLINC-AKAR1 into two separate constructs consisting of a diffusible FHA1-Dronpa and a membrane-targeted PKA-substrate-TagRFP-T. PKA phosphorylation of the substrate recruits cytosolic FHA1 and induce a corresponding normalized pcSOFI signal increase, even though the affinity between FHA1 and phospho-substrate is ~ 0.5 μM[39] (Figure 3.17). These examples showcase the generalizability of FLINC-based biosensors and its potential to enhance the dissection of spatially organized biochemical activities.

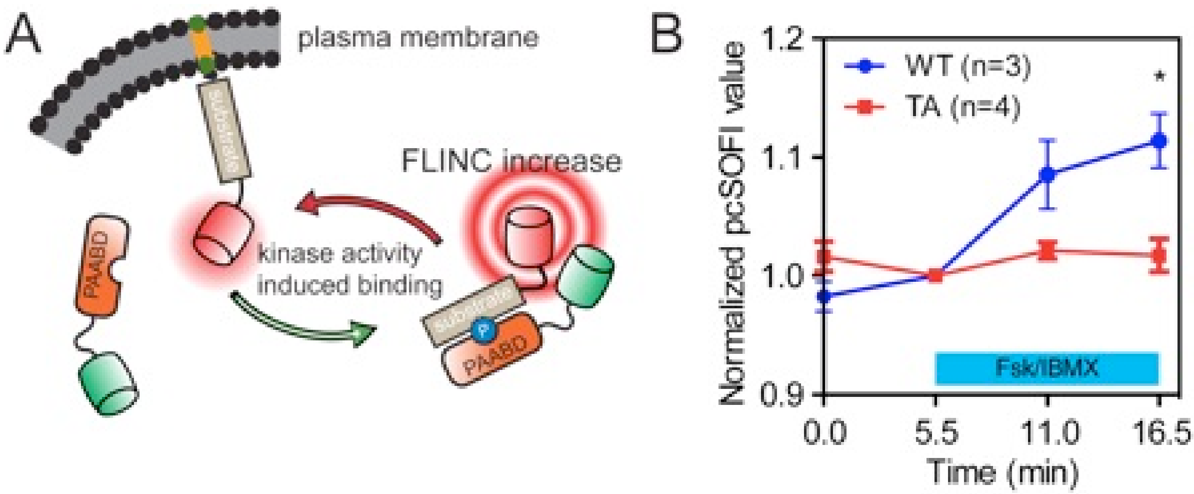

Figure 3.17 Detection of the weak protein-protein interaction between FHA1 and phospho-PKA substrate

a). Schematic of the bi-molecular version of FLINC-AKAR1. It responses to PKA stimulation at the membrane by detecting the binding of phospho-substrate and FHA1, a weak protein-protein interaction (kD ~ 0.5 μM). b). 11 min after Fsk/IBMX stimulation the wild-type (WT, n=3) biosensor shows significant response compare to the non-phosphorylatable mutant (TA, n=4). Pair-wise t-test result *: $p<0.05$; center line and whiskers mark mean and s.e.m. values, respectively.

Discussion

The nanometer sensitivity of FLINC enabled us to emulate the powerful molecular ruler FRET[40, 41] and develop new biosensors for kinase activities and PPI. Although the spatial resolution is not as high as BiFC-based superresolution methods[14–16], the fact that FLINC does not require complementation and fluorophore maturation allows us to achieve reversibility and fast response in the biosensors for investigating dynamic signaling activities in live cells. FLINC-based biosensors may be created and optimized in a fashion similar to their FRET-based counterparts. We note that a FLINC biosensor utilizing the original, compact molecular switch in AKAR2[24] did not give a significant signal upon PKA activation, demonstrating that the linker in AKARev is necessary to maximize the dynamic range of a FLINC biosensor. In addition to intermolecular distance, the FP orientation within a biosensor will be a crucial consideration in future designs. Although FLINC is currently limited to Dronpa and TagRFP-T, future studies will test other fluorescent proteins mutants for their applicability. As in FRET-based biosensor, monomerized fluorescent proteins are preferable, although in our case we have not observed issues arising from dimerization of TagRFP-T[42].

While we have demonstrated a relationship between pcSOFI value and FP proximity, at this time, pcSOFI value cannot be used to directly infer molecular distance. The absolute pcSOFI values depend on biosensor expression and the optical setup (especially camera gain and excitation intensity). However, our normalization scheme largely removes the expression dependence. Therefore, normalized pcSOFI values can be compared across experiments so long as the imaging parameters remain identical. The current temporal resolution may fall short for tracking rapid changes. However, we note that pcSOFI calculations can converge to a high signal-to-noise[43] very quickly. Specifically, we utilize only 4 s within a 30 s interval to collect data. The temporal resolution will thus improve as more sensitive and faster camera becomes available. In principle, as long as fluctuations can be observed, many types of illumination can be used to monitor FLINC, including epi-fluorescence and z-sectioning methods such as lattice light-sheet.

Under the conditions described here and previously[11], diffusion does not affect the accuracy and temporal/spatial resolution of pcSOFI and its quantification of FLINC. This is because fluorophore diffusion over the total duration of pcSOFI measurement does not lead to distortions as long as the fluorophore motion within a single exposure (35 ms) is sufficiently small. Over the imaging time, we can in fact sample the local environment more thoroughly by virtue of biosensor diffusion. In our experiments, we estimated that biosensor diffusion is within a single pixel during a single exposure; simulations using published diffusion coefficients did not reveal distortions. However, depending on the local access and sensitivity to phosphatases that resets kinase biosensors, biosensor diffusion could potentially lower the spatial resolution of the kinase activity map. In this case, while the PKA activity microdomains resolved will still accurately reflect the environment experienced by any endogenous substrate, there would be a slight overestimate of the size of PKA activation zone. There is no evidence that the above issue was significant in our experiments, however, since the sizes of microdomains measured by the both superresolution methods STORM and FLINC were in good agreement.

To our knowledge, this study represents the first demonstration of superresolution imaging of dynamic enzymatic activities such as protein kinase activities in living cells. PKA substrates are known to be more rapidly phosphorylated when localized to AKAP complexes[44], consistent with high PKA activity in the vicinity of AKAP-assembled signalosomes. We can now visualize the activity zone of these nanomachines, which are shown to be larger than the intrinsic flexibility of the PKA holoenzyme complex[45]. The significant self-clustering in AKAP79 and co-clustering of AKAP79 and phospho-PKA substrate signals suggest that the clustering of AKAP complexes, and hence an increased effective concentration of PKA regulatory subunits, may serve as an efficient means to re-capture dissociated C subunit and maintain PKA activity compartmentalization. Interestingly, 24% of total AKAP79 were orphaned and not clustered with phospho-PKA substrate. This and other data suggest that AKAPs may maintain microdomains with varying PKA activity levels, evolving dynamically based on the associated regulatory partners such as adenylyl cyclases, phosphodiesterases, kinases, and phosphatases[46]. As PKA represents a classical example of compartmentalized signaling, other biochemical activities may be under similarly precise spatiotemporal regulation. These spatial details and their functional roles could be illuminated with this new class of FLINC biosensors.

Methods

Plasmid and construct generation

All mammalian constructs were cloned using the pcDNA3.0 vector with a modified multiple cloning site. All E. coli constructs were cloned using the pRSET-B vector. Plasmids were generated through typical molecular cloning methods using a combination of polymerase chain reaction (PCR) and restriction enzyme cloning. PCR was always performed using the Phusion polymerase (New England BioLabs) unless noted. Cloning and subcloning were performed using E. coli DH5α strain.

Mutagenesis (error-prone PCR and site-directed)

All site-directed mutagenesis experiments were performed following a published protocol[47] using the E. coli JM109 strain. The randomized screens at N102 of Dronpa and D159 of TagRFP-T were both performed on a wild-type tandem DpTT template using fully degenerate primers (NNN). Error-prone PCR was performed using Taq polymerase and an in-house dNTP mixture. Eight rounds of consecutive PCR were performed (on Dronpa only) using a reverse primer containing the 8-amino acid linker at the 3’ end. This ensured that the linker was not subject to mutation. The mutation rate was approximated through sequencing, and the 3rd-to-5th-round PCR products (approximately < 2% point mutation rate) were selected for further cloning. These mutant Dronpa fragments were ligated to a linearized pRSET-B plasmid containing wild-type TagRFP-T using the sites BamHI/KpnI. All of the ligate was transformed into JM109 cells and plated onto LB-Amp agar. The candidate mutants were then screened on the basis of colony fluorescence. Once a candidate was chosen, its fluorescence intensity was confirmed by averaging the fluorescence of many colonies over a larger area on the LB-Amp agar plate.

Mutant screening

Expression of TagRFP-T causes an intense salmon/pink color due to the chromophore absorption. The tandem DpTT construct showed a faint but visible color. During error-prone or site-directed mutagenesis screening, we rejected any mutant that did not display this color, thereby excluding badly folded mutants and those containing premature stop codons and frame shifts. To quantify the effects of the mutations on mutant DpTT constructs, E. coli (JM109) expressing the mutants were streaked onto LB-Amp agar plates. The mean intensity of each mutant in the GFP or RFP channel was measured using the same exposure settings on an in-house fluorescence imager, illuminated by a broad-spectrum lamp source (MAX-303, Asahi Spectra) and monitored by a Thorlabs USB digital camera mounted behind a Thorlabs emission filter wheel (maxima/bandwidth in nm; CFP: 430/40; GFP: 535/40; RFP: 630/75). For comparison, each plate was streaked with DpTT as well as TagRFP-T colonies as normalizing controls. The images were analyzed using ImageJ (v. 1.47g). The site-directed, randomized screen at N102 of Dronpa was carried out following the same criteria outlined above. Only brightly fluorescent colonies (in both GFP/RFP channels) were sequenced.

Cell culture, transfection, and pretreatment

The HeLa and HEK293 cells utilized for these experiments were between passages 20–65. Cells were maintained in DMEM growth media supplemented with 10% FBS and 1% penicillin/streptomycin. CHO cells (passage 8–22) stably expressing α4 integrin were maintained in DMEM F12 medium with 10% FBS and 1% penicillin/streptomycin. All cells were transfected at an approximate confluency of 70% using Lipofectamine 2000 and incubated for 24 hours before imaging. All cells were imaged in HBSS buffer at room temperature. To achieve AKAP-PKA RII disruption, HeLa cells were incubated with 5 μM of the synthetic disruptor peptide STAD-2 (or its scrambled control) in DMEM growth media for 6 hours at 37°C and 5% CO2. Immediately prior to imaging, the HBSS imaging buffer was supplemented with the appropriate peptide at 5 μM. For migration studies, CHO cells were plated on cover slips coated overnight with 10 μg/mL human fibronectin (in DPBS). Cells were grown to a monolayer and wounded using a 200-μL pipette tip, then washed and incubated in HBSS buffer for 1 hour prior to imaging to induce migration.

Epifluorescence imaging

All epifluorescence imaging was performed on a Zeiss Axiovert 200M Microscope equipped with a xenon lamp and a cooled CCD, under a 40X oil immersion objective. FRET microscopy of GFP/RFP biosensors such as FLINC-AKAR1 was performed using the following excitation/emission filter combinations (maxima/bandwidths in nm): GFP – EX480/30, EM535/45; RFP – EX568/55, EM653/95; FRET: EX480/30, EM653/95. All epifluorescence experiments were subsequently analyzed using the MetaFluor software.

Total Internal Reflection Fluorescence (TIRF) imaging

All pcSOFI TIRF imaging was performed on either a Nikon Eclipse Ti microscope equipped with a Photometric Evolve 512 EMCCD, a Melles Griot argon laser (GFP excitation: 488 nm), and a Coherent Sapphire solid-state laser (RFP excitation: 561 nm) or the very similar Nikon N-STORM/TIRF microscope equipped with an Andor IXON3 Ultra DU897 electron-multiplying CCD camera. Cell were always imaged under a 100X oil immersion objective (NA 1.49) without further magnification. The TIRF condition was created using a commercial TIRF mirror setup from Nikon and controlled electronically through the imaging software (Nikon NIS-Elements v3.22.00). All TIRF imaging was performed with electronic focus drift correction. All TIRF images or time-lapse series were captured in 16-bit without binning at 35-ms exposure. For the FLINC dataset, we estimate that the 561 nm (RFP) laser intensity at the sample is 24 W/cm^2. The multiplier gain and laser power were kept consistent across all FLINC experiments involving wild-type Dronpa (DpTT, FLINC-AKAR1, FLINC-EKAR1, FLINC-AKAR1-TA, FLINC-EKAR1-TA, and FKBP-Dronpa/FRB-TagRFP-T-CAAX) reported in this article. However, since mutant and control constructs displayed disparate intensities, multiplier-gain and laser power were varied in order to obtain proper exposure. We performed laser and multiplier gain calibration, and found both to be linear. Therefore, the data presented for mean intensity comparison between wild-type DpTT, mutant DpTT, and controls (Figure 3.2b,d,e) were normalized to a gain of 1 and laser power of 100% by applying the appropriate correction factor. Skewness calculations were performed using home-built Matlab software, and pcSOFI calculation and normalization were performed using the Localizer software.[48] Unless otherwise noted, the interval between frames was 35 ms (~28.6 Hz).

Statistical Methods

All statistical significance was tested using Welch's t-test (two-sided, 95% confidence interval). All error bars mark the values of the standard error of the mean (s.e.m.). For pcSOFI and STORM measurements, single-cell responses were summarized from at least two separate experiments, each with multiple cells, over at least two passages. In the case of migrating CHO cells, cells in both wild-type and TA groups were excluded if their migration direction could not be unambiguously established.

Size-exclusion chromatography (SEC)

All SEC experiments were performed on a GE ÄKTA protein purification system using a Superdex 200 column at a flow rate of 0.2 mL/min. Affinity-purified Dronpa and TagRFP-T protein stock solutions were first further purified individually using SEC. The pure fractions of each FP were then pooled, mixed at a 1:1 molar ratio, and concentrated to a total protein concentration of approximately 120 µM; the stoichiometry was verified at 1.00:1 using absorption spectroscopy followed by spectral deconvolution. A total of 150 µL of the mixed stock solution was subsequently examined with the same SEC parameters to resolve any additional oligomeric states present in the concentrated mixture (Figure 3.3a). Collected fractions were subjected to absorption spectroscopy and spectral deconvolution in order to determine the concentration of Dronpa and TagRFP-T in each. A peak at approximately 92 kDa that was not observed in the chromatographs of the individual FPs was found to contain a stoichiometric ratio of approximately 2.5 TagRFP-T molecules to 1 Dronpa. It is known that TagRFP-T forms dimers at high concentrations. Since Dronpa and TagRFP-T are each 30kDa, both size and stoichiometry verified the presence of a trimeric FP complex between a TagRFP-T dimer and a Dronpa monomer.

Analytical ultracentrifugation (AUC)

All sedimentation velocity (SV) experiments were conducted in a Beckman-Coulter Optima XL-A analytical ultracentrifuge at 50,000 rpm and 20°C. A set of initial SV experiments were performed using purified TagRFP-T, Dronpa, and their mixture at the concentrations of 12, 10, and 12/10 μM, respectively, which found that the association constant was weaker than 104 M−1. Three further SV experiments were then collected using highly concentrated proteins: (1) TagRFP-T alone at 171 μM detected at 595 nm; (2) Dronpa alone at 172 μM detected at 435 nm; and (3) a mixture of TagRFP-T (171 μM) and Dronpa (172 μM) detected at 595 nm. The individual Dronpa and TagRFP-T samples were fit to normalized g(s*) distributions using DCDT+ (version 2.4.1) with apparent weight average sedimentation coefficients equal to 2.4 S and 3.7 S, respectively. The sedimentation coefficient distribution function for the mixed sample was poorly described by a sum of non-interacting species, indicating an association between the two components. However, the sedimentation coefficient for the Dronpa+TagRFP-T complex could not be accurately determined because the population of the species was low. To obtain an estimate of the association constant, we further analyzed the data using

SedAnal (version 6.01.6926), which allows direct boundary fitting using mass action equations. The above sedimentation coefficients were used in an initial fitting attempt to a simple A+B ↔ C association model, which converged poorly. We reasoned that the sedimentation coefficients may be depressed in the mixed sample due to molecular crowding and therefore set them to values 10% lower than their original estimates for subsequent fitting using a range of sedimentation coefficients for the complex to obtain estimates of the association constant. A typical fit is shown in Figure 3.3b. The calculated maximum sedimentation coefficient for a spherical shape of the Dronpa + TagRFP-T complex is 5.95 Sv and was found using the following equation:

$$sMax = \frac{M(1 - \bar{v}\rho)}{N_A 6\pi\eta(\frac{3M(\overline{v +}\, \delta_w \bar{v})}{4N_A}}$$

Any asymmetry in the complex shape would lead to lower sedimentation coefficients. Because the complex sedimentation coefficient could not be experimentally determined, we fit the data by fixing it at several different values to obtain the subsequent association constant. These are shown in Table 3.1, in which the Ka varies between 1090 M−1 and 6280 M−1 for reasonable values of the complex sedimentation coefficient. Using these estimates, an A + B ↔ C model yields an estimated Kd in the range of 159 µM to 917 µM.

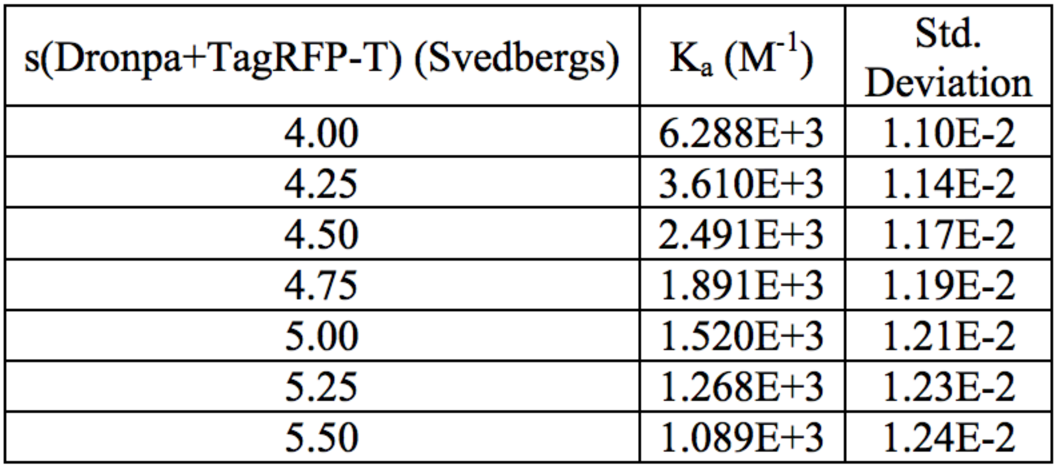

s(Dronpa+TagRFP-T) (Svedbergs)	K_a (M^{-1})	Std. Deviation
4.00	6.288E+3	1.10E-2
4.25	3.610E+3	1.14E-2
4.50	2.491E+3	1.17E-2
4.75	1.891E+3	1.19E-2
5.00	1.520E+3	1.21E-2
5.25	1.268E+3	1.23E-2
5.50	1.089E+3	1.24E-2

Table 3.1 Analytic Ultracentrifugation of Dronpa-TagRFP-T fusion

Summary of SedAnal best fit values of the association constant obtained using estimates of the Dronpa+TagRFP-T complex sedimentation coefficient. This range of Ka values provides limits for the association constant between Dronpa and TagRFP-T.

Single Molecule Fluorescence Characterization

For single-molecule imaging, 30-mm round cover glasses (No. 1, VWR Corporate Headquarters, PA) were sequentially cleaned by ultrasonication in 1% Alconox (Alconox Inc, NY), water, ethanol and 1M KOH. PEG and Biotin-PEG (Laysan Bio) were coated on the clean cover glass according to a published protocol[49]. A Hybriwell (Secure-Seal, Grace) is pasted on the cover glass and sealed by epoxy. The assembled chamber was incubated with A) 0.01mg/ml neutravidin B) 1mM Biotin-NTA (Biotium) in PBS for 10min sequentially. Each step was followed by 1X PBS wash for twice. His-tagged purified TagRFP-T or DpTT was diluted in 1X Tris buffer with different salt (300–3000mM NaCl) concentration to a final protein concentration about 100 pM. Immobilization was done by incubating the final TagRFP-T or DpTT solution in the chamber for 10 min and wash by the same buffer once. Single molecule fluorescence imaging was performed in the buffer without protein on an Olympus IX-71 inverted microscope under a 60X, 1.45 NA TIRFM objective. A home-built optical system with 561 nm solid-state excitation laser (Sapphire, Coherent, Santa Clara, CA) and an EMCCD camera (iXon DU897E, Andor Technology, Belfast, Northern Ireland) was used to examine the samples (emission: ZET488/561m, Chroma Technology, Rockingham, VT). An iris aperture was used to restrict the laser spot size to 150×150 pixels (~700 μm^2). The laser power density was attenuated by a ND filter (NE10A, Thorlabs, NJ) to 12 W/cm^2. Single-molecule image streams were collected with maximum EM Gain (300) in 16-ms integration time for 2000 frames. Molecules were detected by local maximum searching using ImageJ plugin ThunderSTORM[50]. Aggregated molecules were filtered by removing high intensity spots (>3sigma). The spots closer than 1 pixel (267nm) were discarded to guarantee signal is from single molecules. Signal of the spots in every single frame was integrated from a 3×3 ROI centered at the ThunderSTORM detections. Background was subtracted by the whole frame averaged intensity. The real photon count is obtained per instruction from camera manufacturer (Andor). The autocorrelation curves were calculated from the intensity trace of individual spots in Matlab (xcorr function) and normalize to the autocorrelation value at time lag of zero. All autocorrelation curves were averaged to a single autocorrelation function (ACF) for each condition.

TagRFP-T or DpTT solution in the chamber for 10 min and wash by the same buffer once. Single molecule fluorescence imaging was performed in the buffer without protein on an Olympus IX-71 inverted microscope under a 60X, 1.45 NA TIRFM objective. A home-built optical system with 561 nm solid-state excitation laser (Sapphire, Coherent, Santa Clara, CA) and an EMCCD camera (iXon DU897E, Andor Technology, Belfast, Northern Ireland) was used to examine the samples (emission: ZET488/561m, Chroma Technology, Rockingham, VT). An iris aperture was used to restrict the laser spot size to 150×150 pixels (~700 μm^2). The laser power density was attenuated by a ND filter (NE10A, Thorlabs, NJ) to 12 W/cm^2. Single-molecule image streams were collected with maximum EM Gain (300) in 16-ms integration time for 2000 frames. Molecules were detected by local maximum searching using ImageJ plugin ThunderSTORM[50]. Aggregated molecules were filtered by removing high intensity spots (>3sigma). The spots closer than 1 pixel (267nm) were discarded to guarantee signal is from single molecules. Signal of the spots in every single frame was integrated from a 3×3 ROI centered at the ThunderSTORM detections. Background was subtracted by the whole frame averaged intensity. The real photon count is obtained per instruction from camera manufacturer (Andor). The autocorrelation curves were calculated from the intensity trace of individual spots in Matlab (xcorr function) and normalize to the autocorrelation value at time lag of zero. All autocorrelation curves were averaged to a single autocorrelation function (ACF) for each condition.

Photophysical Characterizations

For dark-state conversion (DSC) measurements, HeLa cell expressing nuclear-localized TagRFP-T/DpTT were illuminated with a 561 nm solid-state diode-pumped laser (Genesis MX, Coherent) through a custom-built inverted microscope at an intensity of ~ 8–10 kW/cm2. A 629/56 nm band-pass filter (Semrock) was used to remove excitation from emission. Epi-fluorescence from the cells was collected using a PMT (Hamamatsu Photonics) and subsequently the PMT photo-current was converted to voltage using a custom-built trans-impedance operational amplifier for better signal to noise ratio. Fluorescence signal was digitized using a data acquisition card (DAQ, National Instruments) at a rate of 1 MHz. Pulsed illumination was achieved using an acousto-optic modulator (AOM, Gooch & Housego, 35210-BR). Cells expressing FPs were bleached continuously for 0.1 s and fluorescence traces were collected for further analysis. The raw fluorescence data were background-corrected and spline-fitted for smoothing. The fluorescence traces had three distinct features: a rapid decay up to 100 μs time-scale, a flat region in 100–1000 μs region, followed by a slow decay in ms time-scale. Hence, the fluorescence traces were fitted with a 3-exponetial function using equi-distant time-points in log scale. The fastest time-constants and its corresponding amplitude from the fitting results were considered as DSC time-constants and percent DSC respectively[51]. To measure the ground-state recovery (GSR) time-constants, cells expressing nuclear-localized TagRFP-T/DpTT were excited with pulse-trains having 2 ms exposure time and varying inter-pulse delays (dark time) ranging from 5 µs to 10 ms. Fluorescence traces collected using the pulsed excitations were used to compute percent recoveries using the following equation without further processing: $PR=(FR-FB)/(FL-FB)\times 100$, where PR is the percent recovery. FL, FB, FR are the fluorescence intensities at initial point, after 2 ms exposure, and after the recovery between pulses, respectively. To measure the GSR time-constants, FPs were excited with pulse-trains having 2 ms exposure time and varying inter-pulse delays (dark time) ranging from 10 µs to 50 ms. A home-built software (Matlab) was used to compute percent recoveries of the fluorescence and finally percent recovery vs. dark time plots were fitted with single exponential to extract GSR time-constants[52].

Excited state lifetimes of purified TagRFP-T and fluorescent DpTT were measured on a Fluro Time 100 commercial TCSPC system (PicoQuant) using 560 nm laser excitation with a repetition rate of 2.5 MHz. Lifetime measurements were performed using purified proteins in PBS buffer (pH=7.4) at appropriate dilutions. Figure3.4D displays the fluorescence decays of the proteins and instrument response function (IRF). The fluorescence traces of the FPs were fitted with iterative reconvolution with a bi-exponential function and using measured IRF of the system. Intensity-weighted average excited state lifetime of TagRFP-T and DpTT were 2.45 ns and 2.40 ns, respectively (Table 3.2).

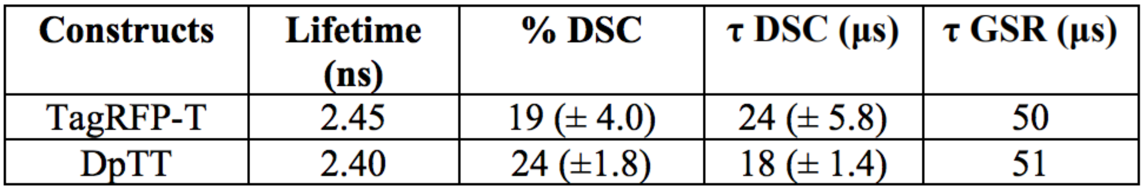

Constructs	Lifetime (ns)	% DSC	τ DSC (μs)	τ GSR (μs)
TagRFP-T	2.45	19 (± 4.0)	24 (± 5.8)	50
DpTT	2.40	24 (±1.8)	18 (± 1.4)	51

Table 3.2 Summary of photophysical measurements

Average values for fluorescence lifetime, percentage of dark-state conversion possible in the sample (% DSC), time constant of DSC (τDSC), and time constant of GSR (τGSR) are reported. See also Figure 3.4

Direct Stochastic Optical Reconstruction (dSTORM) Microscopy

The primary antibodies used in these experiments were mouse anti-AKAP79 (BD Biosciences, 610314) and rabbit anti-Phospho-(Ser/Thr) PKA Substrate ("pPKAsub", Cell Signaling, 9621). The AKAP79 antibody was used 1:50 dilution; the anti-Phospho-(Ser/Thr) PKA substrate antibody was used at 1:200 after a dilution series test was conducted. The secondary antibodies used in these experiments were AlexaFluor® 568 and AlexaFluor® 647 (Life Technologies) at dilutions of 1:2000 and 1:1000, respectively. Saponin from Quillaja Bark, sodium borohydride, glutaraldehyde (GA), and normal goat serum (NGS) were from Sigma-Aldrich; paraformaldehyde (PFA) from Electron Microscopy Sciences; glycine from Fisher Scientific; bovine serum albumin from Roche Diagnostics. Cells plated in 35mm dishes were washed three times in HBSS and appropriately pre-treated (or no pre-treatment) for 15 min. at 37° C, then washed with PBS before fixation using 4% PFA, 0.2% GA PBS for 10 minutes at room temperature. All subsequent steps were performed on a shaker; saponin was always used at 0.0005%; all solutions were at pH 7.4. Cells were quickly rinsed in PBS after fixation and quenched with freshly made 0.1% NaBH4 ice-cold PBS. Following 3X PBS washes of 5 min. each, cells were permeabilized and blocked for 1 hour at room temperature in 10% NGS + saponin PBS, followed by 3X saponin PBS washes of 5 min. each. Primary antibodies were made to working concentrations in 1% BSA + saponin PBS. Cells were incubated with primary overnight at 4° C, followed by 3X saponin PBS washes of 5 min. each. Secondary antibodies were made working concentrations in 1% BSA + saponin PBS. Cells were incubated with secondary antibodies for 1 hour at room temperature in the dark. All remaining steps were performed in the dark. Cells were washed 3X saponin

PBS for 5 min. each followed by washing 3X PBS for 5 min. each. All samples were post-fixed in 4% PFA PBS for 10 min. at room temperature, and quickly rinsed in PBS and quenched with 3X 100mM glycine PBS for 5 min. each. The cells were washed 3X PBS for 5 min. each and stored in PBS at 4°C in the dark until imaging within 24 hours. All STORM imaging was performed on a Nikon Ti microscope under total-internal reflection (TIR) condition, using a 100X/1.49 NA Apo TIRF objective. Images were collected within a 256 × 256 pixel ROI on an Andor IXON3 Ultra DU897 electron-multiplying CCD camera using the multicolor continuous mode setting in the Nikon Elements software. Power of the 568 nm and 647 nm excitation (as well as activating 405 nm excitation) was adjusted to enable stochastic blinking behavior within the ROI. The images were reconstructed and drift-corrected using the Nikon N-STORM software.

pcSOFI analysis of FLINC data

Using the Localizer software[48], we performed second- and third-order, cross-cumulant SOFI calculation to process each time series and generate a pcSOFI image. Briefly, fluorescence intensity fluctuation data from each local pairs of pixels were utilized to calculate the cross-cumulants (or "pcSOFI values"), which quantifies the degree or strength of fluctuation. The nature of the pixel pairing allows the algorithm to refine the location of each scalar pcSOFI value at a resolution higher than the original image pixel density. Simplistically, the use of n-th order cumulant calculation allows n-fold improvement in resolution. Our calculation accounts for photobleaching. In accordance with the analytical derivation for the pcSOFI value (section "Analytical expression for normalized pcSOFI analysis" of this document), the pcSOFI images were normalized pixel-wise by the averaged intensity to address biosensor distribution. Each pcSOFI image was then deconvolved using Localizer over 5 iterations assuming the standard deviation of the PSF is 1.0 pixels. After pcSOFI analysis, the images were exported into 32-bit floating point TIFF files and analyzed using ImageJ (v. 1.47g).

Analytical expression for normalized pcSOFI analysis

The uneven distribution of the biosensor over the cell complicates the evaluation of the biosensor response (Figure 3.7a,c). We addressed this by normalizing the pcSOFI images pixel-wise, dividing the pcSOFI value by the time-averaged intensity using a linearly interpolated averaged intensity image. To derive an expression for the pcSOFI signal, we assumed that FLINC is well modeled by fluorophores that continuously and reversibly cycle between two different states: a non-fluorescent (dark) state and a fluorescent (bright) state with a molecular brightness of ε (expressed in, for instance, photons emitted per second). We further assume that the bright state converts to the dark state at a rate constant k_{BD} and recovers with rate constant k_{DB}. The resulting 2nd order pcSOFI signal for time lag τ is given by:

$$G(\tau) = N\varepsilon^2 \frac{k_{DB}k_{BD}}{(k_{DB} + k_{BD})^2} e^{-(k_{DB}+ k_{BD})\tau}$$

where *N* is the number of molecules contributing to the pixel under consideration. This reveals that the pcSOFI signal is sensitive to both the fluctuation dynamics and the local concentration. Normalizing the pcSOFI value by the time-averaged fluorescence intensity, $\langle I \rangle$, results in the following expression for normalized pcSOFI value:

$$\frac{G(\tau)}{\langle I \rangle} = \varepsilon \frac{k_{BD}}{k_{DB} + k_{BD}} e^{-(k_{DB}+ k_{BD})\tau}$$

Therefore, the normalized pcSOFI value remains sensitive to emission fluctuations but is independent of the local concentration. If we further consider the fluctuating fluorescence signal to be a mixture of two species (e.g. the same biosensor in high and low FLINC states), we can demonstrate that normalization by intensity *I* gives a similar result even in this more general case. We simplify the chromophore rate kinetic terms above using:

$$f^D = \frac{k_{BD}}{k_{DB} + k_{BD}} e^{-(k_{DB} + k_{BD})\tau}, f^B = \frac{k_{DB}}{k_{DB} + k_{BD}} e^{-(k_{DB} + k_{BD})\tau},$$

and arrive at an analogous expression for the normalized pcSOFI value:

$$\frac{G(\tau)}{\langle I \rangle} = \frac{N_1 \varepsilon_1^2 f_1^D f_1^B + N_2 \varepsilon_2^2 f_2^D f_2^B}{N_1 \varepsilon_1 \, f_1^B + N_2 \varepsilon_2 \, f_2^B},$$

where the subscripts 1 and 2 designate the species in mixture. Since in practice, these two species are not independent, we can express them as fractions of the total number of biosensor N_t:

$$\frac{G(\tau)}{\langle I \rangle} = \frac{\alpha N_t \varepsilon_1^2 f_1^D f_1^B + (1-\alpha) N_t \varepsilon_2^2 f_2^D f_2^B}{\alpha N_t \varepsilon_1 \, f_1^B + (1-\alpha) N_t \varepsilon_2 \, f_2^B} = \frac{\alpha \varepsilon_1^2 f_1^D f_1^B + (1-\alpha) \varepsilon_2^2 f_2^D f_2^B}{\alpha \varepsilon_1 \, f_1^B + (1-\alpha) \varepsilon_2 \, f_2^B}$$

where α is the fraction of high-state FLINC biosensors. Again, the normalized pcSOFI value is clearly independent of the total number of molecules N_t. Moreover, normalized pcSOFI remains a function of the high FLINC fraction (α). Therefore, under both a simplified and general consideration, our analytical scheme can effectively remove labeling density dependence, allowing us to measure the biochemical activity of interest. Since the average intensity can only be estimated from the diffraction-limited data, normalized pcSOFI values are slightly less optimal than theoretical predictions. However, our resolution analyses show that the resulting resolution gain compares well with theory. We demonstrate the capability of this normalization scheme using plasma membrane targeted Dronpa. Without normalization, Dronpa concentrations were clearly different at local regions of the membrane; such disparities were abolished in the normalized pcSOFI image; this is supported by the corresponding profile plots showing the effect of normalization within a selected region (averaged in the y-axis) (Figure 3.7e, inset). The normalized pcSOFI values are used throughout the paper (e.g., Figure 3.7b,d).

Signal-to-noise ratio analysis

We conducted a series of simulations designed to examine the sensitivity of the sensor response to the signal-to-noise ratio (SNR) of the input time-series data. Briefly, we simulated a movie consisting of 848 images, each of size 35x35 pixels, containing approximately 250 molecules. This simulation includes full modeling of the blinking of the individual emitters and also the photon counting noise and electron multiplication noise. We define SNR as:

$$SNR_i = \frac{\mu_i}{\sigma_i}$$

where μ_i and σ_i are the average and standard deviation of the signal detected by pixel i over the entire time series. At each condition, we simulated the difference in normalized pcSOFI signal between ON/OFF states of the biosensor and repeated with different emitter brightness to simulate imaging under various SNR. Each set of conditions was repeated nine times to examine the error magnitude. The observed change in normalized pcSOFI value was essentially constant starting from an SNR (from the fluorescence fluctuation) of 2, beyond which the contribution of noise is very small. Analysis of an experimental dataset from a CHO cell found an SNR of 2.8, suggesting that noise in the fluorescence fluctuation time-series has a negligible effect on the response of the FLINC-based biosensors.

Separately, we utilized a published method of Delete-1 jackknife resampling[53] to estimate the signal-to-noise ratio within the pcSOFI image. In this method, the sequence of N fluorescent images used to generate a pcSOFI image was used to generate N distinct image sets in which a single image in the original set was omitted. The pcSOFI calculation was then performed using each of these resampled image stacks to yield N distinct estimations for the cumulant at each pixel. The uncertainty of the pcSOFI value at each pixel was then estimated in order to calculate the SNR, which serves as an estimation of the precision of the pcSOFI value at each pixel. This is shown in Figure 3.5. We determined that the SNR of the pcSOFI value is very high, denoting a high accuracy in activity measurement.

Resolution analysis

The resolution achieved in FLINC imaging was estimated using two previously reported methods. Firstly, resolution was determined by the measurement of a feature of known size, which then allowed an estimate of the resolution using Gaussian fitting. FLINC-AKAR1 was targeted to actin filaments in live HeLa cells using the Lifeact targeting motif[54]. Profiles of actin filaments from normalized pcSOFI images were fitted with Gaussian models (Matlab 2014a, “fit” function), and the averaged full-width-half-maximum (FWHM) across multiple filaments is reported as the resolution. The average Gaussian FWHM was 179 ± 6 nm (n = 7) for 2nd order images and 116 ± 6 nm (n = 7) for 3rd order images (Figure3.9a,b). Secondly, the maximum achieved resolution was examined using two converging features in the pcSOFI images. Profile lines were drawn through the junction of two clearly visible and converging filopodia. The maximum theoretical resolution for a given order of cumulant analysis was reached when only two pixels separate the filopodia, and the resolution was reported as twice the pixel size. Therefore, 2nd order analysis allowed the resolution of features separated by 160 nm; 3rd order analysis resolved features separated by 107 nm (Figure 3.9c-e). 3D surface illustrations were plotted using Matlab (2014a).

Puncta analysis for FLINC imaging

To examine the characteristics of the high activity puncta observed in some of the conditions, we segmented the pcSOFI images and collected statistics on the puncta. A 128x128 region of interest (ROI; 104 μm^2) was selected for each cell from deconvolved normalized pcSOFI images. These ROIs were chosen to include the basal membrane and avoid filopodia extensions. The ROIs were then thresholded using ImageJ (v. 1.47g, Intermodes method) and analyzed automatically by the built-in Particle Analysis function. The number of puncta and approximate diameter of the particle for a given condition were summarized and reported in the text. We further examined the stimulated change in the fractional area occupied by the puncta in each ROI across many constructs and pretreatment. For this second type of analysis, the total area occupied by the puncta at each time point, as identified by the above analysis, was summed and normalized by the total ROI area (128x128). The fractional area for each time point was then normalized by that of the time point immediately before chemical stimulation, and the tabulated result across many cells for each construct/pretreatment/stimulation combination was then reported in Figs. 2G and 3E. Puncta analysis on the filopodia and basal membrane regions of migrating CHO cells was performed in a similar fashion on the entire cell by categorizing individual punctum into different regions based on cell morphology and distance from front-edge. While the migrating cells displayed a large range of pcSOFI values, threshold was set to capture only the top 2%, most highly active pixels within each cell via image histogram for comparison. Consistent with the observed PKA activity gradient, highly-active puncta were seldom found toward the back of the cell. The analyzed puncta PKA activities were reported as an average in each category for each cell (n = 9), for which Figure 3.14e is representative.

Estimating the diffusion of probes due to STAD-2 pretreatment

To analyze the possible diffusion of the probe molecules, we made use of a version of image correlation spectroscopy[55]. Multiple datasets containing only the cell body were created by cropping the pcSOFI dataset to 100x100 regions of interest containing the full time-series in the experiment. The image correlation over this region is as follows:

$$r(\xi,\eta,\tau) = \frac{\langle \delta i(x,y,t)\delta i(x+\xi,y+\eta,t+\tau)\rangle}{\langle i\rangle^2}$$

where $\langle \dots \rangle$ denotes averaging over all *x, y,* and t. ξ,η,τ denote the selected spatial lags and temporal lag in units of pixels and frames. $\delta i(x,y,t)$ is the fluctuation in the fluorescence detected in the pixel at *(x,y,t)*, compared to the average intensity of the image at time *t*, $\delta i(x,y,t) = i(x,y,t) - \langle i\rangle_t$. For our datasets, the possible spatial shifts ξ and η are determined by the pixel size of the camera, and the possible temporal lags τ are determined by the camera exposure time. The resulting correlation function is

Gaussian-like and decreases in amplitude with increasing τ. It can be shown that the variance of the peak as a function of lag time is related to the diffusion coefficient as:

$$\sigma^2(\tau) = 2\sigma_{\mathrm{PSF}}^2 + 2D\tau$$

where σ_{PSF}^2 is the variance of the point-spread function and D is the diffusion coefficient. In our calculation, we determine the variance $\sigma^2(\tau)$ by fitting the correlation signal for each time-lag using a 2D Gaussian function. While deviations arise for longer lag times due to the decreased signal in the correlation, the resulting behaviour is approximately linear for lag times up to about 12 or more exposures. Using these fits, we found that probes in STAD-2-pretreated HeLa cells displayed a diffusion coefficient of 0.075±0.02 $\mu m^2/s$ (n=3), which is not significantly different from the diffusion coefficient of 0.097±0.005 $\mu m^2/s$ (n=5) in scramble-control-pretreated cells. The movement of a biosensor over the duration of SOFI does not pose a problem as long as the movement within a single exposure is not too large. Our exposure time is 35 ms. We estimate that the biosensor travels approximately $(0.075{\sim}0.097\mu m^2/s*35ms)^{1/2}$ = 51-58 nm between each exposure, smaller than the pixel size we employed (160 nm).

Post-processing and cluster analyses of dSTORM imaging data

The persistence of fluorescence for longer than the frame rate and the blinking of the fluorophore can result in multiple localizations from a single emitter. Therefore, prior to analysis, we first corrected for over-counting by grouping the localizations under the criterion that localizations within a 100 nm radius and a given dark time (t_d) period could be from the same molecule. We used a published method for determining the appropriate dark times for each fluorophore.[56,57] The number of distinct molecules identified was determined for different values of the dark time. These data were then fit to the following equation, describing two timescales for blinking:

$$N(t_d) = N(1 + n_{blink,1}e^{\frac{(1-t_d)}{t_{off,1}}} + n_{blink,2}e^{\frac{(1-t_d)}{t_{off,1}}})$$

Here, $N(t_d)$ is the number of molecules identified for a given dark time, N is the real number of fluorescent molecules, $n_{blink,1}$ and $n_{blink,2}$ are the number of dark state conversions occurring with average dark state lifetimes $t_{off,1}$ and $t_{off,1}$, respectively. For Alexa568, the fit showed that 5.8 blinks per molecule occurred for dark states with a lifetime of 1.3 frames (20ms), and 5.4 blinks per molecule occurred for dark states with a lifetime of 22.4 frames (336ms) (Figure 3.11a). For Alexa647, the fit showed that 1.6 blinks per molecule occurred for dark states with a lifetime of 70 frames (1.1s), and 1.7 blinks per molecule occurred for dark states with a timescale of 3.1 frames (46ms) (Figure 3.11b). Values of the dark time were chosen to be double the lifetime of the longer blinking timescale, or 140 frames for Alexa647 and 45 frames for Alexa568.

We employed a variety of complementary clustering/correlation analyses. Mean shift clustering[58] of the STORM data was performed in MATLAB as was described previously[59]. Briefly, the multivariate kernel density function, f(x), is used to estimate the point density of multidimensional data weighted by a spatial kernel, K(x):

$$f(x) = \frac{1}{nh^d}\sum_{i=1}^{n} K\left(\frac{x - x_i}{h}\right)$$

where n is the number of data points, h is the bandwidth of the kernel, d is the dimension (here, d=2). For this study we used a Gaussian kernel and truncated the kernel at a $(x - x_i)/h > 2$. This kernel density function is used to estimate the density gradient to allow iterative progression towards local density maximum. Thus, a random point in the

STORM dataset is selected and the estimated density gradient is used to iteratively move the estimated mean towards the local density maximum, or centroid, until it converges. Then clusters are defined by grouping points together that contribute to this local maximum. We disregarded clusters with 10 or fewer localizations. See Figure 3.11c1,c2 for representative results of the clustering on AKAP79 and pPKAsub localizations, and the nearest-neighbor pair display (Figure 3.11c3). The convex hull of each cluster was determined using the built-in MATLAB function *convhull*, and this area was used to calculate an approximate diameter. To analyze the association between AKAP79 and PKA activity, the nearest pPKAsub cluster centroid to each AKAP79 cluster centroid was identified based on Euclidian distance. From the pair centroid distances we could generate a histogram for each cell to characterize the spatial association compared to random (Figure 3.11c4). For the multiplexed FLINC/STORM data, an analogous histogram can be obtained by connecting each AKAP79 cluster to the nearest microdomain identified by FLINC (Figure 3.11c5). Separately, we estimated that the average experimental error in colocalization between the two color channels was 44.3 nm, as measured by the centroid distances between clusters of localizations in different color channels from many 100 nm Tetraspeck beads (Life Technologies).

To analyze the spatial scales of clustering, the Ripley's K analysis[60] was performed for 5μm x 5μm regions for r values ranging from 1 to 1000. The Ripley's K function is given by the following equation:

$$K(r) = A\sum_{j=1}^{N}\sum_{i=1}^{N}\frac{\delta_{ij}}{n^2}, \quad \delta_{ij} = \begin{cases} 1\ if\ d_{ij} < r \\ \quad else\ 0 \end{cases}$$

where A is the area of the region being analyzed, n is the total number of localizations in that area, and d_{ij} is the distance between molecules i and j. Molecules within a distance of r of the edge of the region of interest are not used in the analysis to eliminate edge effects. The Ripley's K function for a random distribution scales with the area of a circle with radius r. To create a statistic that scales linearly with R, the L function is defined as:

$$L(r) = \sqrt{\frac{K(r)}{\pi}}$$

To eliminate the dependence on r, L(r)−r is plotted, so that a random distribution will have an expected value of zero for all values of r. The peak of the L(r)−r curve represents the length scale of maximum clustering. To generate the 95% confidence interval for random clustering, Ripley's K analysis was performed on 200 simulated randomly dispersed data sets with the same number of molecules as the dataset to which it is compared. These datasets were generated by choosing uniformly distributed random numbers for x- and y-coordinates within the region of interest. The values of L(r)−r were then ranked for each value of r, and the fifth-percentile and ninety-fifth percentile values were plotted.

To study the co-clustering of AKAP79 and pPKAsub, a published method based on Getis and Franklin's local pattern analysis[61,62] was used. Here a value of L(r) is calculated for each molecule individually, according to the equation:

$$L_i(r) = \sqrt{\frac{A}{\pi}\sum_{j=1}^{N}\frac{\delta_{ij}}{n}}, \qquad \delta_{ij} = \begin{cases} 1\ if\ d_{ij} < r \\ \quad else\ 0 \end{cases}$$

To analyze self-clustering of AKAP79 (Figure 3.11d1), $L_{self,i}$ is calculated by counting the number of molecules of AKAP79 (index j) within a radius r of a molecule i of

AKAP79 and normalizing it appropriately. $L_{cross,i}$, on the other hand, is calculated by counting the number of pPKAsub molecules (index j) within a radius of r of molecule i of AKAP79 (Figure 3.11d2). This analysis was performed using a value of R of 200nm, corresponding the approximate length scale of clustering of AKAP79. Plots of L_{cross}(200) vs. L_{self}(200) were generated (Figure 3.11d3), and a threshold of L(r)=250 was used to for both L_{cross} and L_{self} to divide the plot into quadrants. This threshold was chosen because, in all regions examined, AKAP79 molecules with a L_{self} value above 250 were well-clustered, while those with an L_{self} value below 250 were not. This analysis allows for the calculation of the proportion of AKAP79 molecules that are found in clusters as well as the proportion that do or do not co-cluster with pPKAsub.

Personal Contributions

I cloned FLINC EKAR as well as performed the subsequent pcSOFI imaging with FLINC EKAR to characterize it. I also performed the jackknife resampling of the FLINC AKAR data. Furthermore, I wrote the analysis scripts and performed the spatial pattern analysis of the single and two-color STORM data, including Ripley K and the bivariate version of Getis and Franklin local pattern analysis. I wrote the parts of the manuscript corresponding to the jackknife resampling and spatial pattern analysis of STORM data, and I was involved in the editing and revision of the manuscript.

References

1. Avraham, R. & Yarden, Y. Feedback regulation of EGFR signalling: decision making by early and delayed loops. Nat. Rev. Mol. Cell Biol. 12, 104–117 (2011).
2. Ganesan, A. & Zhang, J. How cells process information: quantification of spatiotemporal signaling dynamics. Protein Sci. 21, 918–928 (2012).
3. Wong, W. & Scott, J.D. AKAP signalling complexes: focal points in space and time. Nat. Rev. Mol. Cell Biol. 5, 959–970 (2004).
4. Rizzuto, R. & Pozzan, T. Microdomains of intracellular Ca2+: molecular determinants and functional consequences. Physiol. Rev. 86, 369–408 (2006).
5. Cambi, A. & Lidke, D.S. Nanoscale membrane organization: where biochemistry meets advanced microscopy. ACS Chem. Biol. 7, 139–149 (2012).
6. Sengupta, P., van Engelenburg, S.B. & Lippincott-Schwartz, J. Superresolution imaging of biological systems using photoactivated localization microscopy. Chem. Rev. 114, 3189–3202 (2014).
7. Huang, B., Bates, M. & Zhuang, X. Super-resolution fluorescence microscopy. Annu. Rev. Biochem. 78, 993–1016 (2009).
8. Hell, S.W. Far-field optical nanoscopy. Science 316, 1153–1158 (2007).
9. Betzig, E. et al. Imaging intracellular fluorescent proteins at nanometer resolution. Science 313, 1642–1645 (2006).
10. Rust, M.J., Bates, M. & Zhuang, X. Sub-diffraction-limit imaging by stochastic optical reconstruction microscopy (STORM). Nat. Methods 3, 793–795 (2006).

11. Dedecker, P., Mo, G.C.H., Dertinger, T. & Zhang, J. Widely accessible method for superresolution fluorescence imaging of living systems. Proc. Natl. Acad. Sci. USA 109, 10909–10914 (2012).

12 Dertinger, T., Colyer, R., Iyer, G., Weiss, S. & Enderlein, J. Fast, background-free, 3D super-resolution optical fluctuation imaging (SOFI). Proc. Natl. Acad. Sci. USA 106, 22287–22292 (2009).

13. Rego, E.H. et al. Nonlinear structured-illumination microscopy with a photoswitchable protein reveals cellular structures at 50-nm resolution. Proc. Natl. Acad. Sci. USA 109, E135–E143 (2012).

14. Liu, Z. et al. Super-resolution imaging and tracking of protein-protein interactions in sub-diffraction cellular space. Nat. Commun. 5, 4443 (2014).

15. Nickerson, A., Huang, T., Lin, L.-J. & Nan, X. Photoactivated localization microscopy with bimolecular fluorescence complementation (BiFC-PALM) for nanoscale imaging of protein-protein interactions in cells. PLoS One 9, e100589 (2014).

16. Hertel, F., Mo, G.C.H., Duwé, S., Dedecker, P. & Zhang, J. RefSOFI for mapping nanoscale organization of protein-protein interactions in living cells. Cell Rep. 14, 390–400 (2016).

17. Newman, R.H., Fosbrink, M.D. & Zhang, J. Genetically encodable fluorescent biosensors for tracking signaling dynamics in living cells. Chem. Rev. 111, 3614–3666 (2011).

18. Ando, R., Mizuno, H. & Miyawaki, A. Regulated fast nucleocytoplasmic shuttling observed by reversible protein highlighting. Science 306, 1370–1373 (2004).

19.Shaner, N.C. et al. Improving the photostability of bright monomeric orange and red fluorescent proteins. Nat. Methods 5, 545–551 (2008).

20. Arai, R., Ueda, H., Kitayama, A., Kamiya, N. & Nagamune, T. Design of the linkers which effectively separate domains of a bifunctional fusion protein. Protein Eng. 14, 529–532 (2001).

21. Dickson, R.M., Cubitt, A.B., Tsien, R.Y. & Moerner, W.E. On/off blinking and switching behaviour of single molecules of green fluorescent protein. Nature 388, 355–358 (1997).

22. Bourgeois, D. & Adam, V. Reversible photoswitching in fluorescent proteins: a mechanistic view. IUBMB Life 64, 482–491 (2012).

23. Geissbuehler, S. et al. Live-cell multiplane three-dimensional super-resolution optical fluctuation imaging. Nat. Commun. 5, 5830 (2014).

24. Zhang, J., Hupfeld, C.J., Taylor, S.S., Olefsky, J.M. & Tsien, R.Y. Insulin disrupts beta-adrenergic signalling to protein kinase A in adipocytes. Nature 437, 569–573 (2005).

25. Komatsu, N. et al. Development of an optimized backbone of FRET biosensors for kinases and GTPases. Mol. Biol. Cell 22, 4647–4656 (2011).

26. Bacskai, B.J. et al. Spatially resolved dynamics of cAMP and protein kinase A subunits in Aplysia sensory neurons. Science 260, 222–226 (1993).

27. Chen, C., Nakamura, T. & Koutalos, Y. Cyclic AMP diffusion coefficient in frog olfactory cilia. Biophys. J. 76, 2861–2867 (1999).

28. Neves, S.R. et al. Cell shape and negative links in regulatory motifs together control spatial information flow in signaling networks. Cell 133, 666–680 (2008).

29. Nikolaev, V.O., Bünemann, M., Hein, L., Hannawacker, A. & Lohse, M.J. Novel single chain cAMP sensors for receptor-induced signal propagation. J. Biol. Chem. 279, 37215–37218 (2004).

30. Saucerman, J.J., Greenwald, E.C. & Polanowska-Grabowska, R. Mechanisms of cyclic AMP compartmentation revealed by computational models. J. Gen. Physiol. 143, 39–48 (2014).

31. Harootunian, A.T. et al. Movement of the free catalytic subunit of cAMP-dependent protein kinase into and out of the nucleus can be explained by diffusion. Mol. Biol. Cell 4, 993–1002 (1993).

32. Wen, W. et al. Factors that influence the nuclear accessibility of the catalytic subunit of the cAMP-dependent protein-kinase. FASEB J. 8, A1226 (1994).

33. Dessauer, C.W. Adenylyl cyclase–A-kinase anchoring protein complexes: the next dimension in cAMP signaling. Mol. Pharmacol. 76, 935–941 (2009).

34. Dodge, K. & Scott, J.D. AKAP79 and the evolution of the AKAP model. FEBS Lett. 476, 58–61 (2000).

35. Wang, Y. et al. Isoform-selective disruption of AKAP-localized PKA using hydrocarbon stapled peptides. ACS Chem. Biol. 9, 635–642 (2014).

36. Lim, C.J. et al. Integrin-mediated protein kinase A activation at the leading edge of migrating cells. Mol. Biol. Cell 19, 4930–4941 (2008).

37. Lim, C.J. et al. α4 Integrins are Type I cAMP-dependent protein kinase-anchoring proteins. Nat. Cell Biol. 9, 415–421 (2007).

38. Inoue, T., Heo, W.D., Grimley, J.S., Wandless, T.J. & Meyer, T. An inducible translocation strategy to rapidly activate and inhibit small GTPase signaling pathways. Nat. Methods 2, 415–418 (2005).

39. Durocher, D. et al. The molecular basis of FHA domain:phosphopeptide binding specificity and implications for phospho-dependent signaling mechanisms. Mol. Cell 6, 1169–1182 (2000).

40.Miyawaki, A. & Tsien, R.Y. Monitoring protein conformations and interactions by fluorescence resonance energy transfer between mutants of green fluorescent protein. Methods Enzymol. 327, 472–500 (2000).

41. Lakowicz, J.R. Principles of Fluorescence Spectroscopy 3rd edn. (Springer, 2010).

42. Landgraf, D., Okumus, B., Chien, P., Baker, T.A. & Paulsson, J. Segregation of molecules at cell division reveals native protein localization. Nat. Methods 9, 480–482 (2012).

43. Vandenberg, W. et al. Model-free uncertainty estimation in stochastical optical fluctuation imaging (SOFI) leads to a doubled temporal resolution. Biomed. Opt. Express 7, 467–480 (2016).

44. Zhang, J., Ma, Y., Taylor, S.S. & Tsien, R.Y. Genetically encoded reporters of protein kinase A activity reveal impact of substrate tethering. Proc. Natl. Acad. Sci. USA 98, 14997–15002 (2001).

45. Smith, F.D. et al. Intrinsic disorder within an AKAP-protein kinase A complex guides local substrate phosphorylation. eLife 2, e01319 (2013).

46. Gold, M.G. et al. Architecture and dynamics of an A-kinase anchoring protein 79 (AKAP79) signaling complex. Proc. Natl. Acad. Sci. USA 108, 6426–6431 (2011).

47. Sawano, A. & Miyawaki, A. Directed evolution of green fluorescent protein by a new versatile PCR strategy for site-directed and semi-random mutagenesis. Nucleic Acids Res. 28, E78 (2000).

48. Dedecker, P., Duwe, S., Neely, R.K. & Zhang, J. Localizer: fast, accurate, open-source, and modular software package for superresolution microscopy. J. Biomed. Opt. 17, 5 (2012).

49. Roy, R., Hohng, S. & Ha, T. A practical guide to single-molecule FRET. Nat. Methods 5, 507–516 (2008).

50. Ovesný, M., Křížek, P., Borkovec, J., Svindrych, Z. & Hagen, G.M. ThunderSTORM: a comprehensive ImageJ plug-in for PALM and STORM data analysis and super-resolution imaging. Bioinformatics 30, 2389–2390 (2014).

51. Dean, K.M. et al. Analysis of red-fluorescent proteins provides insight into dark-state conversion and photodegradation. Biophys. J. 101, 961–969 (2011).

52. Manna, P. & Jimenez, R. Time and frequency-domain measurement of ground-state recovery times in red fluorescent proteins. J. Phys. Chem. B 119, 4944–4954 (2015).

53. Vandenberg, W. et al. Model-free uncertainty estimation in stochastical optical fluctuation imaging (SOFI) leads to a doubled temporal resolution. Biomedical optics express 7, 467-480 (2016).

54. Riedl, J. et al. Lifeact: a versatile marker to visualize F-actin. Nature Methods 5, 605-607 (2008).

55. Wiseman, P.W. in Fluorescence Fluctuation Spectroscopy, Vol. 518. (ed. S.Y. Tetin) 245-267 (2013).

56. Annibale, P., Vanni, S., Scarselli, M., Rothlisberger, U. & Radenovic, A. Quantitative Photo Activated Localization Microscopy: Unraveling the Effects of Photoblinking. Plos One 6 (2011).

57. Rossy, J., Owen, D.M., Williamson, D.J., Yang, Z. & Gaus, K. Conformational states of the kinase Lck regulate clustering in early T cell signaling. Nature Immunology 14, 82-89 (2013).

58. Comaniciu, D. & Meer, P. Mean shift: A robust approach toward feature space analysis. Ieee Transactions on Pattern Analysis and Machine Intelligence 24, 603-619 (2002).

59. Wu, Y., Kanchanawong, P. & Zaidel-Bar, R. Actin-Delimited Adhesion-Independent Clustering of E-Cadherin Forms the Nanoscale Building Blocks of Adherens Junctions. Developmental Cell 32, 139-154 (2015).

60. Ripley, B.D. Modeling Spatial Patterns. Journal of the Royal Statistical Society Series B-Methodological 39, 172-212 (1977).

61. Getis, A. & Franklin, J. 2nd-Order Neighborhood Analysis of Mapped Point Patterns . Ecology 68, 473-477 (1987).

62.Rossy, J., Cohen, E., Gaus, K. & Owen, D. M. Method for co-cluster analysis in multichannel single-molecule localisation data. *Histochem. Cell Biol.* 141, 605–12 (2014).

Chapter 4 Live Cell Imaging of H3K9me3 in Super-resolution

Content from this chapter have been included in the following manuscript, currently under review:

R. Hard, N. Li, W. He, **B. Ross**, G. C. H. Mo, Q. Peng, R. Stein, E. Conives, Y. Wang, J. Zhang, W. Wang. "Deciphering and Engineering Chromodomain-Methyllysine Peptide Recognition." *Science Advances.* [under review].

Abstract

Methylation of the tails of histone proteins is a key regulator of chromatin packing and organization. Tri-methylation of lysine 9 of histone 3 (H3K9me), for example, plays a key role in formation and maintenance of constitutive heterochromatin. Here we describe the engineering of a high affinity label for H3K9me3 based on the chromodomain from chromobox protein homolog 1 (CBX1). We then used the mutant CBX1 protein to create live-cell sub-diffraction limit resolution maps of H3K9me3 in the nucleus using two different superresolution microscopy methods: photochromic stochastic optical fluctuation imaging (pcSOFI) and photoactivated localization microscopy (PALM). We demonstrate that the mutant CBX1 chromodomain performs considerably better than wild type CBX1 chromodomain for live cell PALM imaging and results in images comparable to STORM imaging with anti-H3K9me3 antibodies.

Introduction

Imaging histone PTMs has generally required immunofluorescence staining in fixed cells. However, this approach precludes the study changes of the distribution of histone modifications over time. FRET-based approaches have allowed live cell imaging of histone modifications. However, they require exogenous expression of histone peptides and cannot measure endogenous histone PTMs[1-3]. Recent approaches to allow for live cell imaging of endogenous histone modifications have involved fluorescent labeling of antibody fragments, such as scFv-FP fusions[4] or fluorophore-labeled antigen binding fragments (Fabs)[5]. These techniques require domains that are large, unstable, and prone to aggregation in the intracellular environment. The use of histone PTM binding domains from non-histone proteins is a possible alternative; however their use is limited by low binding affinity and specificity. Recent work has demonstrated an FP-fused bromodomain for live cell visualization of acetylation of lysine 14 on histone 3 (H3K14ac), but dimerization of the domain was necessary to have sufficient affinity[6]. Another approach is to directly engineer mutant binding domains that enhance the binding affinity with the PTM of interest. Chromodomains, which are found in many histone-interacting proteins and mediate binding with methyllysine, are a good candidate as a starting point because they are small (<10 kDa), Here we demonstrate the engineering of a the chromobox protein homolog 1 (CBX1) domain to enhance the affinity approximately 10 fold. We then use this domain to create sub diffraction limit resolution maps of tri-metylated histone 3 lysine 9 (H3K9me3) in live cells.

Results and Discussion

Engineering a chromodomain to bind to H3K9me3 with enhanced affinity

To identify candidate chromodomain residues critical for the recognition of H3K9me3, computational modeling of the interaction energetics of chromodomains binding to methyllysine containing peptides was performed. A molecular interaction energy component-support vector machine (MIEC-SVM) model[7-11] was created for 13 different heterochromatin protein 1 (HP1) or Polycomb-like proteins family binding to 457 different peptide sequences (Figure 4.1), starting with either a structure from the Protein Data Bank (PDB) or from homology modeling[12,13]. This model was then used to select important sites on the CBX1 chromodomain to enhance binding to the H3Kme3 chromodomain. First, a list of sites on CBX1 that were important for recognition of specifically of H3K9me3 compared to non-binding peptides was compiled. Then a list of sites important for binding to all CBX1 binders compared to the non-binder H3K27me3 was compiled to identify residues generally important for binding. Residues that were too conserved among chromodomains or did not contribute sufficiently to the binding energy difference of binding vs. non binding petides were filtered (Figure 4.2). Sites 59, 60, and 62 were identified as potential sites important for binding to H3K9me3, and 22, 25, and 59 were identified as potential sites generally important for binding.

Residues 22, 25, 59, 60, and 62 on CBX1 were randomized using degenerate codons (NNK), and yeast surface display screening was performed using a biotin-labelled H3K9me3 peptide. The selected mutants from the yeast surface display screening were then tested for their affinity for H3K9me3 by a fluoresescence polarization binding assay. The two mutants (V22E/K25S/D59F and V22E/K25E/D59S) demonstrated enhanced binding to H3K9me3 compared to the wild type domain (0.32 and 0.21 μM, respectively, compared to 2.78 μM for the wild type domain) (Figure 4.3). However, only weak binding to the H3K27me3 peptide was observed. The V22E/K25E/D59S variant was screened against a MODified Histone Peptide Array (Active Motif), containing 384 histone marks. The screen demonstrated that CBX1(V22E/K25E/D59S) maintained the specificity of the wild type CBX1 (Figure 4.4).

Figure 4.1 Flow chart of MIEC-SVM Model

a). Flow chart of MIEC-SVM that predicts binding specificity between chromodomains and methyllysine peptides. Complex structures between 13 chromodomains and 457 peptides were constructed by computationally mutating peptide sequence from a template complex for each chromodomain (Virtual Mutagenesis). From the modeled complex structures, MIEC terms between peptide-protein residues at the binding interface were computed. The MIECs and the binding/non-binding label (obtained from microarray experiments) for each domain-peptide pair were input to a LASSO logistic regression model to select most predictive MIECs (LASSO feature selection). These selected MIEC features were then used to train an SVM model to discriminate binding from non-binding events. b). Performance of MIEC-SVM model on three different peptide groups (all peptides, singly modified peptides, and multiply modified peptides). The MIEC-SVM model showed consistent performance regardless of the number of modifications on the peptides, indicating that chromodomain-peptide recognition share the same MIEC features for singly and multiply modified peptides. c). SVM decision value distribution of the four classes of peptides (binders/non-binders with single or multiple modifications). Binders and non-binders are well separated regardless of the modification number. d). Pair-wise Jensen-Shannon (JS) divergences between the SVM decision value distributions of the four classes. The differences between any binder

Figure 4.1 (continued) class and non-binder class (regardless of the PTM number) are large (larger JS divergence value): singly modified binder-singly modified non-binder, JS = 0.468 (p-value < 1.0 x 10-20); singly modified binder-multiply modified nonbinder, JS = 0.396 (p-value < 1.0 x 10-19); multiply modified binder-single modified non-binder, JS = 0.704 (p-value < 1.0 x 10-20); multiply modified binder-multiply modified non-binder, JS = 0.603 (p-value < 1.0 x 10-20). In contrast, binder (or non-binder) peptides are similar to each other regardless of the PTM numbers: JS values of 0.113 for binders (p-value = 7.0 x 10-15 for statistical similarity) and 0.027 for non-binders (p-value = 6.1 x 10-10). All p-values were calculated based on the background distributions of JS divergence of randomly selected decision values for the same number of binders or non-binders as the foreground.

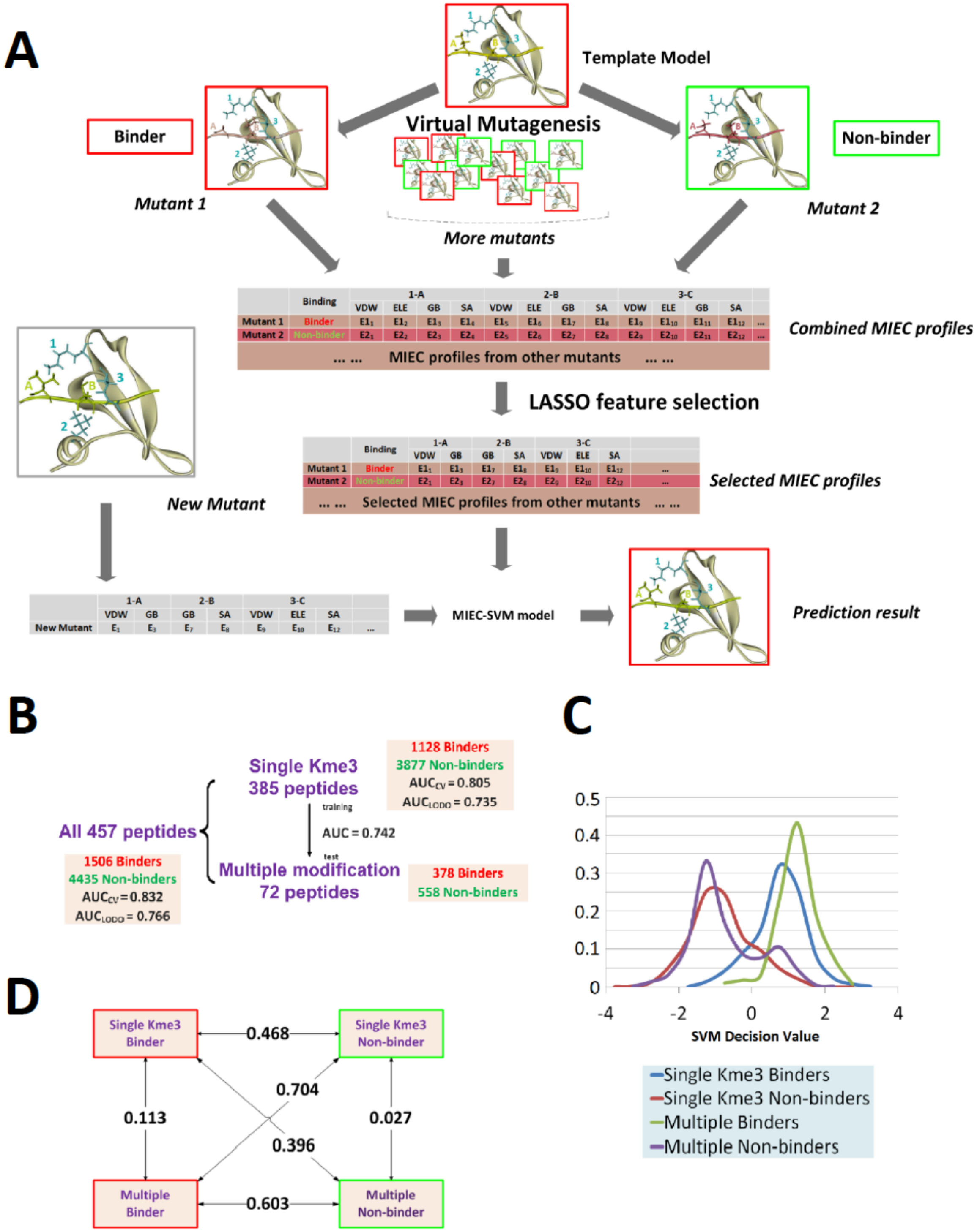
A
Template Model
Virtual Mutagenesis
Binder
Mutant 1
Non-binder
Mutant 2
More mutants
Binding
1-A
2-B
3-C
VDW ELE GB SA VDW ELE GB SA VDW ELE GB SA
Mutant 1 Binder E1₁ E1₂ E1₃ E1₄ E1₅ E1₆ E1₇ E1₈ E1₉ E1₁₀ E1₁₁ E1₁₂ ...
Mutant 2 Non-binder E2₁ E2₂ E2₃ E2₄ E2₅ E2₆ E2₇ E2₈ E2₉ E2₁₀ E2₁₁ E2₁₂ ...
... ... MIEC profiles from other mutants ... ...
Combined MIEC profiles
LASSO feature selection
Binding
1-A
2-B
3-C
VDW GB GB SA VDW ELE SA
Mutant 1 Binder E1₁ E1₃ E1₇ E1₈ E1₉ E1₁₀ E1₁₂ ...
Mutant 2 Non-binder E2₁ E2₃ E2₇ E2₈ E2₉ E2₁₀ E2₁₂ ...
... ... Selected MIEC profiles from other mutants ... ...
Selected MIEC profiles
New Mutant
1-A
2-B
3-C
VDW GB GB SA VDW ELE SA
New Mutant E₁ E₃ E₇ E₈ E₉ E₁₀ E₁₂ ...
MIEC-SVM model
Prediction result
1
2
3
A
B
B
All 457 peptides
1506 Binders
4435 Non-binders
AUC_{CV} = 0.832
AUC_{LODO} = 0.766
Single Kme3
385 peptides
1128 Binders
3877 Non-binders
AUC_{CV} = 0.805
AUC_{LODO} = 0.735
training
AUC = 0.742
test
Multiple modification
72 peptides
378 Binders
558 Non-binders
C
0.5
0.4
0.3
0.2
0.1
0
-4
-2
0
2
4
SVM Decision Value
Single Kme3 Binders
Single Kme3 Non-binders
Multiple Binders
Multiple Non-binders
D
Single Kme3 Binder
Single Kme3 Non-binder
Multiple Binder
Multiple Non-binder
0.468
0.704
0.113
0.027
0.396
0.603

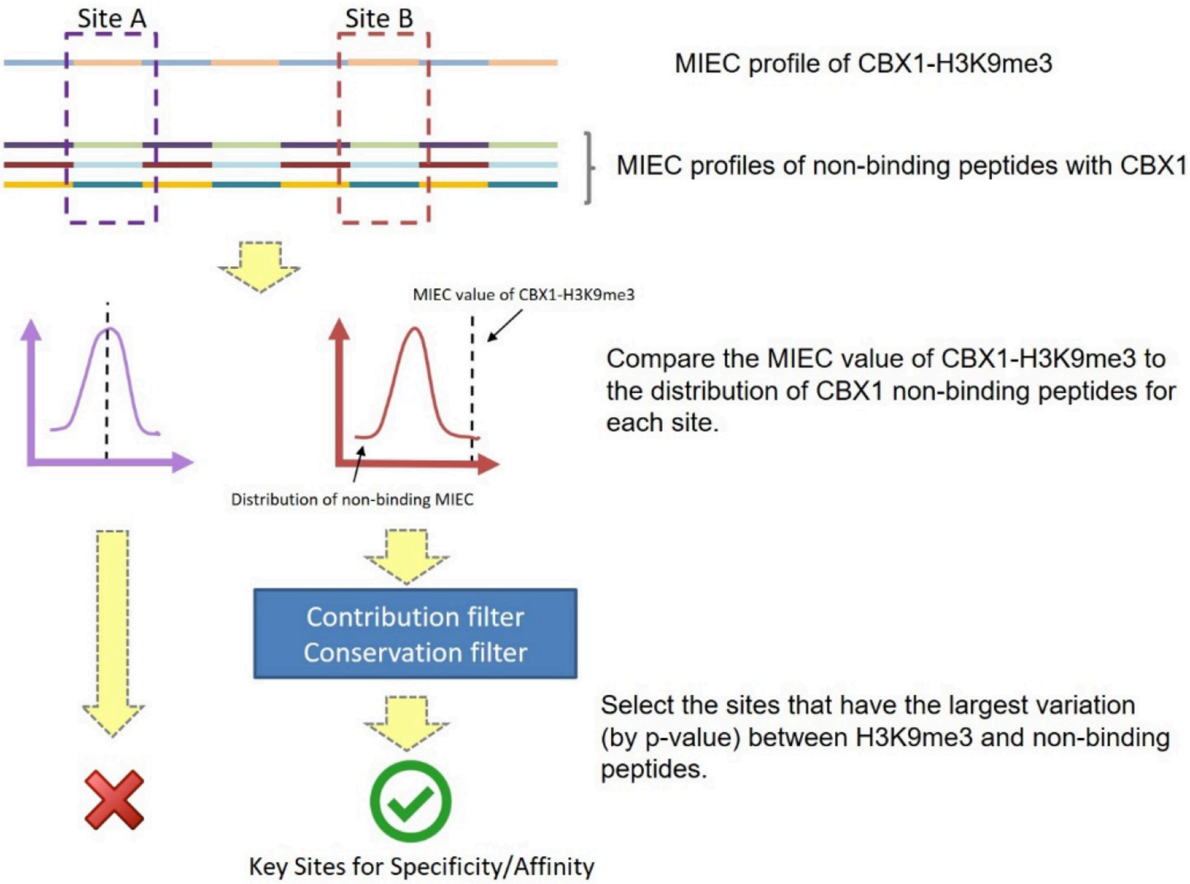

Figure 4.2 Selection of key residues using MIEC-SVM Model

Selection of key sites to randomize for the yeast display experiment with the CBX1 chromodomain. Sites "A" and "B" are just two representative residues being analyzed for site selection for demonstration purposes. The other strategy of selecting residues to randomize on CBX1 (comparing H3K27me3 to CBX1 binders) used the same procedure

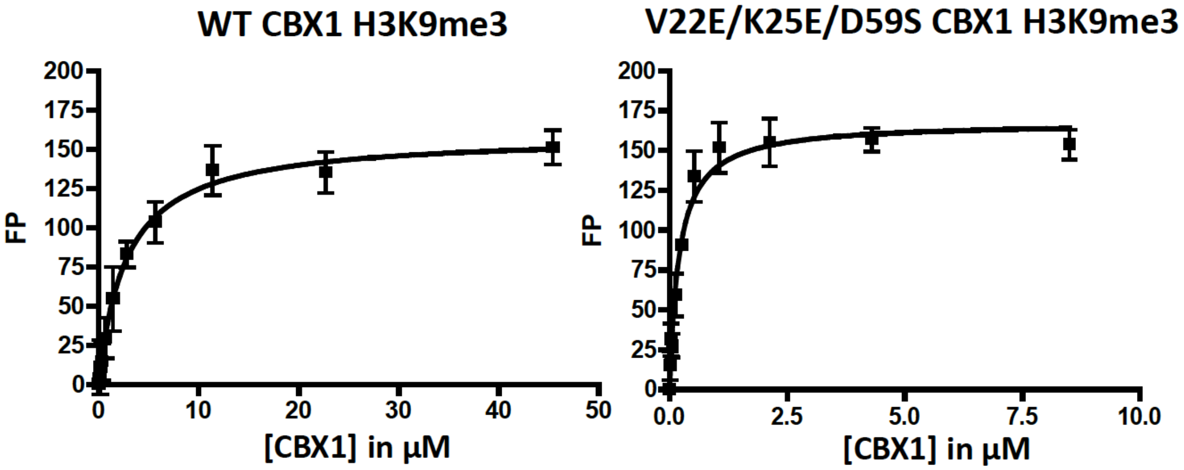

Mutant	K_D to H3K9me3	K_D to H3K27me3
WT CBX-1	2.78 ± 0.60 µM	Too weak
V22E/K25E/D59S (CBX1)	0.21 ± 0.04 µM	Too weak
V22E/K25S/D59F (CBX1)	0.32 ± 0.07 µM	Too weak
WT MPP8	0.50 ± 0.12 µM	Too weak

Figure 4.3 Measuring Binding of CBX1(V22E/K25E/D59S) using Fluorescence Polarization Binding Assay

Dissociation constant (KD) values obtained from fluorescence polarization binding studies between the WT CBX1 and MPP8 chromodomains, along with the V22E mutants isolated from yeast surface display selections. The KD values were derived from a nonlinear regression equation after performing experiments in triplicate

Figure 4.3 (continued) against 1 nM H3K9me3 (NH2-ARTKQTARK(me3)STGG-mini-PEG-K(5-fam)-NH2) and 1 nM H3K27me3 (Ac-QLATKAARK(me3)SAPA-mini-PEG-K(5-fam)-NH2) peptides. KD values towards H3K27me3 are based on visual approximation from unsaturated binding curves, for the V22E mutants, up to 180 µM of each protein was used in an attempt to get a binding curve to H3K27me3.

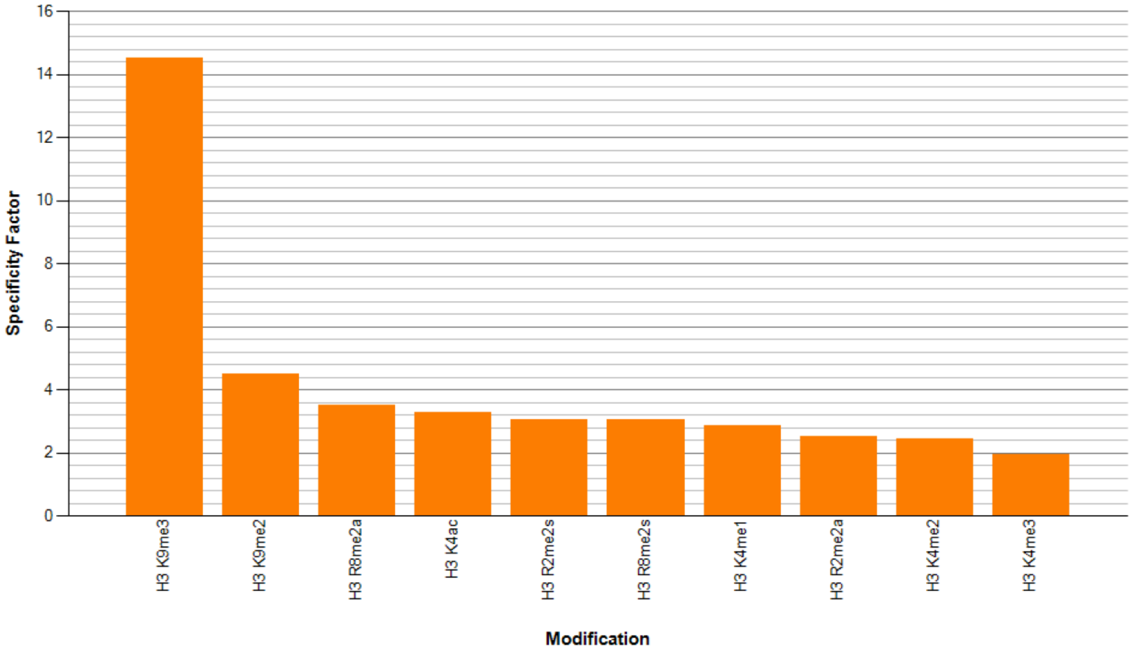

Figure 4.4 Peptide array screening of the V22E/K25E/D59S CBX1 chromodomain mutant

An Active Motif histone peptide array, containing 384 peptide spots printed in duplicate, was screened against 1 nM of the GST-CBX1 mutant. Spots were visualized by chemiluminescence and the spot intensities were analyzed by Active Motif array analysis software. The height of the y-axis (specificity factor) represents the ratio of the average intensity of all array spots containing the mark (listed on the x-axis) over the average intensity of spots not containing the mark.

Superresolution Mapping of H3K9me3 with CBX1(V22E/K25E/D59S)

We aimed to test whether we could use CBX1(V22E/K25E/D59S) to create superresolution spatial maps of the H3K9me3 modification in the nucleus of living cells. Under two different superresolution imaging modalities, photochromatic stochastic optical fluctuation imaging (pcSOFI)[14] and photoactivatable localization microscopy (PALM)[15], we demonstrated that fluorescently protein-tagged chromodomains can be used to visualize H3K9me3 in live cells. As a result, we were able to obtain subdiffraction information in live cells of the spatial organization of constitutive heterochromatin, marked by H3K9me3 histone modifications and labeled with an engineered high affinity chromodomain.

For pcSOFI imaging, the reversibly switchable fluorescent protein Dronpa was tagged to the C-terminal of the CBX1 triple mutant chromodomain (V3E/K6E/D40S) and transiently expressed the fusion in HeLa cells (Figure 4.5). In this approach, cross-correlation analysis of stochastic intensity fluctuations is used to extract subdiffraction information on the distribution of a blinking fluorophore. The resulting pcSOFI images of the CBX1 triple mutant revealed punctate structures with very high pcSOFI signal, regions where the signal is excluded, as well as a meshwork of regions showing moderate pcSOFI signal.

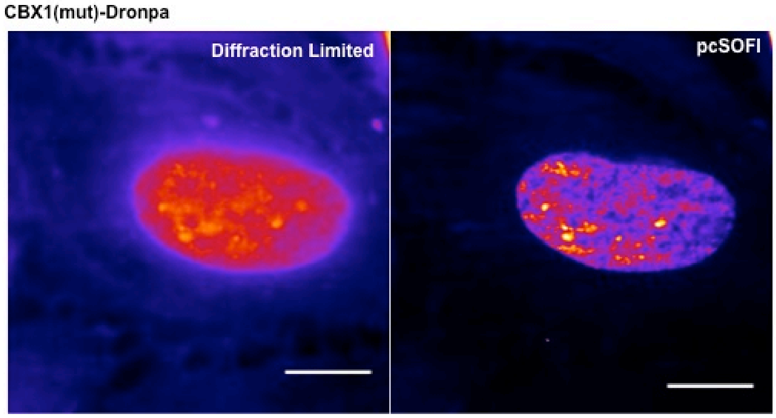

Figure 4.5 pcSOFI Imaging of H3K9me3 using mutant CBX1 domain

Representative deconvolved pcSOFI superresolution image of CBX1(V3E, K6E, D40S)-Dronpa in HeLa cells (left). Diffraction limited image (average image of pcSOFI timecourse) (right).

In addition to pcSOFI, PALM imaging was used to create even higher resolution spatial maps of the H3K9me3 histone modifications (Figure 4.6a). We tagged CBX1(V3E/K6E/D40S) as well as wild type CBX1 with a photoactivatable mCherry (PAmCherry) fluorescent protein (Subach et al Nature Methods 2009) at the C-terminus and transiently expressed these constructs in HeLa or wild type W8 mouse embryonic fibroblasts (MEF) cells. The resulting reconstructed images of CBX1(V3E/K6E/D40S) reveal a similar pattern observed in the pcSOFI images: punctate structures with very dense labeling as well as a meshwork pattern of moderately high localization density interspersed with regions with lower labeling (Figure 4.6a). The wild type CBX1, on the other hand, showed a different pattern of labeling. The mutant showed a high level of nuclear localization (approximately 85% in MEF and 95% in HeLa cells), impressive given the lack of a nuclear localization sequence (NLS) tag in the construct (Figure 4.6b). This was an obvious improvement over the WT domain, and is comparable to fixed-cell images created using an antibody against H3K9me3 (Abcam ab8898).

We then compared the live cell PALM images to fixed cell STORM imaging using an anti-H3K9me3 monoclonal antibody and an Alexa647-labeled secondary antibody (Figure 4.6). This STORM imaging resulting pattern of staining and relative contrast between densely labeled and sparsely labeled regions is more similar to the CBX1 triple mutant. We hypothesize that the higher affinity of the triple mutant allows it localize to regions where H3K9me3 is present but not as enriched, allowing it to show a distribution more similar to what is detected by antibody staining of the H3K9me3 modification.

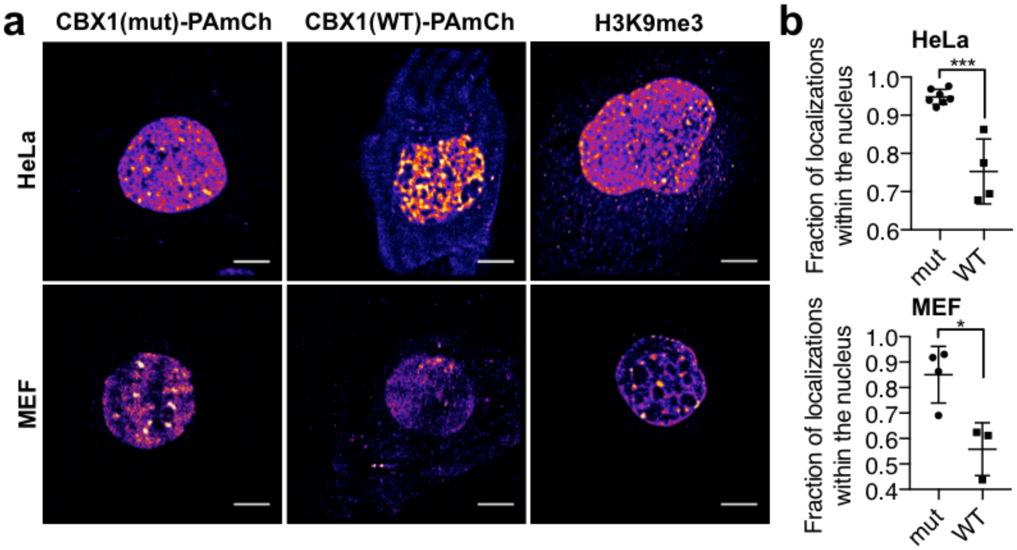

Figure 4.6 Live-cell PALM imaging of H3K9me3 with mutant CBX1 domain compared to Fixed-cell Immunostaining

a). Representative reconstructed PALM image of HeLa cells (top row) and MEF cells (bottom row) transiently transfected with CBX1 (V22E/K25E/D59S)-PAmCherry (left) CBX1-WT-PAmCherry (center), or fixed-cell, immunostained STORM image with Alexa647-labeled anti-H3K9me3 antibody (right). All scale bars are 10µm. b). Quantification of fraction of PALM localizations located within the nuclear region for HeLa cells (top) and MEF cells (bottom) (unpaired two-tailed t-test). Mut: V22E/K25E/D59S triple mutant, WT: wild type.

We subsequently performed live-cell PALM and fixed-cell STORM microscopy on a D5 MEF cell line with a double-knockout of Suv39h, the methyltransferase responsible for methylation of H3K9me3. It has been shown that, while double knockout of Suv39h does reduce the amount of H3K9 methylation, it does not abolish it entirely, but rather there is residual methylated H3K9[16]. While no nuclear labeling was observed with the wild type CBX1, nuclear labeling was observed with the mutant CBX1 and with the anti-H3K9me3 antibody (Figure 4.7). We hypothesize that due to the lower affinity of the wild type CBX1, it was not able to effectively label the lower concentration of H3K9me3 in the Suv39h knockout line. Consistent with the anti-H3K9me3, the mutant CBX1 but not the wild type CBX1 was able to detect the residual H3K9me3 present despite the knockout of the methyltransferase.

Furthermore, we tested the degree of co-localization of the triple mutant with the antibody in two-color fixed STORM imaging in HeLa cells (Figure 4.8). The extent of co-localization was determined using a published method based on a bivariate version of Getis and Franklin's local point pattern analysis (Figure 4.8b, Figure 4.9)[17]. We measured that an average of 63% of localizations of the CBX1 mutant co-clustered with the H3K9me3 antibody, and 94% of H3K9me3 antibody localizations co-clustered with mutant CBX1 (V22E/K25E/D59S). This data is consistent with the peptide array data and confirms the CBX1 mutant's specificity for the H3K9me3 mark within the cellular environment.

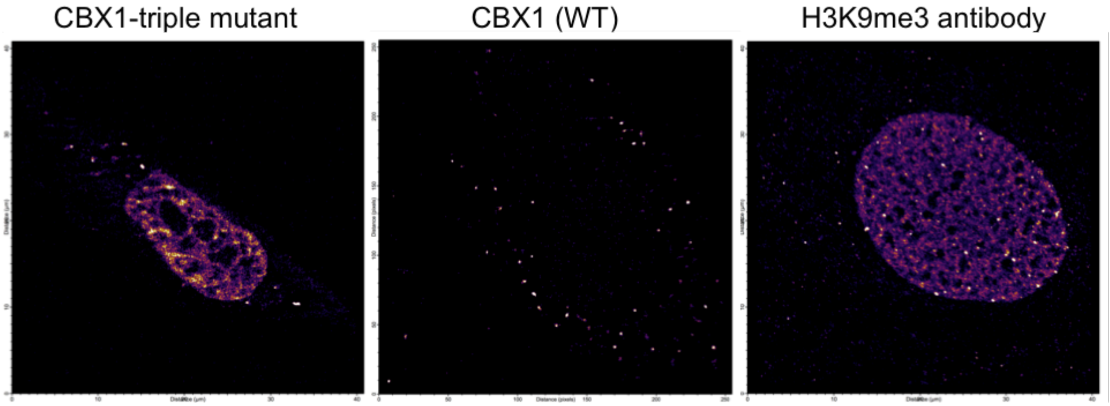

Figure 4.7 Live cell PALM and fixed cell STORM imaging of H3K9me3 in Suv39h double knockout MEF cells

a). Representative reconstructed PALM image of MEF D5 Suvh39h-/- cells transiently transfected with CBX1 (V22E/K25E/D59S)-PAmCherry (left) CBX1-WT-PAmCherry (center), or fixed-cell, immunostained STORM image with Alexa647-labeled anti-H3K9me3 antibody (right). All scale bars are 10µm. b). Mut: V22E/K25E/D59S triple mutant, WT: wild type.

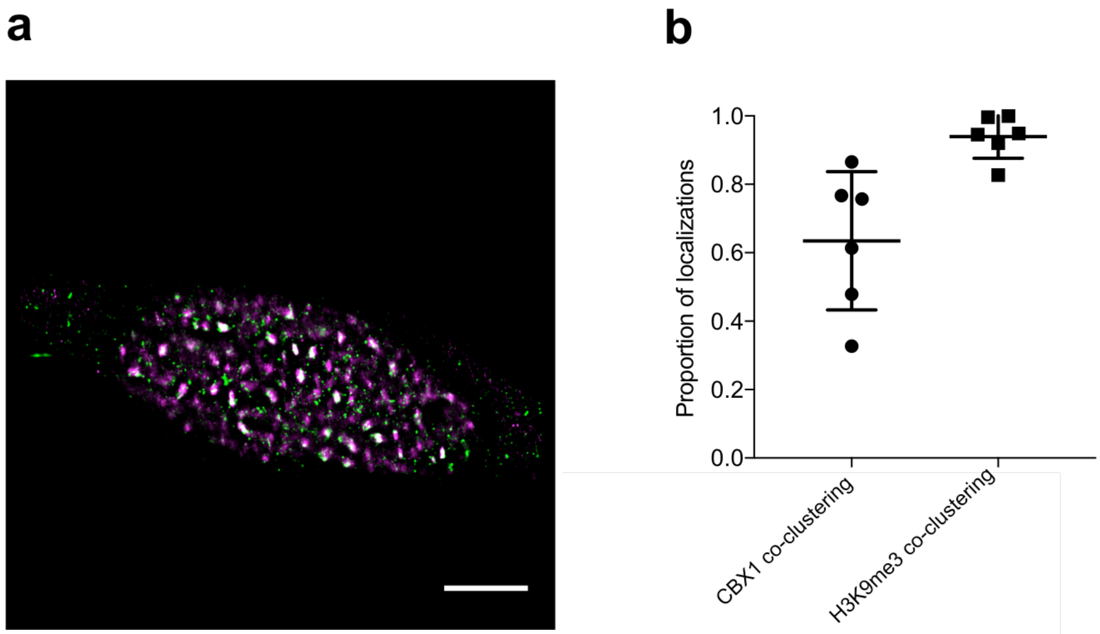

Figure 4.8 Two-Color STORM Imaging with CBX1 mutant and anti-H3K9me3 Antibody

a). Representative two-color STORM image of HeLa cell labeled withanti-H3K9me3 ab and Alexa Fluor 647 secondary antibody (magenta) and Flag-CBX1mutant/Alexa Fluor 568-anti-Flag ab (green). White represents strong co-localization. b). CBX1 (V22E/K25E/D59S) and H3K9me3-antibody (ab) (Abcam ab8898) co-localization analysis. Extent of co-clustering of CBX1 (V22E/K25E/D59S) and H3K9me3-ablocalizations in two-color STORM images was measured using a bivariate version of Getis and Franklin's local point analysis[17]. For each localization in one channel, the number of localizations in the other channel within 200nm was counted. A number above 150 represents co-clustering. Shown here are the proportion of **Figure 4.8 (continued)** localizations for CBX1 (V22E/K25E/D59S) that co-clustered with the H3K9me3 antibody (left) and the proportion of H3K9me3 antibody localizations that co-clustered with CBX1 (V22E/K25E/D59S) (right). Each data point represents the proportion of localizations per cell.

a H3K9me3 co-clustering analysis with respect to CBX1(V3E/K6E/D40S)

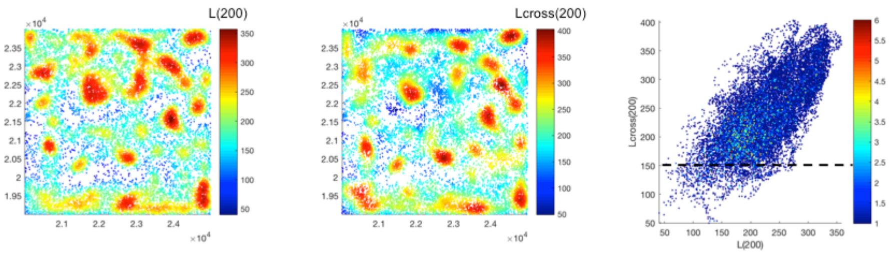

b CBX1(V3E/K6E/D40S) co-clustering analysis with respect to H3K9me3

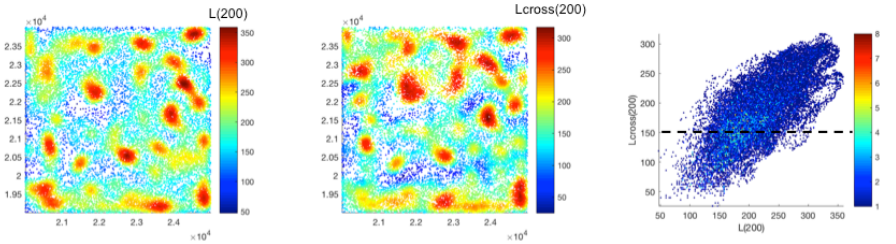

Figure 4.9 Bivariate Getis-Franklin Co-clustering Analysis of CBX1(V3E/K6E/D40S) and anti-H3K9me3 antibody

Bivariate Getis-Franklin single molecule co-clustering analysis of H3K9me3 and CBX1(V3E/K6E/D40S). An anti-H3K9me3 antibody, labeled with Alexa647, and CBX1(V3E/K6E/D40S), labeled with Alexa568, were co-imaged in fixed HeLa cells using STORM microscopy. a). Representative scatter plot showing molecular localizations for the anti-H3K9me3 antibody, color-coded with the values for L(200) (left) and Lcross(200) (center), which reflect the number of localizations in its own species or of the other species, respectively, within a 200 nm radius of each localization. A scatter plot of Lcross(200) and L(200) is shown (right). Localizations with a Lcross(200) score above 150 were considered co-clustered. b). Representative scatter plots showing molecular localizations of CBX1(V3E/K6E/D40S) in the same region, color-coded with L(200) (left) or Lcross(200) (center). A scatter plot of Lcross(200) vs. L(200) is shown (right).

Materials and Methods

Template Construction and Conformational sampling

The template chromo-peptide complex structures for 13 chromodomains (CBX1-8, MPP8, CDYL1, CDYL2, SUV91, SUV92) were obtained from either PDB or homology modeling based on a previously described method[12,13]. The peptide in each chromo-peptide structure contains 9 residues (truncated if more than 9) with tri-methylated lysine on the 8th position. For each chromo-peptide template, molecular dynamics (MD) simulation was performed for conformational optimization and sampling. Binding interface residue backbone RMSD was evaluated for the 13 chromodomains to verify the equilibrium. After the production run, 8 snapshots were evenly selected from the trajectory between 3 to 5 ns as chromo-peptide binding complex templates for each system. The chromo-peptide binding complex templates were mutated in silico to each of the 457 peptides. Restrained by the computational cost, we performed 5000 steps of energy minimization instead of MD simulation to optimize all the complex structures obtained through mutation. (See supporting information for details.)

Calculation of molecular interaction energy components

Residue pair-wise energy decomposition on minimized structures was performed by mm_pbsa.pl in the assisted model building with energy refinement (AMBER) package[18-20], and a molecular interaction energy component (MIEC) profile was generated based on the energy decomposition result consisting of chromo-peptide MIEC profile and peptide internal MIEC profile. For chromo-peptide MIEC profile, the energy contributions from 8 snapshots are averaged and all residue pairs less than 10 Å were included to reflect binding characteristics of the chromo-peptide interactions. The sequences of chromodomains were aligned using sequence and structural information to match residues from different domains. For peptide internal MIEC profile, MIECs of the adjacent peptide residue pairs were calculated to represent the conformational preference of the peptide. MIEC profile for each chromo-peptide interaction contains 158 chromo-peptide residue pairs and 8 peptide-peptide pairs (664 energy components in total).

Construction, Training and Testing of the MIEC-support vector machine model

LASSO (Least Absolute Shrinkage and Selected Operator) logistic regression method[21] was applied to the MIEC profile to select informative features to construct the MIEC-support vector machine (MIEC-SVM) model (see Table S4). All SVM training and tests were conducted using the LIBSVM package[22]. The polynomial kernel function was used. A nested cross validation was performed to exclude an over-fitting issue in the training process (see supplementary material for details and Table S5). Both 3-fold cross validation and leave-one-domain-out (LODO) test were performed to evaluate the prediction accuracy of the MIEC-SVM model.

Selection of Candidate Sites to Randomize on the CBX1 Chromodomain

To select for sites to randomize in the CBX1 library in order to enhance its binding affinity towards H3K9me3, we used two different strategies. The first was to identify residues important for binding H3K9me3 compared to non-binding peptides. Comparison of MIEC components of H3K9me3 binding to non-binder components, along with avoiding choosing residues that were too conserved amongst chromodomains, we constructed a ranked list of candidate sites that showed the largest energetic difference between binders to non-binders. The second strategy was essentially the same as the first strategy except that we selected sites generally important for CBX1 binding by comparing all CBX1 binder MIECs to a representative non-binder (H3K27me3). Again, a conservation filter was applied to prevent selection of structurally important residues on the chromodomain.

Yeast Surface Display Library Construction and Screening

The five sites selected for randomization on the CBX1 chromodomain (residues 22, 25, 59, 60, and 62 of NCBI P83916.1) were fully randomized using primers containing NNK degenerate codons, where the WT domain was used as template for PCR (FWD: 5’-acaattcgtctcggtaccagaatatNNKgtggaaNNKgttctcgaccgtcgagtggtaaagggcaaagtggagtac-3’, REV: 5’-ataattcgtctcctcgagtgttttctgtgactgcagaaactcagcaatgagMNNgggMNNMNNcaggttctcttctggc-3’ (N is any base, K is g/t, M is c/a). The library was ligated into a modified pYD1 vector, followed by transformation into EBY100 yeasts using the LiAc/ssDNA/PEG-3350 method[23], resulting in approximately 106 transformants. The yeast surface display library was screened using biotin-Y-ahx-RTKQTARK(me3)S-NH2 (ahx = aminohexanoic acid) as the antigen[24]. Yeast were sorted on a BD FACSAria II (Moores Cancer Center, University of California San Diego). Random hits were sequenced by dideoxy sequencing.

Fluorescence Polarization

Fluorescein-labeled methylated histone peptides (Karebay) were used for KD determination by serial dilution in triplicate. The peptides used were H3K9me3 (NH2-ARTKQTARK(me3)STGG-minipeg-K(5-fam)-NH2) or H3K27me3 (Ac-QLATKAARK(me3)SAPA-minipeg-K(5-fam)-NH2) at a concentration of 1 nM. The serial dilutions were in TBS buffer (25 mM Tris, 125 mM NaCl, pH 8). FP values were read on a DTX 880 Multimode Detector Beckman Coulter plate reader with excitation filter at 485 nm and two emission filters at 535 nm equipped with polarizers. Data were fit to a nonlinear regression equation using GraphPad Prism 4 software.

Molecular Cloning, Cell Culture, Transfection, and Immunocytochemistry

The CBX1 chromodomain (either wild type or the triple mutant) was cloned into a pcDNA3 vector and fused to the N-terminus of the photoactivatable mCherry protein. HeLa and MEF cells were cultured using standard protocols and plated on 3.5 cm glass-bottom dishes for imaging. For live-cell photoactivated localization microscopy (PALM) imaging, HeLa and MEF cells were transiently transfected using either Lipofectamine 2000 (Thermo-Fisher Scientific) or Polyjet (SignaGen). For fixed-cell stochastic optical reconstruction microscopy (STORM) imaging, cells were fixed with 4% paraformaldehyde (PFA) for 20 min, and then washed with 100 mM glycine in Hank's balanced salt solution (HBSS) to quench the free PFA. Cells were permeabilized and blocked in a permeabilization solution with 0.1% Triton-X, 0.2% BSA, 5% goat serum, and 0.01% sodium azide in HBSS. The cells were then incubated overnight at 4°C with an anti-H3K9me3 antibody (Abcam ab8898) at a 1:500 dilution, followed by 1-2 hours with goat anti-rabbit Alexa 647-conjugated antibodies at 1:1000 dilution. The cells were then post-fixed again in 4% PFA, quenched with 100 mM glycine in HBSS, and washed with HBSS to prepare for imaging. Immediately before imaging, the media was changed to STORM-compatible buffer (50mM Tris-HCl pH 8.0, 10mM NaCl, 10% glucose) with 560 µg/ml glucose oxidase, 170 µg/ml catalase, and 7.7 mg/ml mercaptoethylamide.

For the two-color STORM imaging, the cells were incubated over night at 4°C with a mouse anti-FLAG antibody (Sigma F1804, for detection of FLAG-tagged CBX1) at a 1:200 dilution and with a rabbit anti-H3K9me3 antibody (Abcam 8898) at a 1:500 dilution. They were then incubated 1-2 hours with goat anti-rabbit and anti-mouse antibodies, labeled with Alexa647 and Alexa568 respectively, at a 1:1000 dilution.

Super-Resolution Imaging and Image Analysis

STORM and PALM images were obtained using a Nikon Ti TIRF microscope with N-STORM, an Andor IXON3 Ultra DU897 EMCCD, and a 100X oil-immersion TIRF objective. Photoactivation was driven by a Coherent 405 nm laser, while excitation was driven either with a Coherent 561 nm laser or a 647 nm laser. Illumination was done in a “near-TIRF” format, in which the TIRF angle was adjusted so that molecules in the nucleus were illuminated. All image analysis and image reconstruction was performed using the Localizer software[25] in the Igor Pro 6.3 environment. STORM and PALM images were segmented using the GLRT algorithm[25] and localizations were fit using

Gaussian fitting. Reconstructed bitmap images were created in which intensity corresponds to the number of localizations in each box in a 0.2 pixel-wide grid. For two-color STORM imaging co-localization analysis, the protocol can be found in supplemental methods.

Two-Color Stochastic Optical Reconstruction Microscopy (STORM) Imaging Co-Localization Analysis

For two-color STORM imaging, acquisitions for the two channels were interleaved. Image analysis and reconstruction were performed using the N-STORM software package. Before the co-clustering analysis was performed, over-counting of localizations due to persistence of the fluorescence of an emitter for multiple frames and blinking was corrected by grouping localizations within 100nm separated by less than a particular dark time (t_d) and treating them as coming from a single emitter. The appropriate dark time for each fluorophore was determined using a published method[26,27]. The nmber of localizations after such grouping was determined for varying values of t_d, and the data were fit to the following equation.

$$N(t_d) = N(1 + n_{blink,1}e^{\frac{(1-t_d)}{t_{off,1}}} + n_{blink,2}e^{\frac{(1-t_d)}{t_{off,2}}})$$

Here, $N(t_d)$ is the number of localizations after grouping with a particular dark time, N is the real number of fluorescent molecules, $n_{blink,1}$ and $n_{blink,2}$ are the number of dark state conversions occurring with average dark state lifetimes $t_{off,1}$ and $t_{off,2}$, respectively. For Alexa568, the fit showed that 0.8 blinks per molecule occurred for dark states with a lifetime of 11.4 frames, and 1.4 blinks per molecule occurred for dark states with a lifetime of 90 frames. For Alexa647, the fit showed that 0.3 blinks per molecule occurred for dark states with a lifetime of 9.2 frames, and 0.7 blinks per molecule occurred for dark states with a timescale of 171 frames. Values of the dark time were chosen to be approximately double the lifetime of the longer blinking timescale, or 180 frames for Alexa568 and 340 frames for Alexa647.

Co-clustering analysis was performed using a published method[17,28], based on a bivariate version of Getis and Franklin's local point pattern analysis using MATLAB software. For each localization in one channel, the number of localizations in the other channel within 200nm was counted, with that statistic being called L(200)cross. A threshold of L(200)cross of 150 was set for a particular localization to be considered co-localized with a cluster of the other channel. We then determined the percentages of localizations in each channel that were localized within clusters of the other channel for each cell.

Personal Contributions

I performed the cloning of the fluorescent protein-fused CBX1 wild type and mutant variants, as well as the pcSOFI, PALM, and STORM imaging of all these constructs in HeLa and MEF cell lines. I also performed the subsequent data analysis for the various superresolution imaging experiments, including pcSOFI analysis, single-molecule localization, image reconstruction, as well as spatial pattern analyses.

References

1. Chi-Wang Lin, Cindy Y. Jao, and, and Alice Y. Ting. Genetically Encoded Fluorescent Reporters of Histone Methylation in Living Cells. *JACS* 126 (19), 5982-5983 (2004).
2. Kazuki Sasaki, Tamaki Ito, Norikazu Nishino, Saadi Khochbin, and Minoru Yoshida. Real-time imaging of histone H4 hyperacetylation in living cells. *PNAS* 106 (38) 16257–16262 (2009).
3. Nakaoka S, Sasaki K, Ito A, Nakao Y, Yoshida M. A Genetically Encoded FRET Probe to Detect Intranucleosomal Histone H3K9 or H3K14 Acetylation Using BRD4, a BET Family Member. *ACS Chem Biol*. 11(3):729-33 (2016).
4. Yuko Sato, Masanori Mukai, Jun Ueda, Michiko Muraki, Timothy J. Stasevich, Naoki Horikoshi, Tomoya Kujirai, Hiroaki Kita, Taisuke Kimura, Seiji Hira, Yasushi Okada, Yoko Hayashi-Takanaka, Chikashi Obuse, Hitoshi Kurumizaka, Atsuo Kawahara, Kazuo Yamagata, Naohito Nozaki, and Hiroshi Kimura. Genetically encoded system to track histone modification *in vivo. Sci Rep*. 3: 2436 (2013).
5. Hayashi-Takanaka Y, Yamagata K, Wakayama T, Stasevich TJ, Kainuma T, Tsurimoto T, Tachibana M, Shinkai Y, Kurumizaka H, Nozaki N, Kimura H. Tracking epigenetic histone modifications in single cells using Fab-based live endogenous modification labeling *Nucleic Acids Res*. 39 (15):6475-88 (2011).
6. Oscar F. Sanchez, Agnes Mendonca, Ana D. Carneiro, and Chongli Yuan. Engineering Recombinant Protein Sensors for Quantifying Histone Acetylation. *ACS Sens* 2 (3), pp 426–435 (2017).

7. Tingjun Hou, Wei Zhang, David Case, Wei Wang. Characterization of domain-peptide interaction interface: A case study on the amphiphysin-1 SH3 domain, *Journal of Molecular Biology*, 376, 1201-1214 (2008).
8. Tingjun Hou, Zheng Xu, Wei Zhang, William A. McLaughlin, David A. Case, Yang Xu and Wei Wang. Characterization of domain-peptide interaction interface: a generic structure-based model to decipher the binding specificity of SH3 domains, *Molecular & Cellular Proteomics* 8, 639-649 (2009).
9. Tingjun Hou, Nan Li, Youyong Li, Wei Wang. Characterization of Domain-Peptide Interaction Interface: Prediction of SH3 Domain-Mediated Protein-Protein Interaction Network in Yeast by Generic Structure-Based Models. *Journal of Proteome Research* 11, 2982-2995 (2012).
10. Nan Li, Tingjun Hou, Bo Ding, Wei Wang. Characterization of PDZ domain-peptide interaction interface based on energetic patterns. *Proteins: Structure, Function, and Bioinformatics* 79, 3208-3220 (2011).
11. Nan Li, Richard Ainsworth, Meixin Wu, Bo Ding, Wei Wang. MIEC-SVM: automated pipeline for protein peptide/ligand interaction prediction. *Bioinformatics* 32, 940-942 (2016).
12. Li N, Stein RS, He W, Komives E, Wang W. Identification of methyllysine peptides binding to chromobox protein homolog 6 chromodomain in the human proteome. *Mol Cell Proteomics* 12, 2750-2760 (2013).
13. Stein RS, Li N, He W, Komives E, Wang W. Recognition of Methylated Peptides by Drosophila melanogaster Polycomb Chreromodomain. *J Proteome Res.* 12 (3):1467-77. (2013).

14. Peter Dedecker, Gary C. H. Mo, Thomas Dertinger, and Jin Zhang. Widely accessible method for superresolution fluorescence imaging of living systems. *PNAS* vol. 109 no. 27 10909–10914 (2012).

15. Eric Betzig, George H. Patterson, Rachid Sougrat, O. Wolf Lindwasser, Scott Olenych, Juan S. Bonifacino, Michael W. Davidson, Jennifer Lippincott-Schwartz, Harald F. Hess. Imaging Intracellular Fluorescent Proteins at Nanometer Resolution. *Science* Vol. 313, Issue 5793, pp. 1642-1645 (2006).

16. Jack, A. P. M. *et al*. H3K56me3 is a novel, conserved heterochromatic mark that largely but not completely overlaps with H3K9me3 in both regulation and localization. *PLoS One* 8, e51765 (2013).

17. Rossy, J., Cohen, E., Gaus, K. & Owen, D. M. Method for co-cluster analysis in multichannel single-molecule localisation data. *Histochem. Cell Biol.* 141, 605–12 (2014).

18. D.A. Case, T. A. D., T.E. Cheatham, III, C.L. Simmerling, J. Wang, R.E. Duke, R. et al. (University of California, San Francisco, 2010).

19. Duan, Y. et al. A point-charge force field for molecular mechanics simulations of proteins based on condensed-phase quantum mechanical calculations. J Comput Chem 24, 1999-2012 (2003).

20. Wang, J., Wolf, R. M., Caldwell, J. W., Kollman, P. A. & Case, D. A. Development and testing of a general amber force field. Journal of Computational Chemistry 25, 1157-74 (2004).

21. Tibshirani, R. Regression Shrinkage and Selection via the Lasso. *J. r. Stat. Soc. B* 58, 267–288 (1996).

22. Chang CCL, C.J. (2001) Software available at http://www.csie.ntu.edu.tw/~cjlin/libsvm.

23 R Daniel Gietz & Robert H Schiestl (2007). High-efficiency yeast transformation using the LiAc/SS carrier DNA/PEG method. Nature Protocols 2, 31-34.

24. Ginger Chao, Wai L Lau, Benjamin J Hackel, Stephen L Sazinsky, Shaun M Lippow & K Dane Wittrup. Isolating and engineering human antibodies using yeast surface display (2006). Nature Protocols 1, 755-768.

25. Dedecker, P., Duwe, S., Neely, R.K. & Zhang, J. Localizer: fast, accurate, open-source, and modular software package for superresolution microscopy. J. Biomed. Opt. 17, 5 (2012).

26. Annibale, P., Vanni, S., Scarselli, M., Rothlisberger, U. & Radenovic, A. Quantitative Photo Activated Localization Microscopy: Unraveling the Effects of Photoblinking. *PLoS ONE* 6(7): e22678.

27. Rossy, J., Owen, D.M., Williamson, D.J., Yang, Z. & Gaus, K. Conformational states of the kinase Lck regulate clustering in early T cell signaling. *Nature Immunology* 14, 82-89 (2013).

28. Getis, A. & Franklin, J. 2nd-Order Neighborhood Analysis of Mapped Point Patterns
. Ecology 68, 473-477 (1987).

Chapter 5 Concluding Remarks

We have presented here three novel and distinct technologies that push the boundaries of genetically encodable fluorescent biosensors. These new molecular tools allow the researcher to collect types of information otherwise unavailable or difficult to attain. The genetic encodability of these molecular tools make them well suited for studying the spatial and temporal distribution of PTMs. Genetic encodability allows the sensors to be engineered on the DNA level and then synthesized by the cell's own machinery. This ability allows the researcher to take advantage of the breadth of protein domains found in nature as well as those who have been mutated and engineered for a particular behavior. It further allows for the precise targeting of the tools to particular sub-cellular locations. Furthermore, genetic encodability allows for the system to be self-contained. Once the cell of interest contains the DNA construct, no further components are required to be added for the tools to function, and the cell can pass it on to its daughter cells. Furthermore, the cell continually produces the sensor and replenishes it.

For the FLARE biosensors, we demonstrate that the molecular switches commonly used in kinase activity and second messenger biosensors, when sandwiched by two similar FPs excited with a polarized light source, can cause a measurable change in the anisotropy of the light emitted by the FPs. These switches can thus be used to design biosensors that are both single-color, allowing for sensor multiplexing, and ratiometric, allowing for probe concentration effects to be canceled out. Furthermore, this design is compatible with several different color FPs and many different switches, creating a large panel of biosensors from which to choose. We demonstrate that FLARE can be used for imaging up to three activities simultaneously in the same cell, for monitoring signaling activities while they are perturbed by optogenetic tools, and for multiplexed signaling activity monitoring *in vivo* in live cells. Future work will involve increasing the signal-to-noise ratio of these sensors, expanding the panel of activities that the biosensors can monitor, and using these biosensors for biological applications, such as studying cross-talk among signaling pathways. Optimization of signal-to-noise ratio is especially important for the lower performing cyan and red variants. This optimization may be accomplished by changing the FPs used these homo-FRET sensors, or by optimizing the switches themselves. Furthermore, adding different linker sequences or optimizing the molecular switches themselves may also contribute to optimizing the signal-to-noise ratio. Expansion of the tool-kit will also include adapting the FLARE design to study other key signaling activities, as well as by targeting these tools to different subcellular locations.

The FLINC approach to kinase activity biosensing allows the researcher to study localized signaling activities, approaching the level of a signaling microdomain or signalosome, in a dynamic way. By connecting a molecular switch to a change in the fluctuation behavior of an FP, we can uncover sub-diffraction level information about the signaling activity of interest. We demonstrated that they provide a time course of super-resolved activity maps of kinase activity. In this way, we were able to demonstrate that PKA activity is not evenly spread near the plasma membrane, but is considerably heterogeneous and highly localized. More precise characterization of the spatial architecture of PKA signaling at the membrane, as mediated by AKAP proteins as well uncovering the functional implications of this organization are areas of further study. To continue to develop the technology, the FLINC biosensor design should be adapted for other signaling activities. Furthermore, the approach may be generalizable to other FPs for which their fluctuation behavior can be modulated by another protein domain. This motivates the further detailed study of the fluctuation behaviors of FPs and how interactions with other protein interfaces may alter them. Likewise, further work will aim to apply the FLINC approach with imaging of localized signaling activities in other cellular locations than the plasma membrane. Therefore, adapting the technology for lattice light sheet imaging would allow for super-resolved maps of signaling activities in cellular locations not accessible with TIRF microscopy.

Finally, the engineering of a high-affinity chromodomain to serve as a probe for H3K9me3 allows for the study of the spatial organization of histone modifications and how that relates to chromatin organization and gene expression. We have demonstrated a marked improvement in live-cell imaging of H3K9me3 with the mutant compared to the wild type CBX1 chromodomain. One of the key advantages of a live-cell probe for H3K9me3 is the ability to monitor changes the spatial distribution of heterochromatin; therefore, future work will entail performing time course experiments to provide dynamic high resolution maps of H3K9me3, for example during the cell cycle or cellular differentiation. Additionally, a similar approach using other histone PTM binding domains, such as other chromodomains, Tudor domains, or PHD domains, can be used to develop genetically encodable probes for studying other histone modifications.

Together these technologies should help provide insights into the fine tuning of key cellular functions, such as signal processing and gene expression regulation, in space and in time. By uncovering the patterning of dynamics of critical biochemical markers, we reveal a new level of complexity in cellular functioning. A particular protein in a cell does not have just one function, but many, which may vary from precise subcellular location to location, and from one point in time to another.

CURRICULUM VITAE for Ph.D. CANDIDATES

The Johns Hopkins University School of Medicine

BRIAN ROSS

October 1, 2018

Educational History

Ph.D.	2018	Biomedical Engineering Mentor: Jin Zhang, Ph.D.	The Johns Hopkins University
S.B.	2011	Biological Engineering	Massachusetts Institute of Technology

Other Professional Experience

Intern	2015	Biopharmaceutical Development Team	MedImmune, Inc.
Rotation	2012	Lab of Takanari Inoue, Ph.D.	The Johns Hopkins University
Rotation	2011	Lab of Andre Levchenko, Ph.D.	The Johns Hopkins University
Undergraduate Researcher	2010-2011	Lab of K. Dane Wittrup, Ph.D.	Massachusetts Institute of Technology
Undergraduate Researcher	2009	International Genetically Engineered Machines Competition	Massachusetts Institute of Technology
Undergraduate Researcher	2008	Lab of Eric Alm, Ph.D.	Massachusetts Institute of Technology

External Funding

National Institute of Biomedical Imaging and Bioengineering (NIBIB) Training Grant, National Institutes of Health 2013-2015

Academic Honors

Graduate Research Fellowship Honorable Mention 2013 National Science Foundation

Corey Award for Protein Structure Prediction and Design 2012 Rosetta Design Group

Publications

R. Hard, N. Li, W. He, **B. L. Ross**, G. C. H. Mo, Q. Peng, R. Stein, E. Conives, Y. Wang, J. Zhang, W. Wang. (2018) Deciphering and Engineering Chromodomain-Methyllysine Peptide Recognition. *Science Advances.* [under review].

B. L. Ross, B. Tenner, M. L. Markwardt, A. Zviman, G. Shi, J. P. Kerr, N. Snell, J. McFarland, J. Mauban, C. W. Ward, M. A. Rizzo, J. Zhang (2018) Single-Color, Ratiometric Biosensors for Detecting Signaling Activities in Live Cells. *eLife*, 7: e35458.

G. C. H Mo, **B. Ross**, F. Hertel, P. Manna, X. Yang, E. C. Greenwald, C. Booth, A. M. Plummer,
B. Tenner, Z. Chen, Y. Wang, E. J. Kennedy, P. A. Cole, K. G. Fleming, A. Palmer, R. Jimenez, J. Xiao, P. Dedecker, and J. Zhang (2017) Genetically-Encoded Biosensors for Visualizing Live-cell Biochemical Activity at Superresolution. *Nature Methods*, 14: 427-434.

B. Ross, S. Mehta, J. Zhang (2016) Molecular tools for acute spatiotemporal manipulation of signal transduction. *Current Opinion in Chemical Biology.* 34: 135-142.

Posters, Abstracts, Presentations

B. L. Ross (2018) FLAREs: Single-Color, Ratiometric Biosensors of Signaling Activities. University of California, San Diego, Pharmacology Rounds. Speaker. February 2018.

B. L. Ross, B. Tenner, M. L. Markwardt, A. Zviman, G. Shi, J. P. Kerr, J. Mauban, C. W. Ward, M. A. Rizzo, J. Zhang (2016). FLAREs: Single-Color, Ratiometric Biosensors of Signaling Activities. Poster Presentation Post-translational Regulation of Cell Signaling. August 2016.

B. L. Ross (2016) HHMI Janelia Junior Scientist Workshop on Protein Engineering. FLAREs: Single-Color, Ratiometric Biosensors of Signaling Activities. Invited Speaker. HHMI Janelia Junior Scientist Workshop on Protein Engineering. March 2016.

B. L. Ross, B. Tenner, M. L. Markwardt, A. Zviman, G. Shi, J. P. Kerr, J. Mauban, C. W. Ward, M. A. Rizzo, J. Zhang (2016). FLAREs: Single-Color, Ratiometric Biosensors of Signaling Activities. Biophysical Society Meeting. Poster Presentation. February 2016.

B. L. Ross (2015) FLARE: Pushing the Limits of Fluorescent Biosensors. Advanced Study Institute on Global Health Care Challenges, Junior Invited Speaker June 2015.

B. L. Ross. Designing Anisotropy-Based Signaling Activity Biosensors: A ratiometric, single color approach. Johns Hopkins Pharmacology Research in Progress. February 2015.

B. L. Ross 13th Annual Summer School on Bioinnovation, Biocomplexity, and Biodesign, Participant, with Fellowship. June 2014.

B. L. Ross, J. Zhang**,** Superresolution Plasmalemmal Lipid Mapping. Biophysical Society Meeting. Poster Presentation. February 2014.

M. Manzari, E. Rosalia, **B. L. Ross**, F. Sun, J. Spangler, K. D. Wittrup (2011). Construction and characterization of multi-specific anti-EGFR antibodies for targeted cancer therapy. Poster Presentation. MIT 150: Undergraduate Research Opportunities Program (UROP) Poster Session. April 2011.

J. Spangler, B. Epstein, **B. L. Ross,** Mariah Murray, K. Dane Wittrup (2010). Characterization and Informed Design of downregulating anti-epidermal growth factor receptor antibodies. Protein Society Annual Meeting. July 2010.

B. L. Ross, C. Li, A. Doolittle, D. McDonald (2009). Light Switchable Protein Localization System. International Genetically Engineered Machines (iGEM) Jamboree. Speaker. November 2009.

Patent

Epstein B, Ross B, & Spangler J. *Antibody-based constructs directed against tyrosine kinase receptors* Filed: 2011, Published: 2013. **US 20130216543 A1.**

Service and Leadership

2016-2018	Organizer of San Diego Jewish LGBT Meetup, a social group connecting LGBT members of the Jewish community in San Diego
2017	Guest Lecturer for Seminars in Biomedical Research, University of California San Diego, San Diego, CA.
2015	Teaching Assistant for Models and Simulations, Johns Hopkins University, Baltimore, MD.
2014	Teaching Assistant for Build-A-Genome, Johns Hopkins University, Baltimore, MD (January-May 2014).
2014-2015	Programming Committee Member of JQ Baltimore, an LGBT Jewish organization in Baltimore City

2013-2015	Co-chair of Beth Am Young Adults Twenties and Thirties (BAYITT), a group that organized social, religious, and social action programming for young Jewish professionals in BAltimore
2011-2015	Tutor and Mentor for Incentive Mentoring Program/Thread, a group that offers tutoring and mentorship for disadvantaged high school students in Baltimore City

Biography

Brian L. Ross was born in 1989 in Los Angeles, California, United States of America.

He performed his undergraduate work at the Massachusetts Institute of Technology, where he received a Bachelor of Science degree in Biological Engineering. During his time as an undergraduate, he was on the International Genetically Engineered Machines Competition, where he worked on a project to engineer a reversibly switchable light-induced dimerization system. He then worked in the laboratory of Dr. K. Dane Wittrup, where he developed bispecific antibodies for targeted cancer therapy.

Brian Ross joined the Biomedical Engineering Department at the Johns Hopkins University in 2011 for his PhD work. He performed laboratory rotations. In Dr. Andre Levchenko, he developed a computation model for oscillatory behavior in VEGFR signaling in endothelial cells, while in Dr. Takanari Inoue's laboratory he used studied the interactions between poly-basic sequences and the plasma membrane. In 2012, he joined the Dr. Jin Zhang's laboratory, where he performed is dissertation work. In the summer and fall of 2015, he did an internship at MedImmune, Inc, in which he worked in the protein biophysics development team to work on vaccine development.